

**SYNTHESIS OF PORPHYRINIC METAL ORGANIC FRAMEWORKS WITH
HIGH ROBUSTNESS AND CATALYTIC ACTIVITY**

A Dissertation

by

KECHENG WANG

Submitted to the Office of Graduate and Professional Studies of
Texas A&M University
in partial fulfillment of the requirements for the degree of

DOCTOR OF PHILOSOPHY

Chair of Committee,	Hong-Cai Zhou
Committee Members,	Kim Dunbar
	Paul Lindahl
	Hae-Kwon Jeong
Head of Department,	Simon North

August 2017

Major Subject: Chemistry

Copyright 2017 Kecheng Wang

ABSTRACT

MOFs are ideal platforms to immobilize porphyrins and their derivatives. MOF's high surface areas and rigid structures not only make porphyrin moieties approachable substrates but also prevent the dimerization of their active centers. These advantages effectively enhance the reactivity and optical performance of porphyrins. Extensive study has been done to synthesize porphyrinic MOFs, however, many of the previously reported porphyrinic MOFs suffer from weak chemical stabilities, which severely hinders their wide utilization. My study is focused on the design and syntheses of porphyrinic MOFs with high robustness in various chemical environments. Three porphyrinic MOFs with excellent chemical stability, namely PCN-600, PCN-601 and PCN-602, were obtained, and their performances as catalysts in different reactions were explored.

PCN-600, a Fe-based mesoporous porphyrinic MOF was successfully synthesized through rational topological design and KTDA method. It exhibits high chemical stability in aqueous solutions with pH values ranging from 2 to 11. The catalytic activity of PCN-600(Fe) (with Fe^{3+} at the porphyrin center) was confirmed by its excellent performance in the co-oxidation of phenol and 4-aminoantipyrine (4-AAP) by H_2O_2 .

Most of the reported stable porphyrinic MOFs, including PCN-22Xs (X = 2, 3, 4, 5) and PCN-600, are constructed by high-valent metal ions and carboxylate-based porphyrinic ligands. Though these materials have very high robustness in acidic

solutions, they are relatively vulnerable in aqueous solutions containing some coordinating anions, such as OH^- , F^- , CO_3^{2-} and PO_4^{3-} . To address these problems, two iso-structural porphyrinic MOFs constructed by pyrazolate-terminated ligands were synthesized, namely PCN-601 and PCN-602. These materials exhibit extraordinary stability in the solutions of NaOH , KF , Na_2CO_3 and K_3PO_4 . Their chemical stabilities were rationalized from both thermodynamic and kinetic perspectives. The catalytic performance of PCN-601(Mn) and PCN-602(Mn) (with Mn^{3+} at the coordination centers of the porphyrinic ligands) in C-H halogenation reactions was explored. Compared with PCN-601(Mn), PCN-602(Mn) has a higher porosity and displays a better activity as a recyclable heterogeneous catalyst.

DEDICATION

To my family and my friends

For their love and support

ACKNOWLEDGEMENTS

I would first like to thank my advisor, Dr. Hong-Cai Zhou for providing me with numerous excellent opportunities to train myself over these years. I would like to express my appreciation to my committee members, Dr. Kim Dunbar, Dr. Paul Lindahl, and Dr. Hae-Kwon Jeong for strengthening my science background. Our department members, especially Ms. Sandy Horton, Ms. Lizzie West and Ms. Carrie Frederiksen, have made my time at Texas A&M University a wonderful experience.

My fellow labmates have been incredible to work with. I would like to thank my mentors Julian Sculley and Dawei Feng, who imparted their knowledge of metal organic frameworks to me without reservation. Dr. Tian-Fu Liu, Hao Li, Zhangwen Wei, Dr. Dahuan Liu, and Jihye Park provided a lot of useful suggestions. Stephen Fordham and Mathieu Bosch helped me to polish my writing and oral skills. I am grateful to Dr. Qiang Zhang and Dr. Daqiang Yuan for insightful discussions.

CONTRIBUTORS AND FUNDING SOURCES

Contributors

This work was supervised by a dissertation committee consisting of Professor Hong-Cai Zhou [advisor], Professor Dr. Kim Dunbar, Professor Dr. Paul Lindahl of the Department of Chemistry [Home Department] and Professor Dr. Hae-Kwon Jeong of the Department of Materials Science and Engineering [Outside Department].

The catalytic reaction in Chapter II was designed and conducted by Dr. Tian Liu of the Department of Chemistry and the structural refinements of PCN-600(Fe) and PCN-600(Co) were done by Dr. Jie Su. The context was published in *J. Am. Chem. Soc.*, 136, 13983, 2014. The H₄TPP ligand in Chapter III was synthesized by Xiuliang Lv. The structural refinement of PCN-601 was conducted by Dr. Junliang Sun. The context was published in *J. Am. Chem. Soc.*, 138, 914, 2016. The syntheses of H₄TPP, Mn(H₄TPPP)Cl and Mn(H₄TPP)Cl in Chapter IV were conducted by Xiuliang Lv. The structural refinement of PCN-602(Ni) was done by Dr. Jie Su. The context was published in *J. Am. Chem. Soc.*, 139, 211, 2017.

Funding Sources

This work was supported as part of the Center for Clean-Energy-related Gas Separation, an Energy Frontier Research Center (EFRC) funded by the U.S. Department of Energy (DOE), Office of Science, Office of Basic Energy Sciences under Award Number DE-SC0001015.

User Facility operated for the US Department of Energy (DOE) Office of Science by Argonne National Laboratory, was supported by the U.S. DOE under Contract No. DE-AC02-06CH11357.

NOMENCLATURE

1D	One dimensional
3D	Three dimensional
BET	Brunauer-Emmett-Teller
CAN	Ceric ammonium nitrate
DOE	United States Department of Energy
DFT	Density Functional Theory
DMF	<i>N,N</i> -Dimethyl Formamide
DMSO	Dimethyl Sulfoxide
EA	Elemental analysis
ESI	Electrospray ionization
Et ₃ N	Triethylamine
FT-IR	Fourier transform infrared spectroscopy
GC	Gas chromatography
HSAB	Hard-soft-acid-base
ICP	Inductively coupled plasma
KTDA	Kinetically tuned dimensional augmentation
MOF	Metal organic framework
MeOH	Methanol
MS	Mass spectrum
NMR	Nuclear Magnetic Resonance

PCN	Porous Coordination Network
PMBCl	4-Methoxybenzylchloride
PTC	Phase transfer catalyst
PXRD	Powder X-Ray Diffraction
Pz	Pyrazolate
SBU	Secondary Building Unit
STP	Standard temperature and pressure
TBACl	Tetrabutylammonium chloride
TLC	Thin-layer chromatography

TABLE OF CONTENTS

ABSTRACT	ii
DEDICATION	iv
ACKNOWLEDGEMENTS	v
CONTRIBUTORS AND FUNDING SOURCES.....	vi
NOMENCLATURE.....	viii
TABLE OF CONTENTS	x
LIST OF FIGURES.....	xii
LIST OF TABLES	xvii
LIST OF SCHEMES.....	xviii
CHAPTER I INTRODUCTION	1
CHAPTER II A SERIES OF HIGHLY STABLE MESOPOROUS METALLOPORPHYRIN IRON-MOFS	4
2.1 Introduction	4
2.2 Experimental Section	6
2.2.1 Synthesis of $[\text{Fe}_3\text{O}(\text{OOCCH}_3)_6\text{OH}] \cdot 2\text{H}_2\text{O}$	6
2.2.2 Synthesis of PCN-600.....	7
2.2.3 Structural refinement of PCN-600.....	8
2.2.4 The activation and adsorption measurements of PCN-600	11
2.2.5 BET surface area and pore size distribution analysis of PCN-600	12
2.2.6 Thermal Stability of PCN-600 Samples	13
2.2.7 Catalytic activity of PCN-600(Fe).....	16
2.3 Results and Discussion.....	18
2.3.1 Topological design and Structural Description of PCN-600.....	18
2.3.2 N_2 Uptakes of PCN-600.....	19
2.3.3 Chemical Stability Analysis of PCN-600	20
2.3.4 Catalytic Activity Analysis of PCN-600(Fe).....	21
2.4 Conclusions	23
CHAPTER III A PYRAZOLATE-BASED PORPHYRINIC MOF WITH EXTRAORDINARY BASE-RESISTANCE.....	24
3.1 Introduction	24

3.2 Experimental Section	26
3.2.1 Synthesis of H ₄ TPP.....	26
3.2.2 Synthesis of PCN-601.....	27
3.2.3 Structural Refinement of PCN-601.....	27
3.2.4 Gas adsorption of PCN-601.....	31
3.2.5 Chemical Stability Tests of PCN-601.....	33
3.1 Results and Discussion.....	34
3.3.1 Topological Design and Structural Analysis of PCN-601.....	34
3.3.2 Chemical Stability Analysis of PCN-601.....	38
3.4 Conclusions	43
CHAPTER IV A BASE-RESISTANT METALLOPORPHYRIN MOF FOR C–H BOND HALOGENATION.....	44
4.1 Introduction	44
4.2 Experimental Section	48
4.2.1 Synthesis of H ₄ TPPP	48
4.2.2 Synthesis Mn(H ₄ TPPP)Cl.....	52
4.2.3 Synthesis of Mn(H ₄ TPP)Cl.....	54
4.2.4 Synthesis of MOFs.....	56
4.2.5 Thermal Stability of PCN-602(M) (M = Ni or Mn)	60
4.2.6 Powder X-Ray Diffraction of PCN-602(M) (M = Ni or Mn).....	62
4.2.7 N ₂ Adsorption/Desorption Isotherms of PCN-602(M) (M = Ni or Mn)	62
4.2.8 Rietveld Refinement and Crystallographic Data of PCN- 602(Ni).....	66
4.2.9 Chemical Stability Tests of PCN-602.....	68
4.2.10 Catalytic Activity Tests of PCN-602(Mn).....	69
4.3 Results and Discussion.....	69
4.3.1 Chemical Stability of PCN-602	69
4.3.2 Catalytic Activity of PCN-602(Mn)	74
4.5 Conclusions	87
CHAPTER V SUMMARY	88
REFERENCES.....	90

LIST OF FIGURES

	Page
Figure 1. (a) stp-a network, (b) D_{3h} symmetric six-connected node and (c) D_{4h} four-connected node, (d) and (e) Corresponding nodes commonly seen in MOFs and PCN-600.....	6
Figure 2. Rietveld refinement of PXRD for PCN-600(Fe).....	9
Figure 3. Rietveld refinement of PXRD for PCN-600(Co).....	10
Figure 4. The N_2 sorption isotherms of PCN-600(Fe) samples at 77 K after being treated with different aqueous solutions.....	11
Figure 5. The plot of the linear region on the N_2 isotherm of PCN-600(Fe) for the BET equation.....	12
Figure 6. DFT pore size distribution for PCN-600(Fe).	13
Figure 7. Thermogravimetric analysis of the activated PCN-600(Mn).....	14
Figure 8. Thermogravimetric analysis of the activated PCN-600(Fe).....	14
Figure 9. Thermogravimetric analysis of the activated PCN-600(Co).....	15
Figure 10. Thermogravimetric analysis of the activated PCN-600(Ni).....	15
Figure 11. Thermogravimetric analysis of the activated PCN-600(Cu).....	16
Figure 12. The time course of co-oxidation of phenol and 4-aminoantipyrine as a function of H_2O_2 concentration for PCN-600(Fe).....	17
Figure 13. The initial rate of co-oxidation reaction with PCN-600(Fe) as the catalyst.....	18
Figure 14. (a) Crystals of PCN-600(Fe) under an optical microscope. As-synthesized (left), after treatment of pH = 2 solution for 24 h (middle) and after treatment of pH = 11 solution for 24 h (right). (b) Powder X-ray diffraction pattern of PCN-600(Fe) and the samples treated with aqueous solution with pH = 2 and 11. (c) N_2 adsorption isotherms for PCN-600(Fe) at 77 K, showing the framework stability of PCN-600(Fe) upon treatments with the aqueous solutions with pH = 2 and 11.....	21

Figure 15. Structural analysis of PCN-601. (a) ftw-a topology; (b) O_h symmetric 12-connected node; (c) D_{4h} symmetric 4-connected node; (d) PCN-601; (e) $[Ni_8]$ cluster; (f) TPP^{4-} ligand. The Ni atoms in the porphyrin center are omitted for clarity.	25
Figure 16. Electron density map of PCN-601.....	28
Figure 17. Rietveld refinement of PXRD data for PCN-601.....	31
Figure 18. The N_2 adsorption/desorption isotherm of PCN-601 at 77 K.....	32
Figure 19. The plot of the linear region on the N_2 isotherm of PCN-601 for the BET equation.....	32
Figure 20. The DFT pore size distribution for PCN-601.....	33
Figure 21. Top-down topology analysis: binodal edge-transitive topologies with planar 4-connected nodes (top line), the nodes assigned to SBUs in corresponding nets (middle line), and reported Pz-based SBUs with the same symmetries and connectivities to corresponding nodes (bottom line).....	36
Figure 22. Topology and geometry analysis of PCN-221 and PCN-601: (a) PCN-221; (b) $[Zr_8O_6(CO_2)_{12}]^{8+}$ cluster; (c) $TCPP^{4-}$; (d) ftw-a topology; (e) O_h symmetric 12-connected node; (f) D_{4h} symmetric 4-connected node; (g) PCN-601 (the Ni atoms in the porphyrin center are omitted for clarity); (h) $[Ni_8]$ cluster; (i) TPP^{4-}	37
Figure 23. (a) PXRD patterns for simulated, pristine PCN-601 and PCN-601 samples treated under different conditions; (b) N_2 adsorption/desorption isotherms at 77 K of pristine PCN-601 and treated PCN-601 samples.	38
Figure 24. (a) DMF solutions with immersed PCN-601 samples being treated under 0.1 mM HCl solution at room temperature for 24 h (left) and saturated NaOH at 100 °C for 24 h (middle), respectively. In the right vial it is the standard solution of H_4TPP in DMF (1 mg/20 mL); (b) electronic absorption spectra of different DMF solutions from the vials in Figure 24(a).	39
Figure 25. d orbital splitting of Ni^{2+} in octahedral coordination sphere. $\Delta_{0,O}$ is the crystal field splitting parameter in OH^- (or H_2O) coordination sphere; $\Delta_{0,N}$ is the crystal field splitting parameter in pyrazolate coordination sphere.....	40

Figure 26. Reticular design and construction of PCN-602: (a) <i>ftw-a</i> topological net; (b) 12-connected node with O_h symmetry; (c) 4-connected node with D_{4h} symmetry; (d) TPP^{4-} ligand; (e and h) $[Ni_8]$ cluster; (f) structure of PCN-601 (Ni atoms in the porphyrin center are omitted for clarity); (g) proposed structure of PCN-602; and (i) $TPPP^{4-}$ ligand.	47
Figure 27. FT-IR spectra of H_4TPPP and PCN-602(Ni).	57
Figure 28. FT-IR spectra of $Mn(H_4TPPP)Cl$ and PCN-602(Mn).	58
Figure 29. PXRD profiles of simulated and experimental PCN-222(Fe).	58
Figure 30. PXRD profiles of simulated and experimental PCN-224(Co).	59
Figure 31. PXRD profiles of simulated and experimental PCN-600(Mn).	59
Figure 32. PXRD profiles of simulated and experimental PCN-601(Mn).	60
Figure 33. The N_2 adsorption/desorption isotherms of PCN-601(Mn) at 77 K.	60
Figure 34. The thermogravimetric analysis of as-synthesized PCN-602(Ni).	61
Figure 35. The thermogravimetric analysis of as-synthesized PCN-602(Mn).	61
Figure 36. PXRD profiles of simulated and pristine of PCN-602(Ni).	62
Figure 37. PXRD profiles of simulated and pristine of PCN-602(Mn).	62
Figure 38. N_2 adsorption/desorption isotherm of PCN-602(Ni) at 77 K.	63
Figure 39. The plot of $P/P_0/(n(1-P/P_0))$ vs. P/P_0 to determine the BET surface area.	64
Figure 40. DFT pore size distribution of PCN-602(Ni) evaluated by using N_2 adsorption data measured at 77 K.	64
Figure 41. N_2 adsorption/desorption isotherm of PCN-602(Mn) at 77 K.	65
Figure 42. The plot of $P/P_0/(n(1-P/P_0))$ vs. P/P_0 to determine the BET surface area.	65
Figure 43. DFT pore size distribution of PCN-602(Mn) evaluated by using N_2 adsorption data measured at 77 K.	66
Figure 44. Rietveld refinement of powder X-ray diffraction data for PCN-602(Ni) (the curves from top to bottom are simulated (red), observed (blue),	

and difference profiles (gray), respectively; the bars below curves indicate peak positions.	67
Figure 45. PXRD patterns simulated from the PCN-602 structural model, of pristine PCN-602(Ni) sample, and of those treated in different aqueous solutions.	71
Figure 46. N ₂ adsorption/desorption isotherms of pristine PCN-602(Ni) sample and of those treated in different aqueous solutions (inset: photographs of PCN-602(Ni), -224(Co), -222(Fe), and -600(Mn) soaked in different solutions for 24 h: deionized water, 1 M KF, 1 M Na ₂ CO ₃ , and 1 M K ₃ PO ₄ aqueous solutions, from left to right).	71
Figure 47. PXRD profiles of simulated, pristine PCN-602(Mn), and PCN-602(Mn) treated under different conditions.	72
Figure 48. N ₂ adsorption/desorption isotherms for simulated, pristine PCN-602(Mn), and PCN-602(Mn) samples treated under different conditions at 77 K.....	72
Figure 49. Electronic absorption spectrum of different solutions from the vials in inset (From left to right, Mn(H ₄ TPPP)Cl in DMF solution (0.1 mg / 4 mL), PCN-602(Mn) treated by pH = 4, pH =14, 1 M K ₃ PO ₄ , 1 M Na ₂ CO ₃ and 1 M KF aqueous solution (these samples were washed with deionized water and soaked in DMF)).	73
Figure 50. GC of the chlorination of cyclohexane catalyzed by PCN-602(Mn); inset shows the MS of cyclohexane and chlorocyclohexane.	76
Figure 51. GC of the chlorination of cyclohexane catalyzed by Mn(H ₄ TPPP)Cl.	77
Figure 52. GC of the chlorination of cyclohexane catalyzed by Mn(TPP)Cl.....	77
Figure 53. GC of the chlorination of cyclohexane catalyzed by Mn(TPP)Cl using CH ₂ Cl ₂ as the solvent.	80
Figure 54. GC of the chlorination of cyclohexane catalyzed by PCN-602(Mn) using CH ₂ Cl ₂ as the solvent.....	80
Figure 55. GC of the chlorination of cyclohexane catalyzed by Mn(H ₄ TPPP)Cl using acetone as the solvent.	81
Figure 56. GC of the chlorination of cyclohexane catalyzed by PCN-602(Mn) using acetone as the solvent.	81

Figure 57. GC of the chlorination of cyclohexane catalyzed by Mn(TPP)Cl using methanol as the solvent.	82
Figure 58. GC of the chlorination of cyclohexane catalyzed by PCN-602(Mn) using methanol as the solvent.....	82
Figure 59. GC of the chlorination of cyclohexane catalyzed by Mn(H ₄ TPPP)Cl using ethanol as the solvent.....	83
Figure 60. GC of the chlorination of cyclohexane catalyzed by PCN-602(Mn) using ethanol as the solvent.....	83
Figure 61. (a) Catalytic efficiencies of PCN-602(Mn) and Mn(TPP)Cl in the cyclohexane chlorination in the presence of PTC and CH ₂ Cl ₂ (black) and under the optimal conditions in this work without PTC (red); (b) catalytic efficiencies of PCN-602(Mn) in three consecutive cyclic runs; and (c) PXRD patterns and (d) N ₂ adsorption/desorption isotherms (at 77 K) of pristine PCN-602(Mn) and that after 3 catalytic cycles, respectively.....	86

LIST OF TABLES

	Page
Table 1. Crystallographic data, experimental conditions for powder X-ray data collection and results of the Rietveld refinement of PCN-600(Fe).....	9
Table 2. Crystallographic data, experimental conditions for powder X-ray data collection and results of the Rietveld refinement of PCN-600(Co).	10
Table 3. BET surface and total pore volume of PCN-600(M).	13
Table 4. Catalytic activity of PCN-600(Fe).	23
Table 5. The peaks for indexing of PCN-601.....	29
Table 6. Crystallographic data, experimental conditions for PXRD data collection, and the Rietveld refinement result of PCN-601.	30
Table 7. Crystallographic data and the Rietveld refinement result of PCN-602(Ni).	67
Table 8. The state of different MOFs after treated under different conditions.	73
Table 9. Catalytic performance of PCN-602(Mn), Mn(H ₄ TPPP)Cl, and Mn(TPP)Cl in the C–H bond chlorination under the reported conditions.	76
Table 10. Catalytic performance of PCN-602(Mn), Mn(H ₄ TPPP)Cl, and Mn(TPP)Cl in different solvents for the C–H bond chlorination of cyclohexane.	78
Table 11. The catalytic performance of PCN-602(Mn) and other selected catalysts in the C–H bond chlorination/bromination of cyclohexane/cyclopentane.....	84

LIST OF SCHEMES

	Page
Scheme 1. Reaction catalyzed by PCN-600(Fe).....	21
Scheme 2. Synthesis procedure for H ₄ TPP.....	26
Scheme 3. (a) Thermodynamic stability of PCN-601 in acid and base conditions; (b) Kinetic stability of MOFs with different length of ligands: d _s and d _l are the displacements of terminals of ligands in transition states, θ _s and θ _l are the bending angles of ligands in transition states.....	42
Scheme 4. Synthetic procedure for H ₄ TPPP. Reagents and conditions: (a) Et ₃ N, CH ₂ Cl ₂ , 50 °C; (b) Pd(OAc) ₂ , K ₃ PO ₄ , di(1-adamantyl)-n- butylphosphine, toluene, reflux; and (c) CH ₂ Cl ₂ , CH ₃ OH, HCl, 45 °C.	48
Scheme 5. Synthesis of Mn(H ₄ TPPP)Cl. Reagents and conditions: (a) MnCl ₂ ·4H ₂ O, DMF, reflux and (b) CH ₂ Cl ₂ , CH ₃ OH, HCl, 45 °C.....	52
Scheme 6. Synthesis of Mn(H ₄ TPP)Cl. Reagents and conditions: (a) PMBCl, DMF, K ₂ CO ₃ , reflux; (b) MnCl ₂ ·4H ₂ O, DMF, reflux; (c) CAN, CH ₃ CN, 60 °C.	54
Scheme 7. Chlorination of cyclohexane under the reported method.	75
Scheme 8. Chlorination of cyclohexane in different solvents.	78
Scheme 9. C–H bond halogenation catalyzed by PCN-602(Mn).	85

CHAPTER I

INTRODUCTION

Metal-organic frameworks (MOFs) emerge as a group of porous materials, which are constructed by inorganic nodes and organic linkers.¹⁻³ Because of their large surface areas, high porosities, and structural tunabilities, MOFs have been extensively investigated for their application potentials in gas storage and separation, chemical sensing, and catalysis.⁴⁻²⁰

As a prerequisite for their good performances and easy regenerabilities, MOFs should be robust enough to survive in the chemical conditions involved in their application scenarios, such as being exposed to water (moisture), being immersed in chemicals, or under *in vivo* environments. Typically, the stability of MOFs can be evaluated from three different perspectives: chemical stability, thermal stability, and mechanical stability.²¹ They represent the ability of MOFs to maintain their long-range ordered structures when being treated by chemicals, high temperature, and mechanical force, respectively.²¹

Due to the absolute abundance of water on the earth and its wide involvement in chemical reactions, a great attention has been focused on the chemical stability of MOFs in aqueous solutions and water vapor. At a basic level, MOF structures can be divided into two parts: building nodes (inorganic clusters and organic linkers) and linkages (coordination bonds between building nodes). In most cases, these coordination bonds are the weakest parts that will be attacked by water or other coordinating species in the

solutions during the decomposition of MOFs. Consequently, the strength of the linkages is the determining factor to the stability of MOFs.^{22, 23}

Apart from stability, another challenge is how to endow MOFs with certain functions for specific applications. One effective method is to construct MOFs with organic linkers containing particular functional moieties.¹⁶ Among these organic linkers, porphyrinic ligands have been extensively explored, because porphyrin and its derivatives are vital molecules in many chemical and biological processes. These porphyrinic species can be utilized as anti-cancer drugs, catalysts, antenna pigment molecules, pH sensors, nonlinear optical materials and DNA-binding/-cleavage agents.²⁴⁻³³ When porphyrinic species are immobilized into MOFs, the high surface areas and high porosities of MOFs would be extremely beneficial for the exposure of porphyrin centers to substrates. Moreover, each porphyrin center can be fixed at a certain position owing to the rigid structures of MOFs, which would efficiently prevent the dimerization of active centers. Both these advantages can significantly enhance the reactivities and optical performances of porphyrins.³⁴⁻³⁶

Based on the above analysis, stable porphyrinic MOFs are highly desired for applications that require porphyrin species and are conducted in aqueous solutions. Though vast research efforts have been devoted to developing porphyrinic MOFs,³⁷ only a few successful cases have been reported, such as PCN-22Xs (PCN = porous coordination networks; X= 2, 3, 4, 5). Despite the fact that these MOFs display excellent stability at acidic conditions, they are rather vulnerable in the solutions with hydroxide or other coordinating anions, like OH⁻, F⁻, CO₃²⁻, PO₄³⁻. However, the aforementioned

anions are widely involved in many application scenarios of porphyrinic species as essential reactants or components of buffer solutions. Therefore, it is extraordinarily crucial to develop porphyrinic MOF materials with excellent resistance to coordinating anions.

CHAPTER II

A SERIES OF HIGHLY STABLE MESOPOROUS METALLOPORPHYRIN

IRON-MOFS*

2.1 Introduction

In most of the reported porphyrinic MOFs, the coordination moieties of ligands are carboxylate groups, which are considered as hard Lewis bases.³⁸⁻⁴⁹ When relatively soft Lewis acidic species are used to construct the inorganic nodes in porphyrinic MOFs, such as Zn^{2+} , Cu^{2+} and Cd^{2+} , the coordinating bonds between carboxylate groups and these metal ions are weak. It makes the frameworks less resistant to the attack of reactive chemical species, which severely restricts the applications of porphyrinic MOFs under harsh conditions. To address this problem, clusters formed with high valent metal ions, which are hard Lewis acids, are selected as the inorganic nodes. The strong interactions between high valent metal ions and carboxylate groups significantly increase stability of the frameworks.^{34, 35, 50-58} Guided by this strategy, PCN-22Xs ($X = 2, 3, 4, 5$), a series of zirconium MOFs, are representative examples of stable porphyrinic MOFs obtained through the strategy above. However, because of the similarity of crystal growing conditions of PCN-22Xs and the diverse connectivities of Zr_6 clusters, the multiple phases are always obtained in the syntheses of PCN-22Xs, leading to the tremendous difficulty in phase purification. This has severely hampered the wide applications and

*Reproduced with permission from Wang, K. †; Feng, D. †; Liu, T.-F.; Su, J.; Yuan, S.; Chen, Y.-P.; Bosch, M.; Zou, X.; Zhou, H.-C., A Series of Highly Stable Mesoporous Metalloporphyrin Fe-MOFS. *Journal of the American Chemical Society* **2014**, *136* (40), 13983-13986. 2014 American Chemical Society.

bulk productions of these Zr-based porphyrinic MOFs.^{59, 60} Therefore, the easy synthesis of chemically stable porphyrinic MOFs with pure phase has been a prominent goal.

Fe(III) is an ideal alternative metal ion to construct the inorganic nodes of MOFs due to its nontoxicity, elemental abundance on the earth. Moreover, because of its high hardness as a Lewis acid, Fe(III) can form stronger coordinating bonds with carboxylates, which could enhance the robustness of the frameworks. Similar to other stable MOFs, the structural determination of Fe-MOFs has been a long-standing challenge due to the difficulty of obtaining large single crystals and the formation of the unpredicted inorganic building blocks during the syntheses of Fe-MOFs.⁶⁰ However, the development of KTDA method provides us with a novel strategy to obtain the large crystals of Fe-MOFs with the desired structures.⁶¹

The **stp-a** network is an edge-transitive topology which contains six-connected prism nodes with D_{3h} symmetry and four-connected square planar nodes with D_{4h} symmetry (Figure 1a, 1b, 1c). The connectivities and symmetries of the two nodes in stp-a are exactly the same to those of $\text{Fe}_3\text{O}(\text{OOC})_6$ cluster and the most commonly used four-connected porphyrinic linker, tetrakis (4-carboxyphenyl) porphyrin (H_4TCPP). Therefore it is topologically allowed for us to construct Fe-MOFs with stp-a topology by $\text{Fe}_3\text{O}(\text{OOC})_6$ cluster and TCPP^{4-} (Figure 1d, 1e, 1f). Herein, guided by the topological analysis and KTDA method, we synthesized a series of highly stable mesoporous porphyrinic Fe-MOFs, namely PCN-600(M) (M = Mn, Fe, Co, Ni, Cu). PCN-600 exhibits 1D channels as large as 3.1 nm and the highest experimental pore volume of $1.80 \text{ cm}^3 \text{ g}^{-1}$ among all the reported porphyrinic MOFs. Remarkably, it also shows very

high stability in aqueous solutions with pH values ranging from 2 ~ 11. Among them, PCN-600(Fe) has been demonstrated as an effective catalyst in co-oxidation reaction.

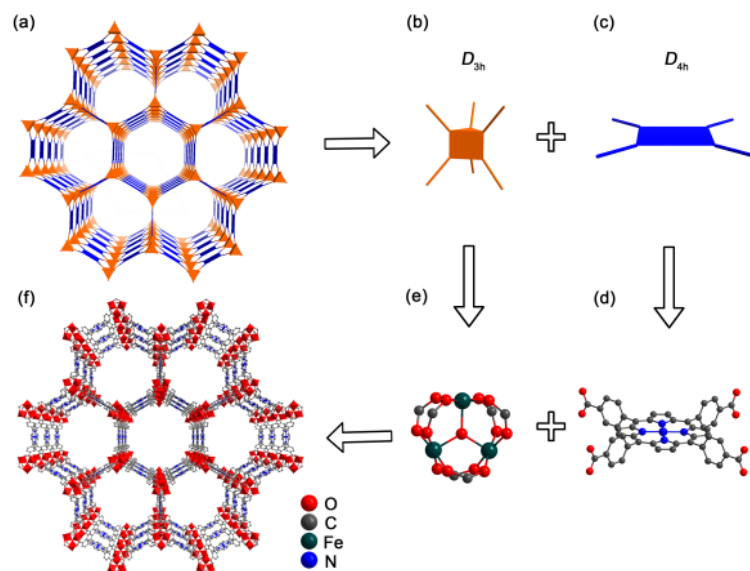


Figure 1. (a) *stp-a* network, (b) D_{3h} symmetric six-connected node and (c) D_{4h} four-connected node, (d) and (e) Corresponding nodes commonly seen in MOFs and PCN-600.

2.2 Experimental Section

2.2.1 Synthesis of $[\text{Fe}_3\text{O}(\text{OOCCH}_3)_6\text{OH}] \cdot 2\text{H}_2\text{O}$

$\text{Fe}(\text{NO}_3)_3 \cdot 9\text{H}_2\text{O}$ (8 g) and $\text{Na}(\text{OOCCH}_3) \cdot 3\text{H}_2\text{O}$ (11 g) were dissolved in 9 ml deionized water. The solution was stirred overnight at room temperature. The red precipitation was filtered and washed with cold deionized water once. The obtained product was dry in an oven at 100 °C. The crystal of product was got from recrystallization in DMF at 150 °C.

2.2.2 Synthesis of PCN-600

PCN-600(Mn): [5,10,15,20-Tetrakis(4-methoxycarbonylphenyl)porphyrinato]-Mn(III) Chloride (Mn(H₄TCPP)Cl) was synthesized according to the procedure in previous reports.³⁴ [Fe₃O(OOCCH₃)₆OH]·2H₂O (80 mg), Mn(H₄TCPP)Cl (80 mg) and Trifluoroacetic acid (2.4 mL) were added into DMF (16 ml) in a 20 mL Pyrex vial. The mixture was heated to 150 °C for 12 h. After cooling down to room temperature, dark needle-shaped crystals were obtained.

PCN-600(Fe): [5,10,15,20-Tetrakis(4-carboxyphenyl)porphyrinato]-Fe(III) Chloride (Fe(H₄TCPP)Cl) was synthesized according to the procedure in previous reports.³⁴ [Fe₃O(OOCCH₃)₆OH]·2H₂O (80 mg), Fe(H₄TCPP)Cl (80 mg) and Trifluoroacetic acid (2.4 mL) were added into DMF (16 ml) in a 20 mL Pyrex vial. The mixture was heated to 150 °C for 12 h. After cooling down to room temperature, dark needle-shaped crystals were obtained.

PCN-600(Co): [5,10,15,20-Tetrakis(4-methoxycarbonylphenyl)porphyrinato]-Co(II) (Co(H₄TCPP)) was synthesized according to the procedure in previous reports.³⁴ [Fe₃O(OOCCH₃)₆OH]·2H₂O (80 mg), Co(H₄TCPP) (80 mg) and Trifluoroacetic acid (2.4 mL) were added into DMF (16 ml) in a 20 mL Pyrex vial. The mixture was heated to 150 °C for 12 h. After cooling down to room temperature, dark needle-shaped crystals were obtained.

PCN-600(Ni): [5,10,15,20-Tetrakis(4-methoxycarbonylphenyl)porphyrinato]-Ni(II) (Ni(H₄TCPP)) was synthesized according to the procedure in previous reports.³⁴ [Fe₃O(OOCCH₃)₆OH]·2H₂O (80 mg), Ni(H₄TCPP) (80 mg) and Trifluoroacetic acid

(2.4 mL) were added into DMF (16 ml) in a 20 mL Pyrex vial. The mixture was heated to 150 °C for 12 h. After cooling down to room temperature, dark needle-shaped crystals were obtained.

PCN-600(Cu): [5,10,15,20-Tetrakis(4-methoxycarbonylphenyl)porphyrinato]-Cu(II) (Cu(H₄TCPP)) was synthesized according to the procedure in previous reports.³⁴ [Fe₃O(OOCCH₃)₆OH]·2H₂O (80 mg), Cu(H₄TCPP) (80 mg) and Trifluoroacetic acid (2.4 mL) were added into DMF (16 ml) in a 20 mL Pyrex vial. The mixture was heated to 150 °C for 12 h. After cooling down to room temperature, dark needle-shaped crystals were obtained.

2.2.3 Structural refinement of PCN-600*

The Rietveld refinement of PCN-600(Fe, Co) against PXRD data was performed using Topas Academic V4.1. The background was fitted with a 10th (for Fe) or 12th (for Co) order Chebychev polynomial. The refinement was conducted using a Pearson VII peak profile function, followed by refinement of unit cells and zero-shift. The rigid bodies were applied on the porphyrin ligand (Figure 2-3 and Table 1-2).

* The structural refinement of PCN-602 was conducted by Dr. Jie Su.

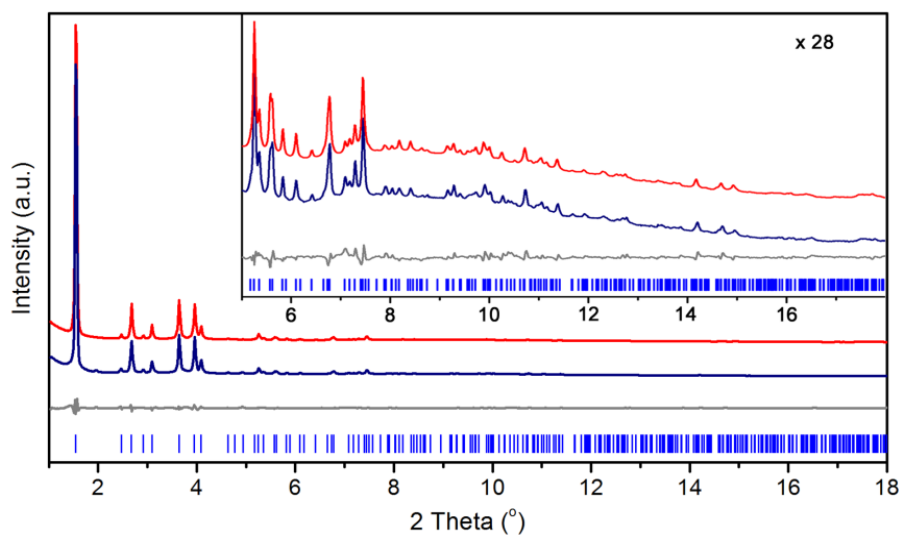


Figure 2. Rietveld refinement of PXRD for PCN-600(Fe). The curves from top to bottom are simulated (red), observed (blue), and difference profiles (grey), respectively; the bars below curves indicate peak positions.

Table 1. Crystallographic data, experimental conditions for powder X-ray data collection and results of the Rietveld refinement of PCN-600(Fe).

Chemical formula	$\text{Fe}_{3.81}\text{O}_{16}\text{C}_{72}\text{N}_6\text{H}_{36}\text{Cl}_{0.81}$
Formula weight	1482.56
Crystal system	Hexagonal
Space group	$P6/mmm$
$a/\text{\AA}$	31.269(4)
$c/\text{\AA}$	16.953(2)
Z	2
Temperature/K	298(2)
Wavelength/ \AA	0.72959
2θ range/ $^\circ$	1.0312- 18.0063
Number of reflections	298
Number of structural variables	37
R_p	0.0320
R_{wp}	0.0463
R_{exp}	0.0363
GOF	1.274

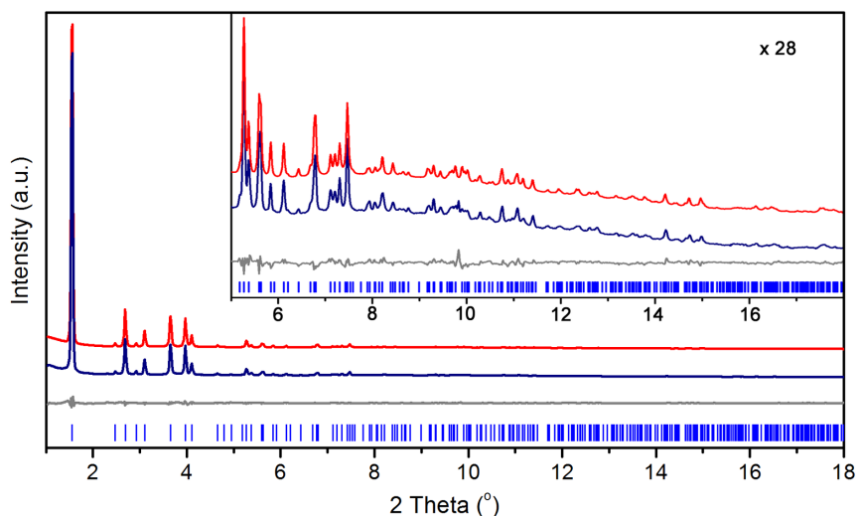


Figure 3. Rietveld refinement of PXRD for PCN-600(Co). The curves from top to bottom are simulated (red), observed (blue), and difference profiles (grey), respectively; the bars below curves indicate peak positions.

Table 2. Crystallographic data, experimental conditions for powder X-ray data collection and results of the Rietveld refinement of PCN-600(Co).

Chemical formula	$\text{Fe}_3\text{Co}_{1.13}\text{O}_{16}\text{C}_{72}\text{N}_6\text{H}_{36}$
Formula weight	1475.20
Crystal system	Hexagonal
Space group	$P6/mmm$
$a/\text{\AA}$	31.134 (5)
$c/\text{\AA}$	16.909 (3)
Z	2
Temperature/K	298(2)
Wavelength/ \AA	0.72959
2θ range/ $^\circ$	1.0312- 18.0063
Number of reflections	298
Number of structural variables	37
R_p	0.0310
R_{wp}	0.0449
R_{exp}	0.0365
GOF	1.227

2.2.4 The activation and adsorption measurements of PCN-600

Before sorption measurements, as-synthesized PCN-600 samples were washed with DMF and deionized water for several times to remove unreacted ligands and inorganic species. To optimize of the activation procedures for PCN-600, different HCl/NaOH aqueous solutions were used to treat PCN-600 samples. Afterward, the solutions were carefully decanted and the samples were washed with water and DMF for several times. Then, the samples were activated by supercritical CO₂. Then, the samples were further degassed under vacuum at 120 °C for 6 h.

The N₂ sorption isotherms of PCN-600(Fe) samples treated with different amounts of HCl/NaOH solutions were measured (Figure 4). When the pH of the aqueous solution was 2 or 11, the N₂ uptakes of PCN-600(Fe) reached the maximum, which, on the other hand, indicated the great chemical stability of PCN-600.

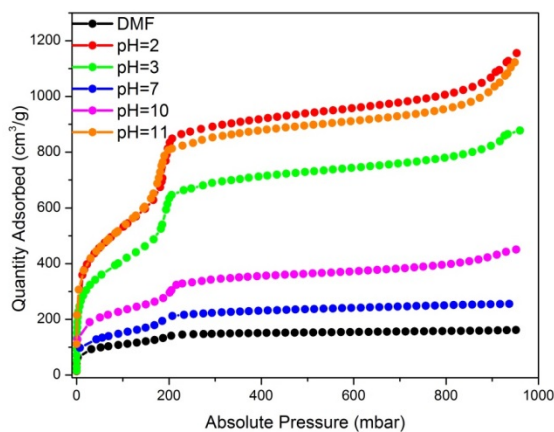


Figure 4. The N₂ sorption isotherms of PCN-600(Fe) samples at 77 K after being treated with different aqueous solutions.

Since the crystal contained very large channels, the unreacted ligands, iron clusters and the unknown coordination compounds formed by ligands and cluster might be stuck in the channels of PCN-600. This could significantly decrease its surface area and pore volume, which was shown in Figure 4 (curves for DMF and pH = 7). When the samples were immersed in acid or base solution, the H_3O^+ and OH^- could help to decompose the coordination compounds and make them removable by water and DMF. Therefore the surface area and volume of PCN-600 obviously increased after the treatments.

2.2.5 BET surface area and pore size distribution analysis of PCN-600

All the PCN-600 samples used to measure BET surface areas and pore size distributions were immersed in HCl aqueous solution (pH = 2) for 6 hours before CO_2 supercritical activation (Figure 5, 6 and Table 3).

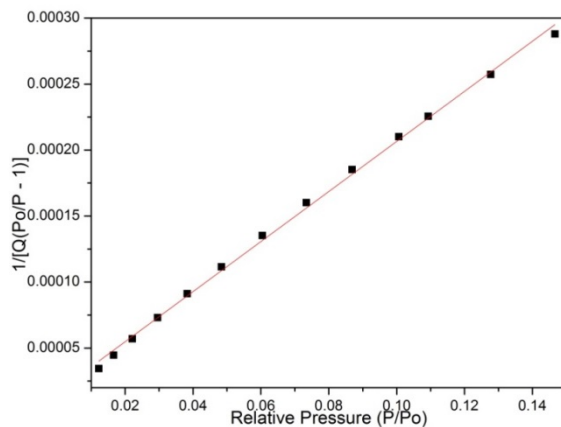


Figure 5. The plot of the linear region on the N_2 isotherm of PCN-600(Fe) for the BET equation.

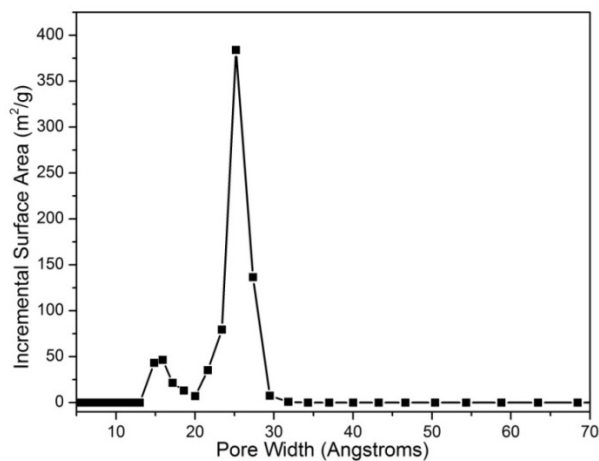


Figure 6. DFT pore size distribution for PCN-600(Fe).

Table 3. BET surface and total pore volume of PCN-600(M).

PCN-600	BET Surface Area ($\text{m}^2 \text{g}^{-1}$)	total pore volume($\text{cm}^3 \text{g}^{-1}$)
PCN-600(Mn)	2306	1.79
PCN-600(Fe)	2270	1.80
PCN-600(Co)	2340	1.65
PCN-600(Ni)	2300	1.70
PCN-600(Cu)	2350	1.77

2.2.6 Thermal Stability of PCN-600 Samples

The TGA results of PCN-601s are exhibited in Figure 7-11.

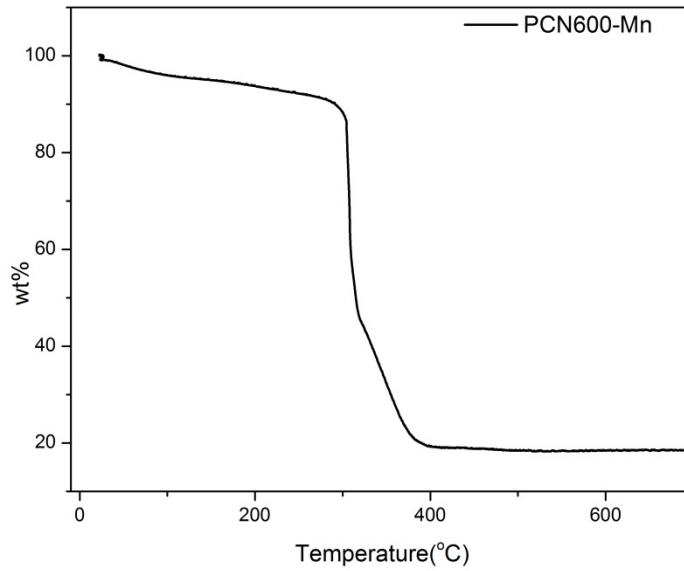


Figure 7. Thermogravimetric analysis of the activated PCN-600(Mn).

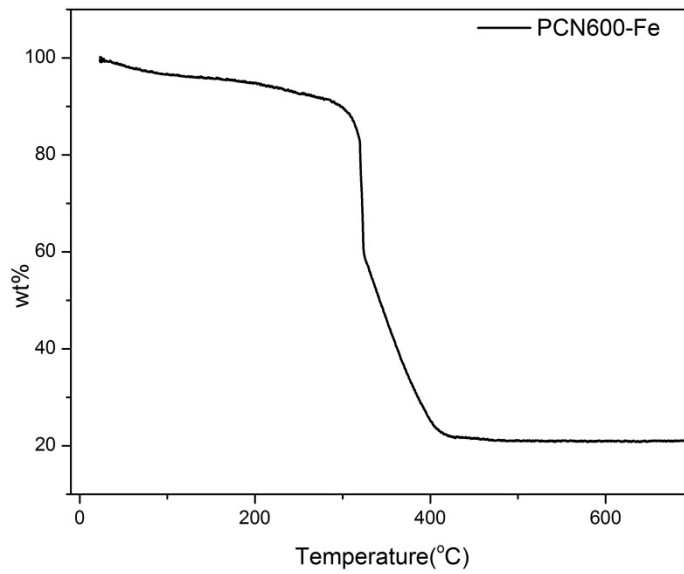


Figure 8. Thermogravimetric analysis of the activated PCN-600(Fe).

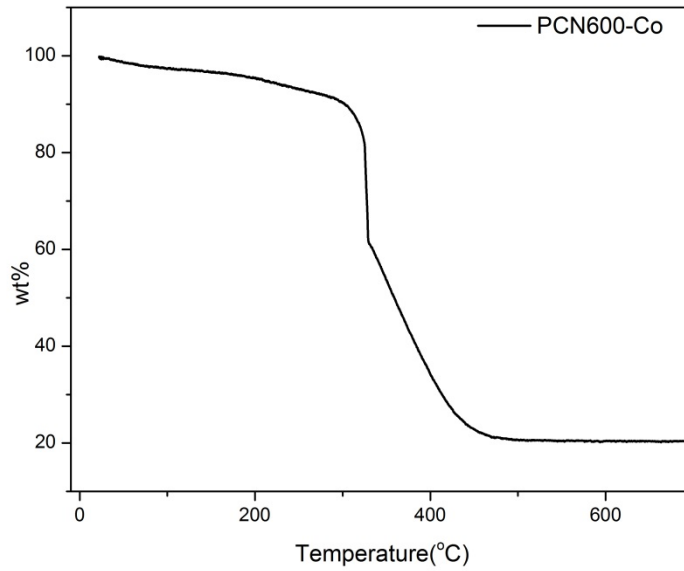


Figure 9. Thermogravimetric analysis of the activated PCN-600(Co).

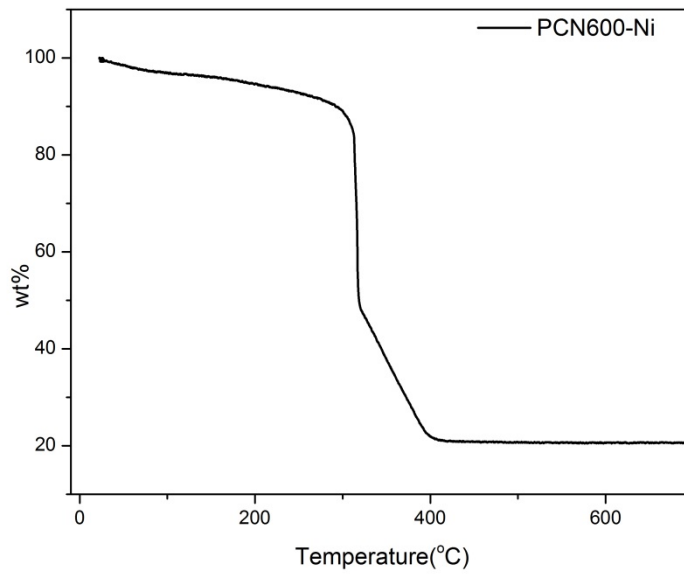


Figure 10. Thermogravimetric analysis of the activated PCN-600(Ni).

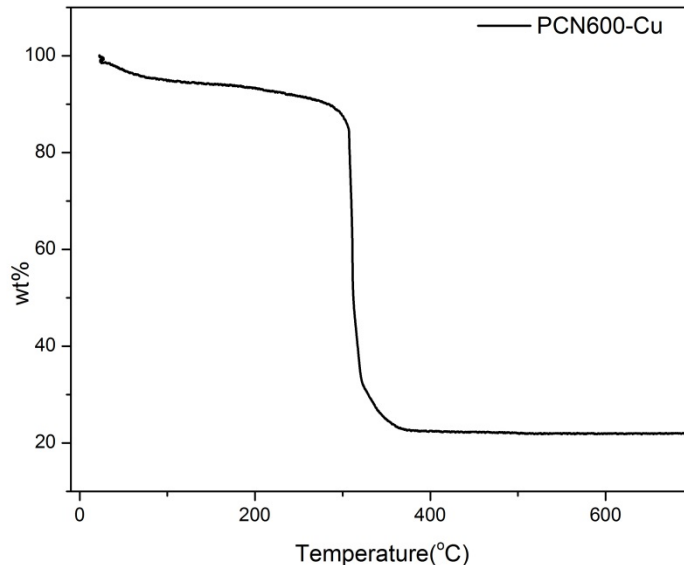


Figure 11. Thermogravimetric analysis of the activated PCN-600(Cu).

2.2.7 Catalytic activity of PCN-600(Fe) *

The co-oxidation of phenol and 4-aminoantipyrine (4-AAP) with H₂O₂ leads to the formation of a quinoneimine dye that can be monitored spectrophotometrically at 500 nm (the reported molar absorption coefficient of 12800 M⁻¹ cm⁻¹). This reaction was used to characterize the catalytic performance of PCN-600(Fe). H₂O₂ concentration was determined spectrophotometrically at 240 nm with $\epsilon = 43.6 \text{ M}^{-1} \text{ cm}^{-1}$.⁶² Kinetic measurements were carried out in time course mode by monitoring the absorbance change at 500 nm (Figure 12, 13). The Michaelis-Menten equation (eq. 1) was used.

$$V_o = \frac{V_{\max} [S]}{K_m + [S]} \quad (\text{eq. 1})$$

* The experiments to measure the catalytic activity of PCN-600(Fe) were designed and conducted by Dr. Tian-Fu Liu.

Herein, V_0 is the initial reaction rate. V_{\max} is the maximum rate conversion, which is obtained when the active sites on the catalyst are saturated with substrate. $[S]$ is the substrate concentration and K_m is the apparent Michaelis-Menten constant. The K_m and V_{\max} values can be estimated using the least squares non-linear regression to fit the plot of V vs $[S]$ to Michaelis-Menten equation.

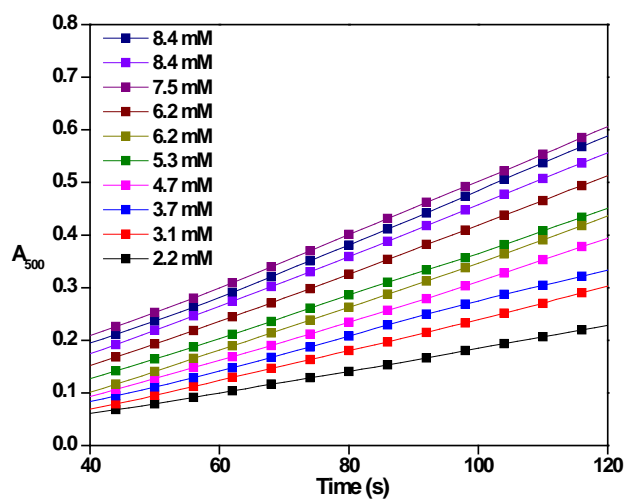


Figure 12. The time course of co-oxidation of phenol and 4-aminoantipyrine as a function of H_2O_2 concentration for PCN-600(Fe).

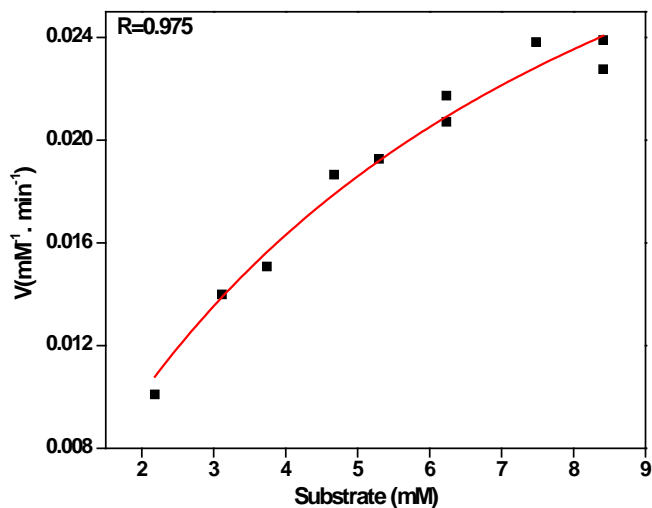


Figure 13. The initial rate of co-oxidation reaction with PCN-600(Fe) as the catalyst.

2.3 Results and Discussion

2.3.1 Topological design and Structural Description of PCN-600

The solvothermal reaction of $H_4TCPP(M)$ ($M = Mn, Fe, Co, Ni, Cu$), $[Fe_3O(OOCCH_3)_6(OH)]$ and trifluoroacetic acid in DMF at 150 °C for 12 h yielded needle-shaped single crystals of PCN-600. Although the large single crystals with length around 0.3 mm have been obtained (Figure 14a), it was difficult to determine the crystal structure against its single-crystal X-ray diffraction data due to the small size of the crystals in the other two dimensions. However, the simulated structure model of PCN-600 with a space group of $P6/mmm$ can be built by Material Studio 6.0.⁶³ The calculated PXRD pattern of the simulated structure fits the experimental results well. The unit cell parameters of $a=b=31.27 \text{ \AA}$ and $c=16.95 \text{ \AA}$ are obtained through the indexing of the

experimental high-resolution PXRD patterns. The predicted structure is ultimately validated with Rietveld refinements using the PXRD data collected from a synchrotron source. The 3D framework of PCN-600 can also be viewed as iron-carboxylate layers, which form a honeycomb-like 2D lattice in the *ab* plane, inherently pillared by TCPP ligands giving rise to a 3D framework. The 3D framework contains large hexagonal 1D channels along the *c* axis with a diameter of 3.1 nm.

2.3.2 N₂ Uptakes of PCN-600

Due to the large ligand and pore size, the activation of PCN-600 with traditional method was unsuccessful. The activation procedure of PCN-600 was optimized by solvent exchange with supercritical carbon dioxide after the sample was pre-treated by dilute acid solutions. The porosity of PCN-600 was measured by the N₂ sorption tests at 77 K (Figure 14c). The typical type IV isotherm of PCN-600(Fe) exhibits a steep increase at the point of $P/P_0 = 0.2$, suggesting the mesoporosity of this material. A N₂ uptake of 1150 cm³ g⁻¹ (STP) and a BET surface area of 2270 m² g⁻¹ were observed for PCN-600(Fe). The experimental total pore volume of this material is 1.80 cm³ g⁻¹, which is also in agreement with the value of calculated pore volume (2.28 cm³ g⁻¹). The evaluation of a DFT simulation from the N₂ sorption curve indicates that there is only one type of pore, with the diameter of 2.6 nm, assigned to the hexagonal channels, which is consistent with the crystallographic data when van der Waals contact was taken into account. PCN-600s with other metal ions at the porphyrin center show similar type IV N₂ sorption isotherms and exhibit the N₂ uptakes, surface areas, and total pore volumes up to 1170 cm³ g⁻¹ (STP), 2350 m² g⁻¹, and 1.79 cm³ g⁻¹, respectively (Table 3).

2.3.3 Chemical Stability Analysis of PCN-600

Although the requirement of supercritical carbon dioxide during the activation of PCN-600 indicates its low mechanical robustness, this will not weaken its potential in many applications in solvent-mediated systems, since the collapse of PCN-600 is mainly due to the surface tension in liquid-gas phase transition during the traditional activation procedure.⁶⁴ However, when PCN-600 is used as a heterogeneous catalyst or sensor in liquids, no liquid-gas phase transition happens. Therefore, the robustness of PCN-600 is mainly determined by its chemical stability under different reaction conditions. PCN-600 is a representative example to demonstrate how a MOF's mechanical stability and chemical stability are not always related. The experiment data shows PCN-600 has very high chemical stability compared with previously reported porphyrinic MOFs. The PXRD patterns of PCN-600 suggest the frameworks remain intact upon being immersed in solutions with pH = 2 and 11 for 24 h, indicating that no framework collapse or phase transition happens during the treatments (Figure 14a and 14b). Moreover, the N₂ sorption isotherms of the samples after treatments of the solutions with pH = 2 and pH = 11 further confirmed that PCN-600 can survive in these conditions (Figure 14c). As mentioned above, the chemical stability of PCN-600 comes from its Fe₃O(OOC)₆ cluster. Fe³⁺, with high charge/radius ratio, can form strong coordination bonds with carboxylate groups. It makes PCN-600 highly stable in water, dilute acid and base. PCN-222 (or MOF-545) is the only mesoporous porphyrinic MOF that was previously reported. However, it only shows good stability in acidic aqueous solutions.³⁴ As a

comparison, PCN-600 maintains good crystallinity in both acid and base aqueous media, which indicates its broader application ranges.

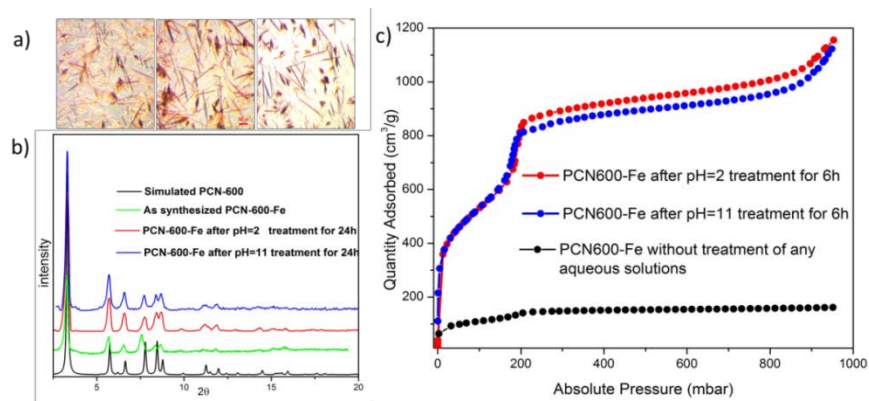
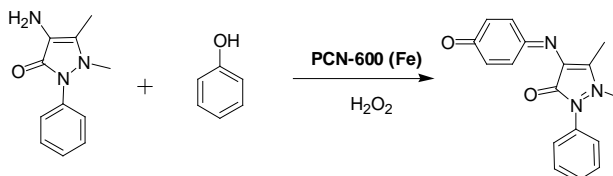


Figure 14. (a) Crystals of PCN-600(Fe) under an optical microscope. As-synthesized (left), after treatment of pH = 2 solution for 24 h (middle) and after treatment of pH = 11 solution for 24 h (right). (b) Powder X-ray diffraction pattern of PCN-600(Fe) and the samples treated with aqueous solution with pH = 2 and 11. (c) N₂ adsorption isotherms for PCN-600(Fe) at 77 K, showing the framework stability of PCN-600(Fe) upon treatments with the aqueous solutions with pH = 2 and 11.

2.3.4 Catalytic Activity Analysis of PCN-600(Fe)



Scheme 1. Reaction catalyzed by PCN-600(Fe).

The excellent chemical stability, large open channels and high concentration of porphyrins of PCN-600 endow it with high potential as a heterogeneous catalyst. The catalytic activity of PCN-600 was evaluated by its performance in the co-oxidation of phenol and 4-AAP by H_2O_2 (Scheme 1), which is also a principal reaction for phenol and cholesterol estimation.⁶² The addition of PCN-600(Fe) and H_2O_2 to the substrate solution led to the formation of quinone-imide, which gave a maximum absorbance at 500 nm. The catalytic activity of PCN-600 was analyzed by determining apparent steady-state kinetic parameters. With the suitable range of H_2O_2 concentrations, typical Michaelis-Menten curves were obtained for PCN-600(Fe). The results show PCN-600(Fe) has a very small Michaelis-Menten constant (K_m). It indicates PCN-600(Fe) has a strong affinity for the substrate and exhibits high reaction rate even with low concentration of substrates. This may be caused by the following advantages of MOFs as catalysts: First, the distribution of porphyrinic ligands throughout the framework is assured at the highly ordered microstructural level, which prevents the dimerization of active sites. Second, the porphyrinic cores were well exposed to the channel surface which is readily accessible for substrate. Third, the high surface area can adsorb the substrates from solution, which increases the “effective concentration” of the substrates around the active centers.^{65, 66} For the value of k_{cat} in PCN-600(Fe), it incorporates the rate constants for all the steps from the combination of the catalyst and the substrate, which includes the process for the product diffusing out of the channel to be detected by electronic absorption spectrometer. The low k_{cat} of PCN-600(Fe) is probably caused by the slow diffusion rate of the product in the MOF channel (Table 4).⁶⁷

Table 4. Catalytic activity of PCN-600(Fe).

Catalyst	PCN-600 (Fe)
K_m (mM)	6.37
k_{cat} (min^{-1})	0.66

2.4 Conclusions

In summary, we have demonstrated that PCN-600(Fe) is a mesoporous MOF with high chemical stability and the highest pore volume among all porphyrinic MOFs. The catalytically active sites of PCN-600(Fe) are located on the inner wall of the 1D channel with a diameter of 3.1 nm. It shows good activity for the co-oxidation of phenol and 4-AAP. The high density of active centers, large open channels, and the excellent chemical stability of PCN-600 endow this material with its great potential to be applied to heterogeneous catalysis and other applications, especially those involve basic environments.

CHAPTER III

A PYRAZOLATE-BASED PORPHYRINIC MOF WITH EXTRAORDINARY BASE-RESISTANCE*

3.1 Introduction

Owing to the fact that many applications of porphyrin involve harsh chemical conditions, chemical stability becomes crucial for porphyrinic MOFs.^{34, 35} Therefore, development of highly stable porphyrinic MOFs is a sought-after goal to extend the scope of applications for these materials. One direct strategy to overcome the vulnerability of MOFs is to enhance the strength of coordination bonds between organic linkers and metal nodes. To realize it, one of the extensively-explored methods is to choose secondary building units (SBUs) formed with high-valent metal ions and carboxylate groups, like $[\text{Zr}_6\text{O}_4(\text{OH})_4(\text{CO}_2)_{12}]$, and $[\text{M}_3\text{OX}(\text{CO}_2)_6]$ ($\text{M} = \text{Al}^{3+}$, Cr^{3+} , or Fe^{3+} ; $\text{X} = \text{OH}^-$, F^- , or Cl^-).^{22, 34, 35, 50, 51, 68-78} With this strategy, several porphyrinic MOFs with high stability in acidic and neutral aqueous solutions have been obtained, such as PCN-22X ($\text{X} = 2, 3, 4$, and 5), PCN-600 and Al-PMOF.^{34, 35, 50, 51, 57, 73}

However, these acid-resistant materials usually are fragile in basic aqueous solutions, which could severely hamper some of their applications.⁷³ A typical example is PCN-222 (or MOF-545).³⁴ It can even survive in concentrated hydrochloride acid but decomposes easily in dilute alkali solution. Since azolate-based MOFs, especially

*Reproduced with permission from Wang, K. †; Lv, X.-L. †; Feng, D.; Li, J.; Chen, S.; Sun, J.; Song, L.; Xie, Y.; Li, J.-R.; Zhou, H.-C., Pyrazolate-Based Porphyrinic Metal–Organic Framework with Extraordinary Base-Resistance. *Journal of the American Chemical Society* **2016**, *138* (3), 914-919. Copyright 2016 by American Chemical Society.

pyrazolate-based ones (pyrazolate is shortened as Pz), have been demonstrated extremely stable under basic environments,^{72, 79-86} adopting Pz-based porphyrinic organic linkers thus becomes a promising way to obtain base-resistant porphyrinic MOFs.

Herein, we demonstrate how rational top-down strategy based on topological analysis guides us to obtain a Pz-based porphyrinic MOF with excellent base-resistance, namely PCN-601, which is constructed by $[\text{Ni}_8(\text{OH})_4(\text{H}_2\text{O})_2\text{Pz}_{12}]$ (denoted as $[\text{Ni}_8]$) nodes and 5,10,15,20-tetra(1*H*-pyrazol-4-yl)porphyrin (H_4TPP) ligands (Figure 15). Experimental data confirms PCN-601 is immune to the attack of H_2O and OH^- in aqueous solutions, even at high temperature. As far as we know, it is the first identified MOF that can retain crystallinity and porosity in saturated NaOH solution at room temperature (RT) and 100 °C.

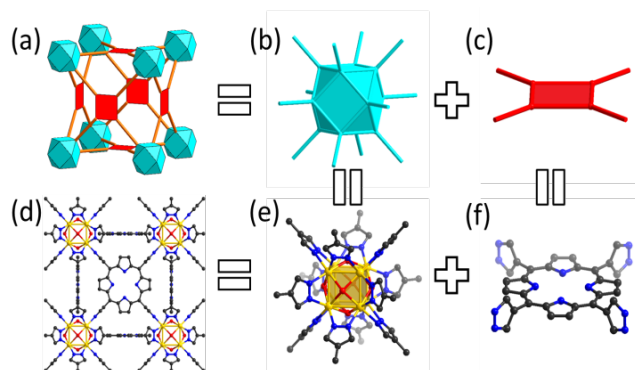
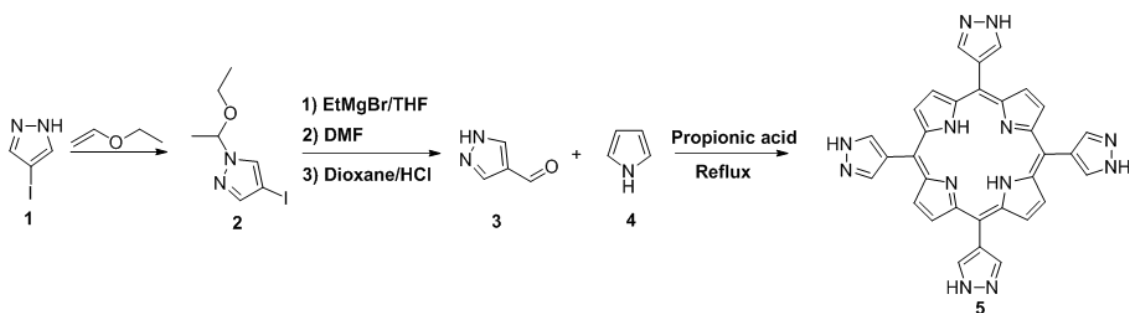


Figure 15. Structural analysis of PCN-601. (a) **ftw-a** topology; (b) O_h symmetric 12-connected node; (c) D_{4h} symmetric 4-connected node; (d) PCN-601; (e) $[\text{Ni}_8]$ cluster; (f) TPP^{4-} ligand. The Ni atoms in the porphyrin center are omitted for clarity.

3.2 Experimental Section*

3.2.1 Synthesis of H₄TPP



Scheme 2. Synthesis procedure for H₄TPP.

1-(1-Ethoxyethyl)-4-iodo-1H-pyrazole (2): 1-(1-ethoxyethyl)-4-iodo-1H-pyrazole (**2**) was obtained by a modified literature method (Scheme 2).⁸⁷ 4-Iodo-1H-pyrazole (**1**, 19.4 g, 100 mmol) was dissolved in toluene (150 mL). Ethylvinylether (20.0 mL, 211 mmol) and 2 mL HCl were added, and the mixture was heated at 50 °C. The progress of the reaction was detected by TLC. After the reaction completed, the mixture was poured into a saturated solution of NaHCO₃ (50 mL) and extracted by CH₂Cl₂ (50 mL × 3), the organic phase was dried over MgSO₄ and filtered. The product **2** was obtained by column chromatographer on Al₂O₃ (CH₂Cl₂ as eluent), yield 22.0 g (82.5 %). ¹H-NMR (300 MHz, CDCl₃) δ (ppm): 7.62 (s, 1H), 7.49 (s, 1H), 5.48 (q, 1H), 3.30-3.45 (m, 2H), 1.61 (d, 3H), 1.13 (t, 3H).

*The synthesis of H₄TPP was conducted by Xiuliang Lv.

B. 4-Formyl-1(*H*)-pyrazole (3): 4-formyl-1(*H*)-pyrazole (**3**) was synthesized by following a reported method.⁸⁸ ¹H-NMR (300 MHz, DMSO) δ (ppm): 9.87 (s, 1H), 8.25 (s, 2H).

C. 5,10,15,20-Tetra(1*H*-pyrazol-4-yl)porphyrin (H₄TPP) (5): To a refluxed propionic acid (100 mL) in a three-necked flask, 4-formyl-1(*H*)-pyrazole (**3**, 4.8 g, 0.050 mol) was added and stirred for 15 min. Then pyrrole (**4**, 3.5 mL, 0.050 mol) was added dropwise to the reaction mixture for 30 min, then the solution was refluxed for 10 h in darkness. After the reaction mixture was cooled to room temperature and stand overnight, the crystalline product of **5** was collected by filtration and washed with acetone (1.30 g, 2.26 mmol, 18.1% yield). ¹H NMR (300 MHz, DMSO) δ (ppm) 13.62 (s, 4H), 9.14 (s, 8H), 8.55 (s, 8H), -2.68 (s, 2H).

3.2.2 Synthesis of PCN-601

Ni(AcO)₂·4H₂O (800 mg), H₄TPP (400 mg), Et₃N (2 mL), and water (8 mL) in 80 mL of DMF were ultrasonically dissolved in a 150 mL high-pressure vessel. The mixture was heated to 75 °C for 4 days. After cooling down to room temperature, reddish powder in colorless solution was obtained (yield: ~96%). ICP: Ni (19.23%); EA: N (12.69%), C (34.91%), H (4.79%).

3.2.3 Structural Refinement of PCN-601*

The Rietveld refinement of PCN-601 against PXRD data was performed using Topas V4.2. The background was fitted with a 21th order Chebychev polynomial. The refinement was conducted using a Thompson-Cox-Hastings pseudo-Voigt peak profile

* The structural refinement of PCN-602 was conducted by Dr. Junliang Sun.

function, followed by refinement of unit cells and zero-shift. The rigid bodies were applied on the porphyrin ligand.

The unit cell parameters were determined directly from the high solution PXRD pattern by TREOR.⁸⁹ 30 diffraction peaks (Table 5) were used to index and no peak was not indexed. The diffraction intensities were extracted by Le Bail fitting using JANA2006.⁹⁰ We applied charge-flipping iterations on the extracted intensities using the software Superflip.⁹¹ From the best electron density maps with the lowest R values, the space group ($Pm-3m$) and the position of Ni and O were determined (Figure 16). Other framework atoms were located from the difference Fourier maps, the occupancies were confirmed by ICP and EA. According to the data of ICP, Ni^{2+} , which was located in the center of TPP^{4-} , is not full occupied, and its occupancy was 0.5911 after refinement. A few disordered small organic molecules (DMF and/or Et_3N) still remain in the pores even activated. The molecular formula is defined as skeleton formula not including disordered H_2O and a few small organic molecules in pores.

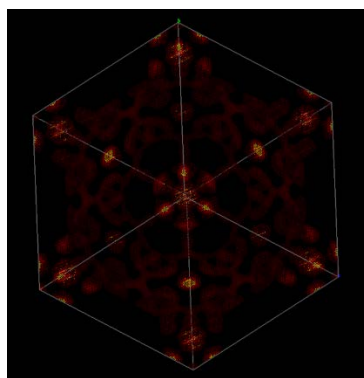


Figure 16. Electron density map of PCN-601.

Table 5. The peaks for indexing of PCN-601.

No.	Pos. [2 θ .]	FWHM Left [2 θ .]	Backgr.[counts]	d-spacing [Å]	Height [counts]
1	5.7388	0.1791	788.7	15.40036	16224.02
2	8.1041	0.1791	788.7	10.91005	8120.65
3	9.9378	0.2047	788.7	8.90075	11178.44
4	11.4455	0.1663	788.7	7.73139	2575.67
5	14.087	0.1535	788.7	6.28707	946.78
6	17.247	0.2047	713.41	5.14161	299.4
7	18.1667	0.1279	669.88	4.88334	1616.33
8	19.946	0.1535	585.68	4.45154	301.89
9	20.7877	0.2047	545.85	4.27317	154.58
10	23.0445	0.1535	446.97	3.85954	346.53
11	23.8098	0.2047	415.4	3.73719	1040.65
12	24.5267	0.2047	385.83	3.62955	439.35
13	26.5180	0.2558	303.69	3.36136	554.74
14	27.0799	0.2558	280.51	3.29287	134.29
15	28.3609	0.2047	251.08	3.14698	93.63
16	29.5122	0.2047	253.8	3.02678	440.73
17	31.7824	0.1535	259.14	2.81557	294.45
18	32.8989	0.2558	261.78	2.72253	296.12
19	33.3463	0.1791	262.83	2.68702	428.04
20	35.9165	0.2047	268.88	2.50041	311.98
21	37.8066	0.2558	273.34	2.37964	346.2
22	39.2020	0.3070	276.62	2.2981	177.8
23	41.3922	0.2047	281.78	2.18142	350.4
24	41.8385	0.2047	282.84	2.15917	354.6
25	44.2837	0.2558	288.60	2.04546	255.09
26	45.9338	0.2047	292.48	1.97575	434.47
27	46.372	0.2558	293.52	1.9581	382.69
28	47.9119	0.2558	297.14	1.8987	186.66
29	50.2099	0.3070	305.78	1.81706	104.71
30	55.2069	0.8187	213.05	1.66383	32.09

The unit cell parameter of $a = b = c = 15.43 \text{ \AA}$ was obtained through indexing of experimental high-resolution PXRD patterns (Table 6). The predicted structure was ultimately validated with Rietveld refinements (Figure 17).

Table 6. Crystallographic data, experimental conditions for PXRD data collection, and the Rietveld refinement result of PCN-601.

Chemical formula	$\text{Ni}_{9.77}\text{C}_{56.64}\text{N}_{21.24}\text{O}_{10.92}\text{H}_{43.75}$
Formula weight	1734.20
Density (calculated)	0.785
Crystal system	cubic
Space group	$Pm\bar{3}m$
$a / \text{\AA}$	15.4292(9)
Z	1
Temperature /K	298(2)
X-ray source	Cu $K\alpha 1$
Wavelength / \AA	1.540596
2θ range / $^\circ$	4.502-60.012
Number of reflections	146
Number of data points	4271
Refinement method	Rietveld refinement
R_p	0.0427
R_{wp}	0.0566
R_{exp}	0.0321
GOF	1.765
R_{bragg}	0.0130

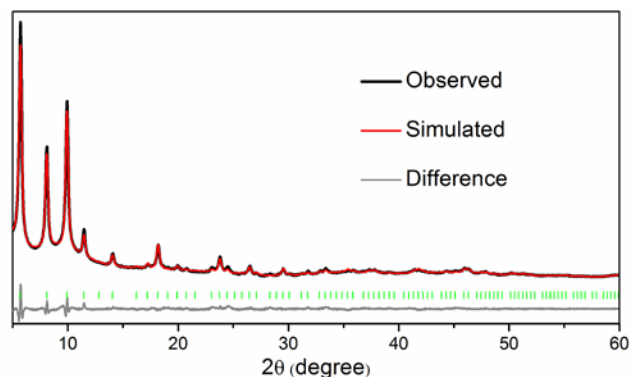


Figure 17. Rietveld refinement of PXRD data for PCN-601. The curves are simulated (red), observed (blue), and difference profiles (grey), respectively; the bars below curves indicate peak positions.

3.2.4 Gas adsorption of PCN-601

The reddish powder obtained through solvothermal reaction was washed with deionized water for several times to remove excess inorganic salt. Then the sample was washed with acetone for 3 times. After being soaked in acetone for 12 h, the sample was activated at 100 °C under vacuum for 12 h. Then, its N₂ uptake was measured at 77 K.

A BET surface area of 1309 m² g⁻¹ and a N₂ uptake of 505 cm³ g⁻¹ were observed (Figure 18 and 19). Evaluation of a DFT simulation from the N₂ sorption curve suggested the pore size distribution curve reached the maximum around 1.1 nm. The very low distributions of pores with larger diameters are possibly caused by the space between nanoparticles and the existence of defects in crystals (Figure 20).^{71, 72}

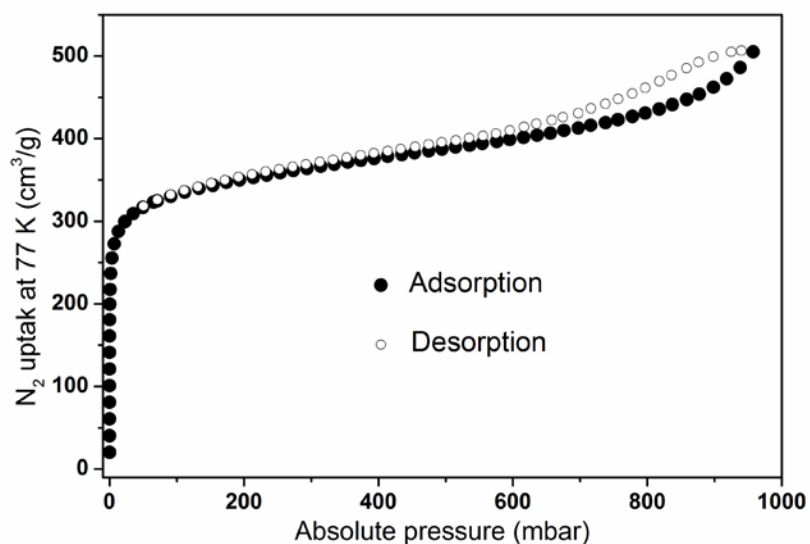


Figure 18. The N₂ adsorption/desorption isotherm of PCN-601 at 77 K.

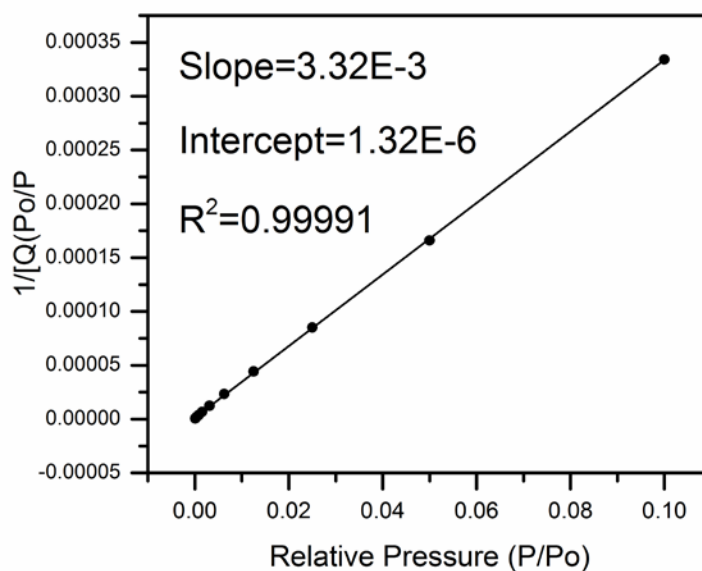


Figure 19. The plot of the linear region on the N₂ isotherm of PCN-601 for the BET equation.

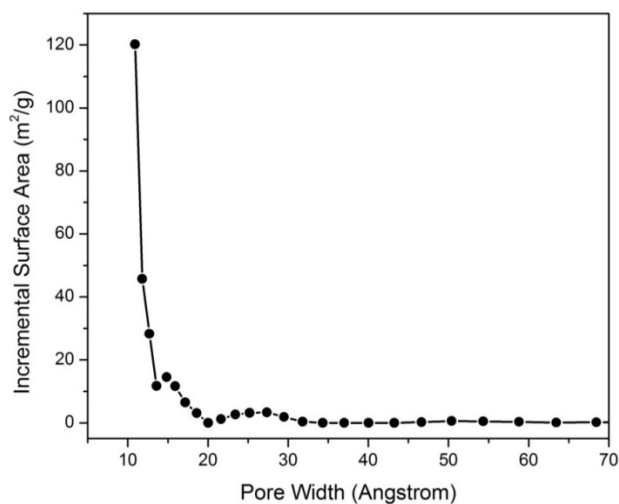


Figure 20. The DFT pore size distribution for PCN-601.

3.2.5 Chemical Stability Tests of PCN-601

PXRD measurements for stability test of PCN-601: After washed with DI water, as-synthesized PCN-601 sample, 10 mg for each batch were immersed in about 3.5 mL aqueous solution of 0.01 mmol/L HCl, 0.1 mmol/L HCl, 0.1 mol/L NaOH, 1 mol/L NaOH, 10 mol/L NaOH, and saturated NaOH (the solution is concentrated with NaOH at 20 °C, which means the concentration is around 109 g NaOH/100 g H₂O or 20 mol/L) at room temperature or 100 °C for 24 hours. The treated samples were washed with deionized water (3 times) and acetone (3 times). The powders were dried under vacuum at 100 °C for 10 h before PXRD measurements.

N₂ uptakes for stability test of PCN-601: Two batches of samples (about 100 mg for each) were immersed in 35 mL of 0.1 mM HCl solution (at room temperature) and saturated NaOH solution (at 100 °C) for 24 hours, respectively. After being washed

with water (3 times) and acetone (3 times), the samples were degassed on ASAP 2420 adsorption system for 10 h at 100 °C. These samples were then measured for N₂ sorption at 77 K.

Electronic absorption spectra for stability test of PCN-601: Two batches of samples (about 5 mg for each) were immersed in 3.5 mL of 0.1 mM HCl solution (at room temperature) and saturated NaOH solution (at 100 °C) for 24 hours, respectively. After being washed with deionized water (3 times), the samples were soaked in DMF for 24 hours. The clear solutions were taken for electronic absorption spectrum measurements. The standard solution of H₄TPP was prepared by dissolving 1 mg of H₄TPP in 20 mL of DMF.

3.1 Results and Discussion

3.3.1 Topological Design and Structural Analysis of PCN-601

Despite the well-known high robustness of Pz-based MOFs, researchers have faced great difficulty in the syntheses and structural determinations of these materials. Unlike carboxylate-based MOFs, it is very challenging to obtain single crystals or even highly crystalline powders of Pz-based MOFs.^{61, 73, 93} To solve the problem and obtain our desired product, a top-down strategy based on topological analysis is applied here. Firstly, we find out the possible topologies and structures which can theoretically incorporate our desired organic linker. After limiting our preferred products to certain networks, we then rationally choose suitable SBUs and porphyrinic ligands with proper symmetry and geometry, which can fit into targeted structures. Finally, a synthetic condition which can generate our selected SBU is adopted to obtain our expected

frameworks. In this way, the time consuming explorative synthetic work can be minimized and matched structure can be easily identified by comparison with the proposed framework.

In the first step of top-down strategy, to make searching of suitable topologies easier, we start from the simplest situation by restricting ourselves to MOFs containing only one kind of SBU, one kind of organic linker, and one kind of connecting edge, which are defined as binodal edge-transitive nets.⁹⁴ Since tetratopic porphyrinic ligands are most frequently adopted in MOFs due to their relative ease of syntheses, we further zoom into binodal edge-transitive nets with planar 4-connected node. Herein, we enumerated the reported topologies that satisfy our requirements (Figure 21, top line), analyzed the nodes that can be assigned to SBUs in corresponding nets (Figure 21, middle line, the planar 4-connected node is assigned to porphyrinic linker in each topology), and listed the reported Pz-based SBUs with the same symmetries and connectivities to corresponding nodes (Figure 21, bottom line). Through this top-down analysis, eight candidate structures with different topologies (**pto-a**, **tbo-a**, **stp-a**, **soc-a**, **csq-a**, **scu-a**, **sqc-a** and **ftw-a**) constructed by six kinds of SBUs are generated. Among these SBUs, $[\text{Ni}_8(\text{OH})_4(\text{H}_2\text{O})_2\text{Pz}_{12}]$ (shorten as $[\text{Ni}_8]$ below), a 12-connected cluster with O_h symmetry, is very intriguing to us.⁹⁵ $[\text{Ni}_8]$ owns the highest connectivity in reported Pz-based SBUs, which empirically can increase the robustness of MOFs.^{88, 93, 96} Thus a **ftw-a** network constructed by $[\text{Ni}_8]$ and Pz-based tetratopic porphyrinic ligand becomes our target.

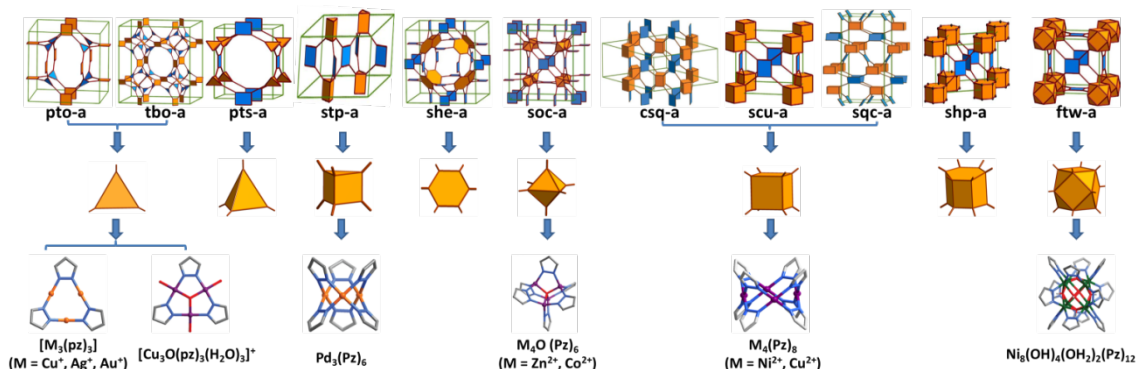


Figure 21. Top-down topology analysis: binodal edge-transitive topologies with planar 4-connected nodes (top line), the nodes assigned to SBUs in corresponding nets (middle line), and reported Pz-based SBUs with the same symmetries and connectivities to corresponding nodes (bottom line).^{83, 94, 97} For the simplification of this figure and the absence of reported planar 4-connected Pz-based SBU, the 5 topologies derived from uninodal edge-transitive nets with only 4-connected planar nodes are omitted here: **ssb-a**, **ssa-a**, **rhr-b**, **nbo-b** and **lvt-b**.

After the determination of the topology and SBU of our desired MOF, the next step is to consider the geometry details of Pz-based tetratopic porphyrinic ligand. Because the ligand is assigned to the 4-connected node with D_{4h} (or $4/mmm$) symmetry in **ftw-a** topology, only two possibilities are left here: the 4 peripheral Pz groups could be either perpendicular or parallel to the porphyrin center. To determine which type of ligands we should use, we picked PCN-221 as a reference for analysis (Figure 22). Because it is also a porphyrinic MOF with **ftw-a** topology.⁹⁸ In PCN-221, the SBU, $[Zr_8]$, is both symmetrically and geometrically equivalent to $[Ni_8]$. When the $[Zr_8O_6(CO_2)_{12}]^{8+}$ (denoted as $[Zr_8]$) is simplified into a topological node, it is compatible with two topologically identical tetratopic porphyrinic linkers with D_{4h} symmetry.⁵¹ However, only one type of linker fits when the spatial arrangement of $[Zr_8]$ and porphyrinic linker is taken into account. Therefore, to construct MOF isostructural to

PCN-221, the ligand we use should also be geometrically equivalent to the ligand in PCN-221, which is tetrakis(4-carboxyphenyl) porphyrin (H_4TCPP). As four peripheral benzoates are perpendicular to porphyrin center in $TCPP^{4-}$ (Figure 22c), we finally choose to construct our targeted MOF with H_4TPP , in which four Pz groups are forced vertical to the porphyrin center because of the steric hindrance of pyrrole rings (Figure 22i).

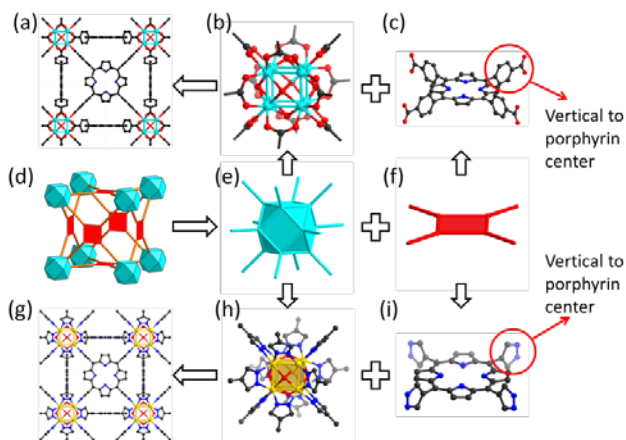


Figure 22. Topology and geometry analysis of PCN-221 and PCN-601: (a) PCN-221; (b) $[Zr_8O_6(CO_2)_{12}]^{8+}$ cluster; (c) $TCPP^{4-}$; (d) **ftw-a** topology; (e) O_h symmetric 12-connected node; (f) D_{4h} symmetric 4-connected node; (g) PCN-601 (the Ni atoms in the porphyrin center are omitted for clarity); (h) $[Ni_8]$ cluster; (i) TPP^{4-} .

In order to obtain our hypothetical structure, the last step here is to explore synthetic condition to generate the desired cluster. $[Ni_8]$, as an isolated cluster, has been synthesized with $Ni(AcO)_2 \cdot 4H_2O$, pyrazole and a weak base in MeOH.⁹⁵ Ideally, if we can conduct the synthesis under similar condition, it is quite possible to obtain our designed structure. However, given the low solubility of H_4TPP in MeOH, the solvent

for the synthesis of our targeted MOF needs to be optimized. Considering the deprotonation of H₂O and Pyrazole groups during the formation of [Ni₈] and the high pK_a values of these two species, a weak base might be necessary during the syntheses of our desired MOF. After dozens of trials, crystalline powder of PCN-601 was finally obtained through the solvothermal reaction of H₄TPP, Ni(AcO)₂·4H₂O, water and Et₃N in DMF.

3.3.2 Chemical Stability Analysis of PCN-601

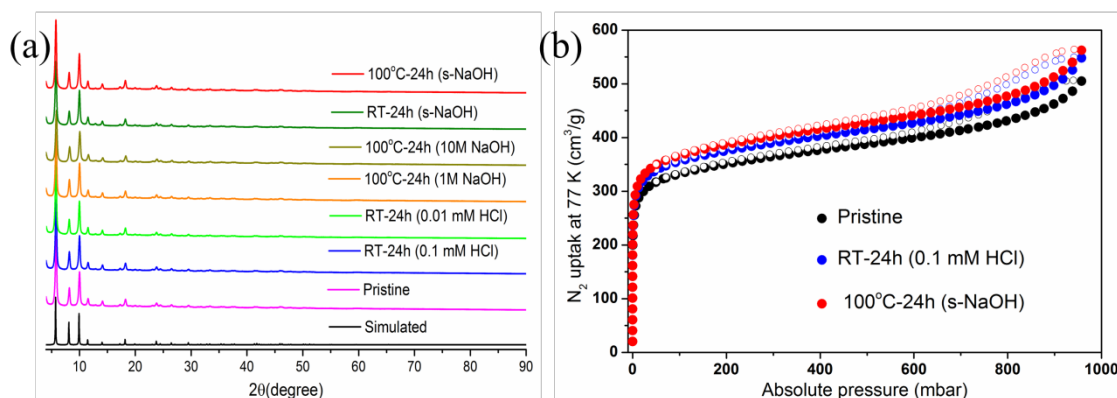


Figure 23. (a) PXRD patterns for simulated, pristine PCN-601 and PCN-601 samples treated under different conditions; (b) N₂ adsorption/desorption isotherms at 77 K of pristine PCN-601 and treated PCN-601 samples.

Chemical stability of PCN-601 was then tested by treating the material under different conditions. The PXRD patterns of all treated PCN-601 remain intact, which indicates there was no phase transition or framework collapse during treatments (Figure 23). Moreover, N₂ sorption isotherms of PCN-601 treated under the harshest conditions further confirmed its viability in these environments (Figure 23b). Though it is not very

obvious, the N_2 uptake of PCN-601 after treatments is slightly higher than that of untreated sample. We propose that it could be explained by the removal of unknown coordination species trapped inside of the framework in as-synthesized samples during the treatment of acid or base solutions, which causes a slight increase of porosity of PCN-601.⁷³ Additionally, electronic absorption spectrum suggested that the ligand of PCN-601 did not leak into DMF solution even the samples were treated under the harshest conditions, which further confirmed the intactness of PCN-601 in stability tests (Figure 24).

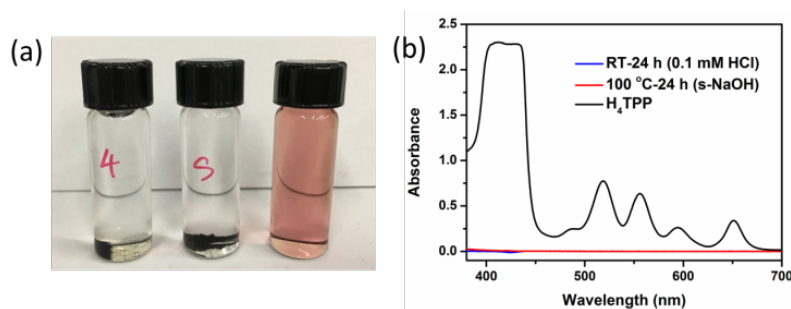


Figure 24. (a) DMF solutions with immersed PCN-601 samples being treated under 0.1 mM HCl solution at room temperature for 24 h (left) and saturated NaOH at 100 °C for 24 h (middle), respectively. In the right vial it is the standard solution of H_4TPP in DMF (1 mg/20 mL); (b) electronic absorption spectra of different DMF solutions from the vials in Figure 24(a).

We propose the extreme robustness of PCN-601 in basic aqueous media could be explained from both thermodynamic and kinetic perspectives. In basic condition, the decomposition procedure of PCN-601 could be considered as a competition between Pz^-

and OH^- (or H_2O) for Ni^{2+} . Compared with OH^- and H_2O , Pz^- has higher crystal field splitting parameter.⁹⁹ According to crystal field theory, the coordination between Ni^{2+} and Pz^- can provide more crystal field stabilization energy than that between Ni^{2+} and OH^- (or H_2O). This thermodynamically endows PCN-601 with strong resistance to the attack of H_2O and OH^- even under extremely basic condition (Figure 25). However, in acidic solution, the major driving force of MOF decomposition becomes the competition between H^+ and Ni^{2+} for Pz^- . Because of high pK_a value of pyrazole, the equilibrium is more inclined to the decomposed state (Scheme 3a). Therefore, both comparative acid-liability and extreme base-resistance of PCN-601 are related to its different thermodynamic behaviors in acid and base.

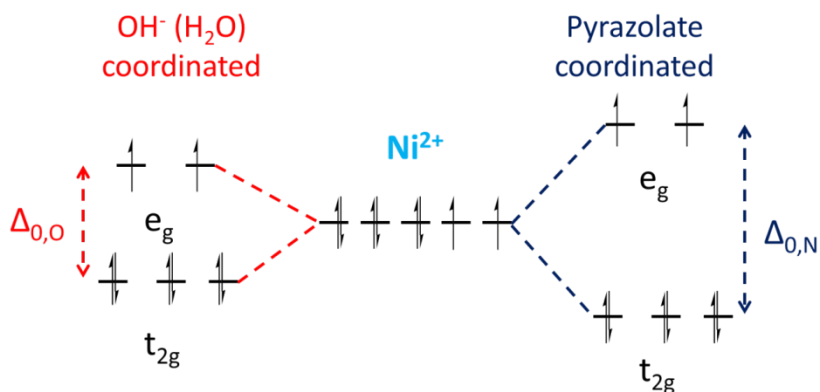
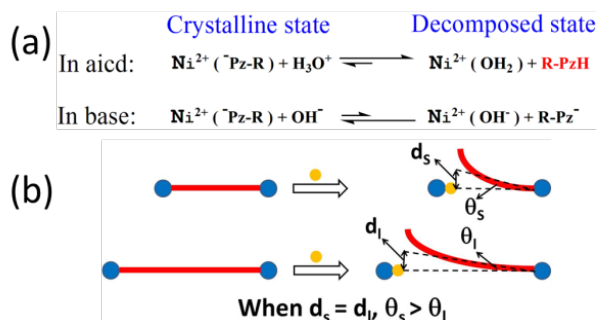


Figure 25. d orbital splitting of Ni^{2+} in octahedral coordination sphere. $\Delta_{0,O}$ is the crystal field splitting parameter in OH^- (or H_2O) coordination sphere; $\Delta_{0,N}$ is the crystal field splitting parameter in pyrazolate coordination sphere.

From kinetic aspect, the decomposition of MOFs in solutions could be generally considered as successive substitution reactions, during which defects are generated through replacing coordination moieties of ligands with small molecules or ions, akin to H_2O and OH^- .²³ Respect to the ligand, when one coordination site is displaced from the metal node, it might still stay around because of the restriction from other attached “arms” of ligands. This generates a very high “effective concentration” of coordination moiety around the defect site. Therefore the rate of reverse reaction for the dissociated site to re-attach to the metal nodes is extremely fast,¹⁰⁰ which results in the immediate structure reparation. When the connectivity of ligand is higher, this effect will become stronger, because the ligand could tolerate the displacements of more coordination sites and still keep a high rate of defect repair. We call this as “3D chelating effect” owing to its similarity to the chelating effect in the soluble coordination compounds. An similar conclusion can be drawn if SBU is considered as the leaving moiety, where high connectivity of SBU will also enhance the stability of framework. Overall, when the connectivities of the ligand and SBU are high, partially ligand dissociation can hardly result in the collapse of the whole framework because of the fast structure reparation. Therefore, such 3D chelating effect can contribute to the kinetic inertness of MOFs with highly connected SBUs and ligands. Besides the 3D chelating effect, activation energy is another critical factor in the decomposition reaction of MOFs. Scheme 3b is a model to compare the decomposition processes of two iso-reticular MOFs with short and long ligands, noted as MOF-s and MOF-l respectively. For simplification, we first assume SBUs in these two MOFs are ideally rigid. No matter the substitution reactions undergo

association or dissociation mechanism, the ligands coordinated to SBUs need to be bent in the transition states. When the displacements of the terminals of ligands in the transition states are equal in these two MOFs ($d_s = d_l$), apparently the shorter ligand will be bent more severely ($\theta_s > \theta_l$), which leads to a higher activation energy. As a result, MOF-s becomes comparatively inert.¹⁰¹ On the other hand, both the rigidities of SBUs and ligands should also be taken into account in real situations. Reasonably, SBUs and ligands with higher connectivity will be stiffer, which makes MOFs constructed by them more stable.⁵¹ Given the facts that H₄TPP is the shortest porphyrinic ligands in reported MOFs and both [Ni₈] and H₄TPP have impressively high connectivities, it is quite rational for PCN-601 to be kinetically stable. Clearly, the extreme robustness in alkali aqueous media endows PCN-601 with unique advantages in many applications, like pH sensing, catalysis and photodynamic therapy, which may have high requirement to base-resistance of MOFs.^{35, 36, 56}



Scheme 3. (a) Thermodynamic stability of PCN-601 in acid and base conditions; (b) Kinetic stability of MOFs with different length of ligands: d_s and d_l are the displacements of terminals of ligands in transition states, θ_s and θ_l are the bending angles of ligands in transition states.

3.4 Conclusions

In summary, guided by a top-down topological analysis, we rationally designed and synthesized PCN-601. Its stability has been carefully explored. PXRD patterns and N₂ uptakes suggested its crystallinity and porosity were perfectly maintained in saturated NaOH solution (20 mol/L) at RT and 100 °C. This not only pushes base-resistance of porphyrinic MOFs to the limit in aqueous media but also greatly extends the scope of applications for these materials. We also proposed thermodynamic and kinetic factors that might induce extraordinary robustness of PCN-601 in basic conditions.

CHAPTER IV

A BASE-RESISTANT METALLOPORPHYRIN MOF FOR C–H BOND

HALOGENATION*

4.1 Introduction

To exploit the desirable features of porphyrinic MOFs, the materials should be stable under the harsh chemical conditions involved in real applications. So far, the explorations of the robustness of MOFs are mainly focused on their chemical stability in water and acid aqueous solutions, but the chemical resistance of MOFs towards other species has not been extensively studied.¹⁰² Many coordinating anions (Lewis bases), such as F^- , CO_3^{2-} , and PO_4^{3-} , are also frequently involved in different kinds of reactions.¹⁰³ They are usually essential reactants or work as the compositions of buffer solutions to control the pH in the reactions catalyzed by porphyrin derivatives. Therefore, the strong resistance of porphyrinic MOFs towards these coordinating anions is highly desired to extend their application scopes.

It was found that many reported stable porphyrinic MOFs are constructed with carboxylate-based ligands and Zr^{4+} , Fe^{3+} , or Al^{3+} -based inorganic clusters.^{34, 35, 50, 51, 57, 73} In the hard-soft-acid-base (HSAB) theory, the carboxylate groups and these high-valent metal ions are categorized as hard Lewis bases and acids and can form strong coordination bonds with each other, which endows the frameworks with strong robustness. On the other hand, many coordinating anions, like F^- , CO_3^{2-} , and PO_4^{3-} , have

*Reproduced with permission from Lv, X.-L. †; Wang, K. †; Wang, B.; Su, J.; Zou, X.; Xie, Y.; Li, J.-R.; Zhou, H.-C., A Base-Resistant Metalloporphyrin Metal–Organic Framework for C–H Bond Halogenation. *Journal of the American Chemical Society* **2017**, *139* (1), 211-217. Copyright 2017 by American Chemical Society.

either small diameters or high charges. They are also classified as Lewis bases with great hardness. It leads to their strong affinity towards the high-valent metal ions, which is confirmed by the high binding constants of these anions and Zr^{4+} , Fe^{3+} , and Al^{3+} .^{104, 105} As we proposed in our previous work, the decomposition of MOFs in solutions can be considered as the competition between coordination groups of ligands and other molecules (or anions) for metal ions of the inorganic clusters inside the frameworks.²³ For the MOFs constructed by high valent metal ions, when other hard Lewis bases exist as competing species with the high concentrations in solutions, the carboxylate groups of ligands coordinated to metal ions will be easily replaced, leading to the MOF decomposition. To overcome the vulnerability of these materials in the solutions of coordinating anions with great hardness, one method is to construct MOFs with metal ions and ligands that have higher softness. With this strategy, the strong coordination interaction between the metal ions and ligands can be kept, while the affinity between coordinating anions in the solutions and metal ions inside the frameworks is weakened. This endows MOFs with high resistance to the attack of coordinating anions with great hardness.

Recently, our group reported a MOF, namely PCN-601, that fulfill all the requirements mentioned above. It is constructed by Ni^{2+} (as $[Ni_8]$ cluster $[Ni_8(OH)_4(H_2O)_2Pz_{12}]$,⁹⁵ Pz = pyrazolate) and 5,10,15,20-tetra(pyrazolate-4-yl)porphyrin(TPP^{4-}) ligand, which are soft Lewis acid and base, respectively (Figure 26d-f).¹⁰² However, the window size of the cages in PCN-601 is too small ($\sim 2.1 \times 8.0 \text{ \AA}$ after deducting van der Waals Radii). When PCN-601 is applied as a catalyst, the small

window size would slow down the diffusion of reactants or even limit the approachability of the active sites for substrates. A direct method to augment the window size and improve catalytic performance is to construct an isorecticular MOF with the rationally designed elongated ligand under the guidance of the reticular synthesis strategy (Figure 26).¹⁰⁶

We finally choose 5,10,15,20-tetrakis(4-(1*H*-pyrazol-4-yl)phenyl)porphyrin (H₄TPPP) as the ligand to construct the targeted MOF, based on two major considerations. First, in TPPP⁴⁻, each phenyl ring is vertical to porphyrin center owing to the steric hindrance of pyrazolate groups, while the pyrazolate groups prefer to be parallel to the connected phenyl rings to enlarge the conjugated system and lower the energy of the molecule. As a result, in its most stable conformation, TPPP⁴⁻ is a 4-connected *D*_{4h} symmetric ligand with 4 pyrazolate groups vertical to the porphyrin center, which is symmetrically and geometrically equivalent to TPP⁴⁻. Therefore, the construction of an isorecticular framework of PCN-601 with [Ni₈] and TPPP⁴⁻ would be possible. Second, given the fact that the pore size and stability of a MOF are usually inversely correlated, extensive elongation of the ligand could undermine the robustness of resulting framework.⁷³ Comparing to TPP⁴⁻, only one phenyl ring is inserted between the porphyrin center and pyrazolate groups in TPPP⁴⁻, which makes it one of the shortest elongated versions of TPP⁴⁻. Furthermore, the structural simulation suggests that the window size of the cages in the resulting MOF is about 6.0 × 14.0 Å, which is large enough for some substrates to diffuse inside its framework. Therefore, the MOF

constructed by TPPP^{4-} may strike the balance between cavity and robustness of the material.

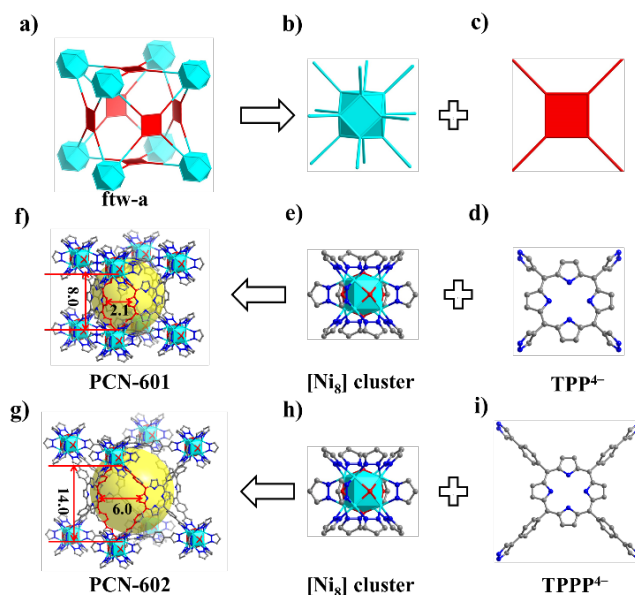


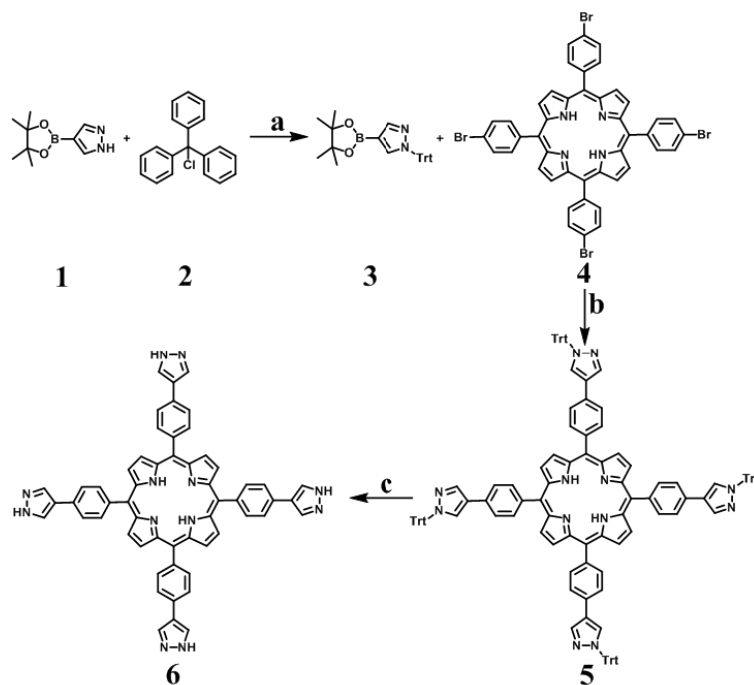
Figure 26. Reticular design and construction of PCN-602: (a) *ftw-a* topological net; (b) 12-connected node with O_h symmetry; (c) 4-connected node with D_{4h} symmetry; (d) TPP^{4-} ligand; (e and h) $[\text{Ni}_8]$ cluster; (f) structure of PCN-601 (Ni atoms in the porphyrin center are omitted for clarity); (g) proposed structure of PCN-602; and (i) TPPP^{4-} ligand.

Here, we report this rationally designed pyrazolate-based porphyrinic MOF, $[\text{Ni}_8(\text{OH})_4(\text{H}_2\text{O})_2(\text{TPPP-Ni})_3]$, namely PCN-602(Ni) (the porphyrin center is occupied by Ni^{2+}). The experimental results of its stability tests show this material has excellent robustness in aqueous solutions with OH^- , F^- , CO_3^{2-} , and PO_4^{3-} ions. An isostructural MOF with Mn^{3+} -porphyrin ligand ($\text{Mn}(\text{TPPP}^{4-})\text{Cl}$) was then prepared, assigned as PCN-602(Mn). The catalytic activity of PCN-602(Mn) has been demonstrated by its extraordinary performance as a regenerable heterogeneous catalyst in the halogenation

of hydrocarbons in basic condition. Compared with the previous method with homogeneous Mn-porphyrin catalysts,¹⁰⁷ much higher yields were achieved under a more environment-friendly condition with PCN-602(Mn).

4.2 Experimental Section*

4.2.1 Synthesis of H₄TPPP



Scheme 4. Synthetic procedure for H₄TPPP. Reagents and conditions: (a) Et₃N, CH₂Cl₂, 50 °C; (b) Pd(OAc)₂, K₃PO₄, di(1-adamantyl)-n-butylphosphine, toluene, reflux; and (c) CH₂Cl₂, CH₃OH, HCl, 45 °C.

*H₄TPPP, Mn(T₄TPPP)Cl, and Mn(H₄TPP)Cl were synthesized by Xiuliang Lv.

4-(4,4,5,5-Tetramethyl-1,3,2-dioxaborolan-2-yl)-1-trityl-pyrazole (3) : 4-(4,4,5,5-Tetramethyl-1,3,2-dioxaborolan-2-yl)-1*H*-pyrazole (8.0 g, 41.2 mmol) was dissolved in 80 mL of CH₂Cl₂ and the mixture was added to a dried 200 mL three-neck round bottom flask. Et₃N (8.0 mL) was then added dropwise to the reaction mixture and a water condenser was attached to the flask. The mixture was heated to reflux, and cautiously stirred for 30 min to give a clear colorless solution. Triphenylmethyl chloride (11.2 g, 40.4 mmol) was added to the solution and the reaction was complete in another 2 h. The reaction system was cooled to room temperature, and then poured over 100 mL of ice water in a 1 L beaker. The resulting solution was extracted three times with CH₂Cl₂ (300 mL total). The organic phase was collected and dried over anhydrous MgSO₄ for 10 min. The solvents were removed by rotary evaporation to give 4-(4,4,5,5-tetramethyl-1,3,2-dioxaborolan-2-yl)-1-trityl-pyrazole (**3**, 16.18 g, 90.0% yield based on 4-(4,4,5,5-tetramethyl-1,3,2-dioxaborolan-2-yl)-1*H*-pyrazole). ¹H NMR (400 MHz, CDCl₃): δ (ppm) 7.69 (s, 1H), 7.43 (s, 1H), 7.32 (m, 9H), 7.14 (m, 6H), 1.20 (s, 12 H). ¹³C NMR (400 MHz, CDCl₃): δ (ppm) 145.9, 143.2, 138.8, 130.1, 127.8, 127.7, 83.3, 24.8. MS (ESI) calcd for C₂₈H₂₉BN₂O₂ m/z = 436.2, found 437.2 ([M + H]⁺). FT-IR (cm⁻¹): 3005 (m), 2975 (m), 2880 (m), 1650 (m), 1435 (m), 1375 (m), 958 (m).

5,10,15,20-Tetrakis(4-bromophenyl)porphyrin (4) : 4-Bromobenzaldehyde (18.5 g, 100 mmol) and pyrrole (7.2 mL, 100 mmol) were dissolved in 200 mL of dried propionic acid, and the solution was heated to reflux and stirred for 12 h. The reaction mixture was cooled down to room temperature and filtered subsequently to remove the impurities. Then the solid was washed by 200 mL of acetone to obtain compound **4** as

crystalline powder (5.0 g, 21.5% yield based on 4-bromobenzaldehyde). ^1H NMR (400 MHz, CDCl_3): δ (ppm) 8.65 (s, 8 H), 8.01 (d, 8 H), 7.54 (d, 8H), -2.04 (s, 2 H). ^{13}C NMR (400 MHz, CDCl_3): δ (ppm) 140.9, 135.9, 130.1, 122.8, 119.0. MS (ESI) calcd for $\text{C}_{44}\text{H}_{26}\text{N}_4\text{Br}_4$ $m/z = 929.7$, found 930.7 ($[\text{M} + \text{H}]^+$). FT-IR (cm^{-1}): 3320 (s), 3022 (m), 1472 (s), 1348 (m), 964 (m), 782 (m), 724 (m).

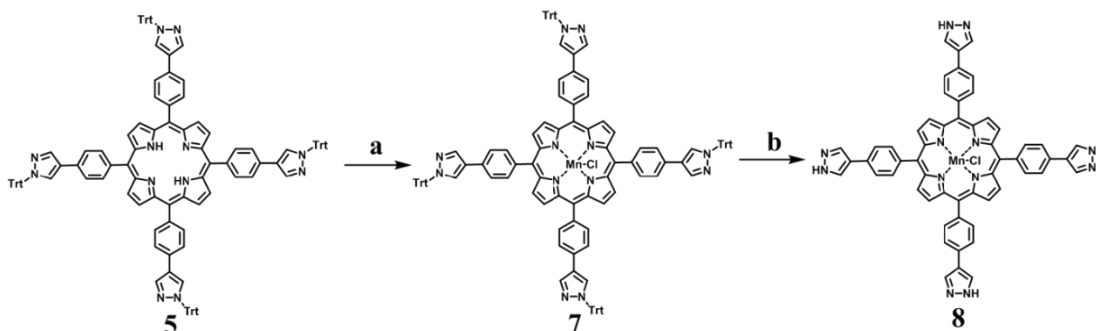
5,10,15,20-Tetrakis(4-(1-trityl-pyrazol-4-yl)phenyl)porphyrin (TPPP-Trt)

(5): Compound **4** (0.930 g, 1 mmol) and **3** (2.62 g, 6 mmol) were dissolved in 100 mL of degassed toluene. $\text{Pd}(\text{OAc})_2$ (45 mg, 0.2 mmol, 20 mol%), di(1-adamantyl)-*n*-butylphosphine (144 mg, 0.4 mmol), and $\text{K}_3\text{PO}_4 \cdot 3\text{H}_2\text{O}$ (2.128 g, 8 mmol) were then added. The reaction system was heated to reflux and stirred for 8 h under N_2 atmosphere. After the reaction completed, the mixture was cooled to room temperature. 100 mL of water was added to the crude mixture and the solution was extracted three times with CHCl_3 (3×200 mL). The organic phase combined and dried with MgSO_4 for 10 min, and evaporated to dry. The solid residue was dissolved in a small amount of 2:1 CHCl_3 -PE mixture, and then separated by column chromatography (CH_2Cl_2 to $\text{CH}_2\text{Cl}_2/\text{EA} = 10:1$). 5,10,15,20-Tetrakis(4-(1-trityl-pyrazol-4-yl)phenyl)porphyrin (**5**) was isolated as a purple solid (1.57 g, 85% yield based on **4**). ^1H NMR (400 MHz, CDCl_3): δ (ppm) 8.81 (s, 8 H), 8.23 (d, 8H), 7.30-7.70 (m, 68 H), -2.03 (s, 2 H). ^{13}C NMR (400 MHz, CDCl_3): δ (ppm) 145.9, 144.0, 143.0, 139.8, 137.2, 135.3, 136.9, 135.0, 130.3, 128.9, 127.8, 83.5. MS (ESI) calcd for $\text{C}_{132}\text{H}_{94}\text{N}_{12}$ $m/z = 1846.8$, found 1847.8 ($[\text{M} + \text{H}]^+$). FT-IR (cm^{-1}): 3062(m), 1717 (s), 1450 (m), 1357 (s), 958 (m), 752 (m).

5,10,15,20-Tetrakis(4-(1H-pyrazol-4-yl)phenyl)porphyrin (H₄TPPP) (6) :

Compound **5** (1.215 g, 1 mmol) was suspended in 60 mL of CH₂Cl₂:MeOH (1:1) mixed solvent in a 150 mL round-bottom flask. 20 mL of 2 M HCl aqueous solution was slowly added to the suspension and the resulting mixture was stirred at 45 °C for 6 h. The reaction system was cooled to room temperature and the solvents were removed by rotary evaporation. The raw product was washed successively with deionized water (~70 mL), methanol (~70 mL), and chloroform (~70 mL). The resulting purple solid was dried in *vacuo* to afford 5,10,15,20-tetrakis(4-(1H-pyrazol-4-yl)phenyl)porphyrin (H₄TPPP) (**6**), 0.79 g, 90 % yield based on **5** (Scheme 4). ¹H NMR (400 MHz, DMSO-d⁶) δ (ppm): 13.90 (s, 4H), 8.95 (s, 8H), 8.50 (s, 4H), 8.20 (d, 12H), 8.07 (d, 8H), -2.84 (s, 2H). ¹³C NMR (400 MHz, DMSO-d⁶) δ (ppm): 143.3, 140.1, 137.5, 135.8, 135.0, 130.2, 129.5, 128.0. MS (ESI) calcd for C₅₆H₃₈N₁₂ m/z = 878.3, found 879.3 ([M + H]⁺). FT-IR: 3314 (m), 3225 (m), 1709 (m), 1562 (m), 1463 (m), 1355 (m), 1227 (m), 951 (m), 794 (s); electronic absorption spectrum (λ_{max} (nm), relative intensity (%)) in DMF: 425 (100), 519 (6.5), 557 (5.1), 650 (2.8).

4.2.2 Synthesis Mn(H₄TPPP)Cl



Scheme 5. Synthesis of Mn(H₄TPPP)Cl. Reagents and conditions: (a) MnCl₂·4H₂O, DMF, reflux and (b) CH₂Cl₂, CH₃OH, HCl, 45 °C.

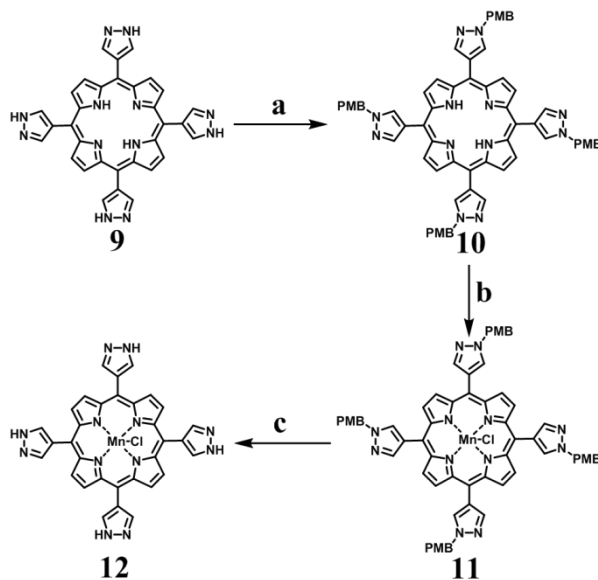
5,10,15,20-Tetrakis(4-(1-trityl-pyrazol-4-yl)phenyl)porphyrin-Mn chloride

(Mn(TPPP-Trt)Cl) (7): Compound **5** (1.215 g, 1.0 mmol) and MnCl₂·4H₂O (2.5 g, 12.8 mmol) were dissolved in 100 mL of DMF in a 250 mL round-bottom flask (Scheme 5). The solution was heated to reflux and stirred for 12 h. After the reaction system was cooled to room temperature, 150 mL of water was added. The resultant precipitate was filtered and washed with 50 mL of water for twice. The obtained solid was dissolved in 300 mL of CHCl₃, followed by washing three times with water (3 × 100 mL). The organic layer was dried over MgSO₄ for 10 min and evaporated to afford 5,10,15,20-Tetrakis(4-(1-trityl-pyrazol-4-yl)phenyl)porphyrin-Mn(III) chloride (Mn(TPPPTrt)Cl) (**7**, 1.0 g, 78% yield based on **5**). MS (ESI) calcd for C₁₃₂H₉₂ClMnN₁₂ m/z = 1934.7, found 1899.7 ([M - Cl]⁺). FT-IR: 3055 (m, ArH), 1661 (m), 1492 (m), 1443 (m), 1364

(m), 1157 (m), 1007 (s); electronic absorption spectrum (λ_{max} (nm), relative intensity (%)) in DMF: 473 (100), 574 (10), 615 (12).

5,10,15,20-Tetrakis(4-(1*H*-pyrazol-4-yl)phenyl)porphyrin-Mn chloride (Mn(H₄TPPP)Cl) (8) : Compound **7** (1.0 g) was suspended in 60 mL of CH₂Cl₂:CH₃OH (1:1) mixed solvent in a 150 mL round-bottom flask. 20 mL of 2 M HCl was slowly added to the suspension and the mixture was stirred at 45 °C for 6 h. The reaction mixture was cooled to room temperature and the solvents were removed by rotary evaporation. The raw product was washed successively with deionized water (~70 mL), methanol (~70 mL), and chloroform (~70 mL). The resulting dark green solid was dried under vacuum to afford 5,10,15,20-tetrakis(4-(1*H*-pyrazol-4-yl)phenyl)porphyrin-Mn chloride (Mn(H₄TPPP)Cl) (**8**, 0.40 g, 80% yield based on **7**). MS (ESI) calcd for C₅₆H₃₆ClMnN₁₂ m/z = 966.2, found 931.3 ([M – Cl]⁺). FT-IR: 3245 (m), 1703 (m), 1654 (s), 1359 (m), 1221 (m), 1014 (m), 946 (m), 808 (m); electronic absorption spectrum (λ_{max} (nm), relative intensity (%)) in DMF: 473 (100), 576 (10), 616 (11).

4.2.3 Synthesis of Mn(H₄TPP)Cl



Scheme 6. Synthesis of Mn(H₄TPP)Cl. Reagents and conditions: (a) PMBCl, DMF, K₂CO₃, reflux; (b) MnCl₂·4H₂O, DMF, reflux; (c) CAN, CH₃CN, 60 °C.

5,10,15,20-Tetrakis(1-(4-methoxybenzyl)-pyrazol-4-yl)porphyrin (**10**) :

5,10,15,20-Tetra(1H-pyrazol-4-yl)porphyrin (H₄TPP, **9**, 0.574 g, 1 mmol) was dissolved in 100 mL of DMF and was added to a dried 200 mL round bottom flask. K₂CO₃ (1.1 g, 8.0 mmol) was then added to the reaction mixture. The mixture was heated at 70 °C and stirred for 30 min to give a purple solution. 4-Methoxybenzylchloride (PMBCl 0.81 mL, 6 mmol) was then added to the mixture, and the reaction mixture was stirred for another 2 h. After the reaction completed, the mixture was cooled to room temperature and then poured over 100 mL of ice water in a

1 L beaker. The mixture was extracted three times with 100 mL CHCl₃ (300 mL total). The organic phase was dried over anhydrous MgSO₄ for 10 min and the solvent was removed by rotary evaporation to give 5,10,15,20-tetrakis(1-(4-methoxybenzyl)-pyrazol-4-yl)porphyrin (**10**, 0.9 g, 85% yield based on **9**). ¹H NMR (400 MHz, CDCl₃): δ (ppm) 8.97 (s, 8H), 8.28 (s, 4H), 8.06 (s, 4H), 7.41 (d, 8H), 6.93 (d, 8H), 5.53 (s, 8H), 3.77 (s, 12 H), -2.81 (s, 2H). ¹³C NMR (400 MHz, CDCl₃): δ (ppm) 159.8, 144.1, 133.3, 129.8, 128.6, 123.1, 114.6, 110.6, 56.1, 55.4. MS (ESI) calcd for C₆₄H₅₄N₁₂O₄ m/z = 1054.4, found 1055.4 ([M + H]⁺). FT-IR: 3108 (w), 2921 (m), 2843 (m), 1612 (m), 1553 (m), 1504 (m), 1248 (s), 1170 (m), 1032 (m), 953 (m), 805 (m); electronic absorption spectrum (λ_{max} (nm), relative intensity (%)) in DMF: 425 (100), 519 (6.5), 557 (5.1), 650 (2.8).

5,10,15,20-Tetrakis(1-(4-methoxybenzyl)-pyrazol-4-yl)porphyrin-Mn(III)

chloride (11): Compound **10** (0.9 g, 0.85 mmol) and MnCl₂·4H₂O (2.0 g, 10.0 mmol) were dissolved in 100 mL of DMF in a 250 mL round bottom flask. The solution was heated to reflux and stirred for 12 h. After the mixture was cooled to room temperature, 150 mL of water was added. The resultant precipitate was filtered and washed with 50 mL of water for twice. The obtained solid was dissolved in 300 mL of CHCl₃, followed by washing three times with water (3 × 100 mL). The organic layer was dried over MgSO₄ for 10 min and evaporated to afford 5,10,15,20-tetrakis(1-(4-methoxybenzyl)-pyrazol-4-yl)porphyrin-Mn(III) chloride (**11**, 0.95 g, 95% yield based on **10**). MS (ESI) calcd for C₆₄H₅₂ClMnN₁₂O₄ m/z = 1142.3, found 1107.3 ([M - Cl]⁺). FT-IR: 2921 (m), 2843 (m), 1615 (m), 1550 (m), 1500 (m), 1248 (s), 1170 (m), 1032 (m), 1005(s), 953

(m), 805 (m); electronic absorption spectrum (λ_{\max} (nm), relative intensity (%)) in DMF: 473 (100), 574 (8.5), 615 (10).

5,10,15,20-Tetra(1*H*-pyrazol-4-yl)porphyrin-Mn(III) chloride (12) :

Compound **11** (0.95 g) and Ceric ammonium nitrate (CAN, 22.0 g, 40 mmol) were suspended in 150 mL of CH₃CN. The solution was heated at 60 °C and stirred for 5 h. After cooling down to room temperature, 100 mL of water was added in to reaction system. The resultant precipitate was filtered and washed with CHCl₃ (2 × 100 mL), acetone (2 × 100 mL), DMF (2 × 20 mL) to afford 5,10,15,20-tetra(1*H*-pyrazol-4-yl)porphyrin-Mn(III) chloride (**12**, 0.3 g, 78% yield based on **11**) as dark green powder (Scheme 6). MS (ESI) calcd for C₃₂H₂₀ClMnN₁₂ m/z = 662.1, found 627.1 ([M - Cl]⁺). FT-IR: 3163 (s), 1647 (m), 1559 (m), 1490 (m), 1372 (m), 1214 (m), 978 (m), 801 (m); electronic absorption spectrum (λ_{\max} (nm), relative intensity (%)) in DMF: 473 (100), 574 (10), 615 (12).

4.2.4 Synthesis of MOFs

Synthesis of PCN-602(Ni): Ni(AcO)₂·4H₂O (8 mg, 32.3 mmol), H₄TTPP (10 mg, 17.4 mmol), and deionized (DI) water (1.2 mL) in 2 mL of DMF were mixed and ultrasonically dissolved in a 5 mL high-pressure vessel. The resulting mixture was sealed and heated at 120 °C for 24 h. After cooling down to room temperature, reddish crystalline powder of PCN-602(Ni) was collected by filtration (8 mg). ICP: Ni (18.732%); EA: N (12.77%), C (57.25%), H (4.359%). The FT-IR spectrum of as-synthesized PCN-602(Ni) is shown in Figure 27. The PXRD pattern of PCN-602(Ni) is shown in Figure 36.

Synthesis of PCN-602(Mn) : Ni(AcO)₂·4H₂O (6 mg, 24.2 mmol), Mn(H₄TPPP)Cl (10 mg, 15.0 mmol), DI water (2.5 mL) and DMF (1.5 mL) were mixed in a 5 mL high-pressure vessel. The mixture was sealed and heated at 120 °C for 24 h. After cooling down to room temperature, dark green crystalline powder of PCN-602(Mn) was collected by filtration (8 mg). ICP: Ni (18.732%); EA: N (12.77%), C (57.25%), H (4.359%). FT-IR spectrum of as-synthesized PCN-602(Mn) is shown in Figure 28. The PXRD pattern of PCN-602(Ni) is shown in Figure 37.

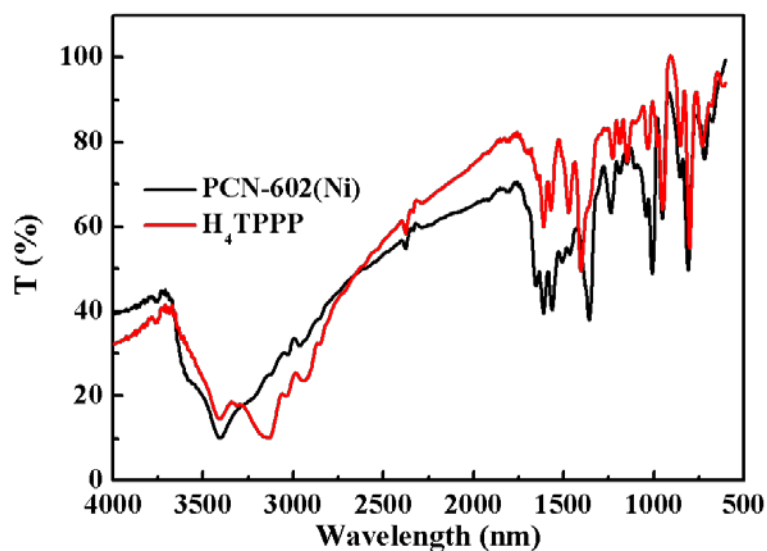


Figure 27. FT-IR spectra of H₄TPPP and PCN-602(Ni).

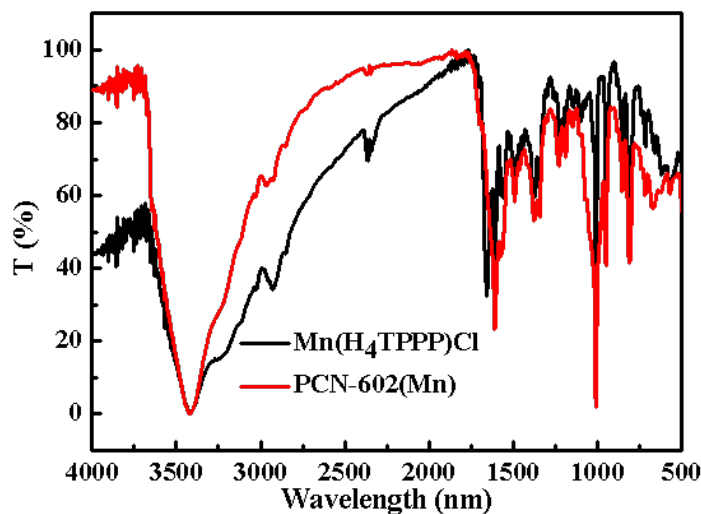


Figure 28. FT-IR spectra of Mn(H₄TPPP)Cl and PCN-602(Mn).

Synthesis of PCN-222(Fe), -224(Co), and -600(Mn): These three MOFs were synthesized according to the reported procedures and structurally characterized by PXRD, respectively.^{34, 50, 73} Well matching between the simulated and measured PXRD patterns shows the success of synthesizing the target material, as well as its phase purity in each case (Figure 29-31).

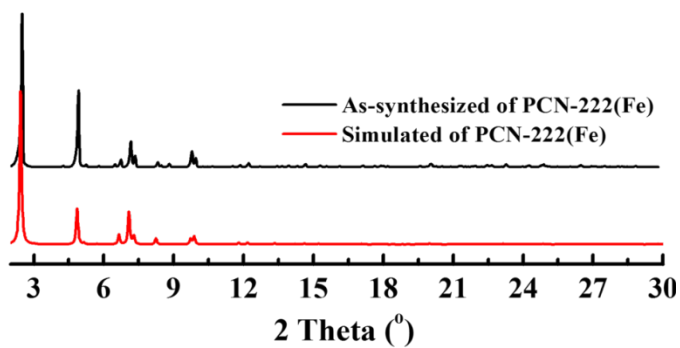


Figure 29. PXRD profiles of simulated and experimental PCN-222(Fe).

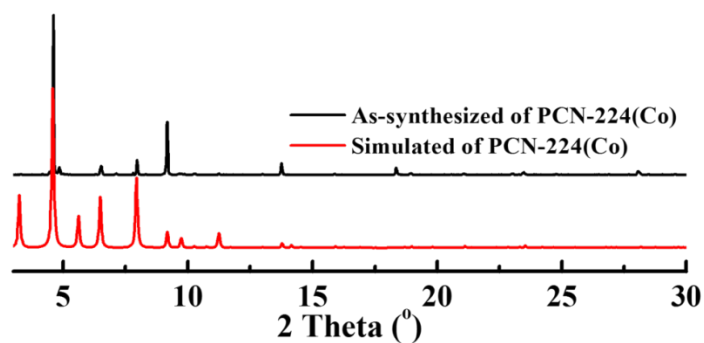


Figure 30. PXRD profiles of simulated and experimental PCN-224(Co).

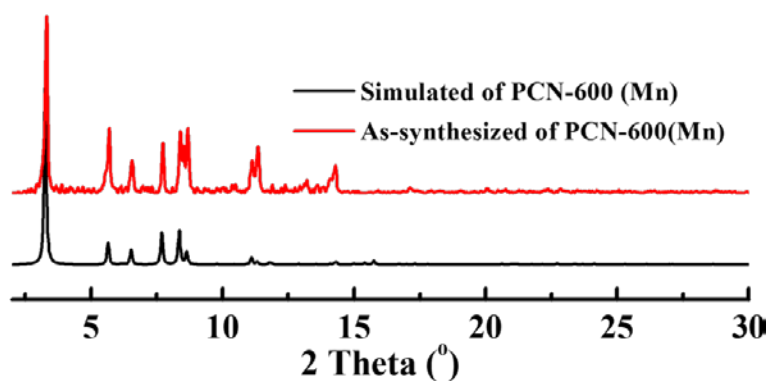


Figure 31. PXRD profiles of simulated and experimental PCN-600(Mn).

Synthesis of PCN-601(Mn) : $\text{Ni}(\text{AcO})_2 \cdot 4\text{H}_2\text{O}$ (80 mg, 32.1 mmol) and $\text{Mn}(\text{H}_4\text{TPP})\text{Cl}$ (45 mg) in 10 mL of DMF were ultrasonically dissolved in a 25 mL high pressure-vessel. The vessel was heated at 130 °C for 1 day. After cooling down to room temperature, dark green powder in colorless solution was collected by filtration. PXRD and N_2 adsorption characterizations are shown in Figure 32 and 33, respectively.

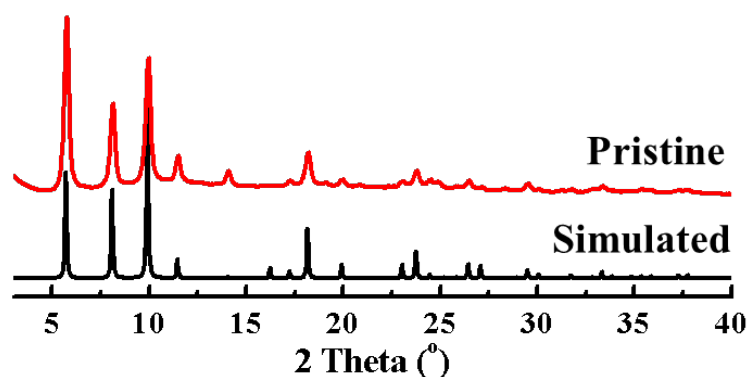


Figure 32. PXRD profiles of simulated and experimental PCN-601(Mn).

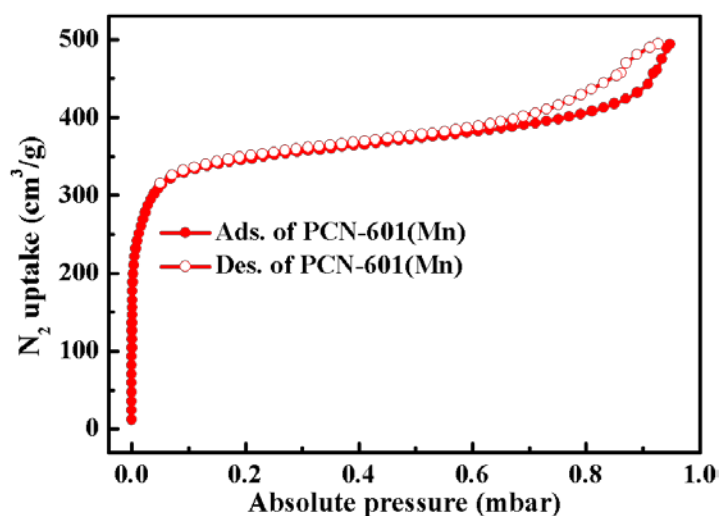


Figure 33. The N₂ adsorption/desorption isotherms of PCN-601(Mn) at 77 K.

4.2.5 Thermal Stability of PCN-602(M) (M = Ni or Mn)

Thermogravimetry analysis suggests a thermal stability of PCN-602(Ni) and -602(Mn) up to 280 °C, at which point it begins to decompose as shown in Figure 34 and 35, respectively.

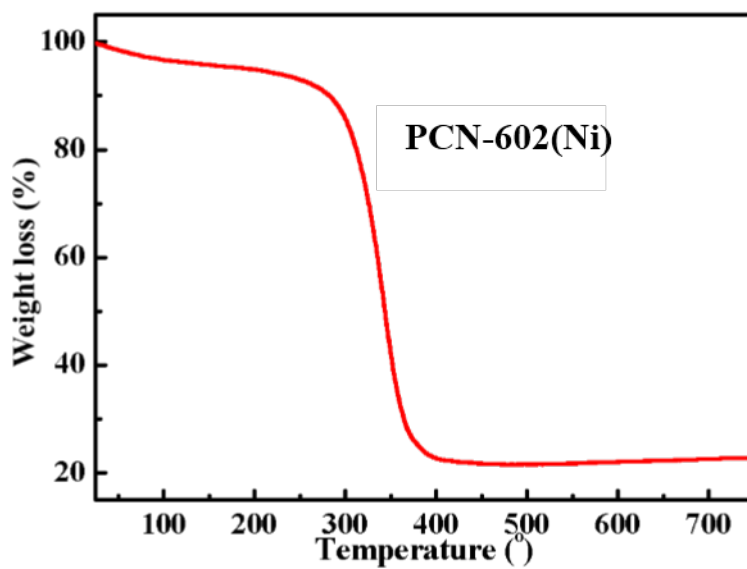


Figure 34. The thermogravimetric analysis of as-synthesized PCN-602(Ni).

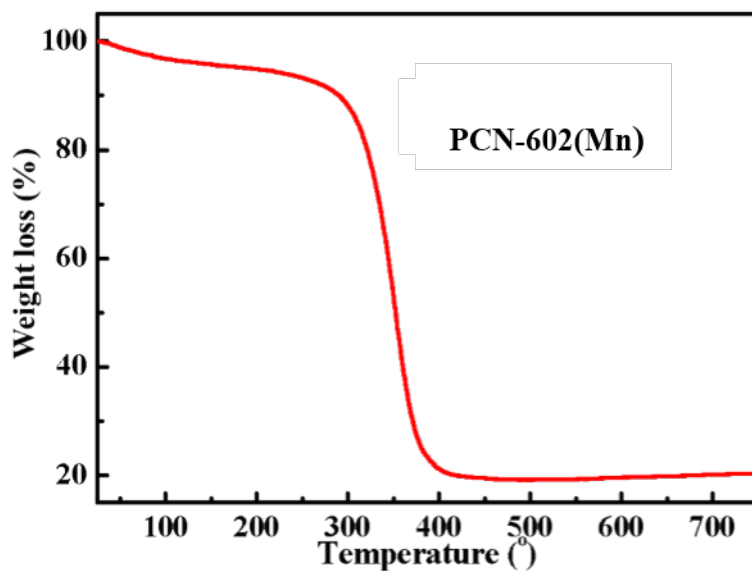


Figure 35. The thermogravimetric analysis of as-synthesized PCN-602(Mn).

4.2.6 Powder X-Ray Diffraction of PCN-602(M) (M = Ni or Mn)

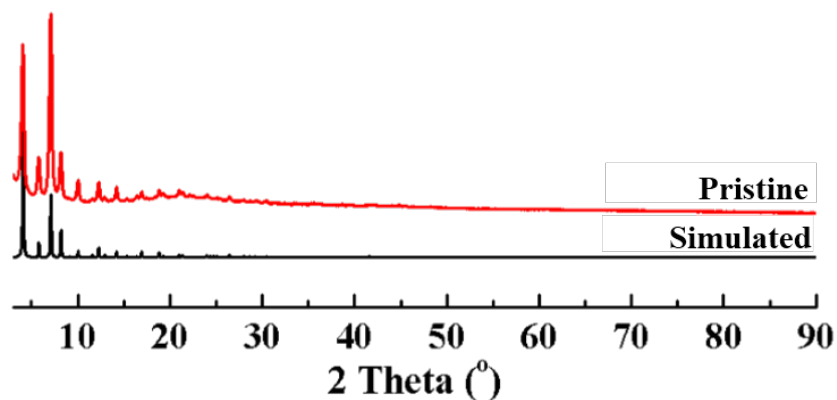


Figure 36. PXRD profiles of simulated and pristine of PCN-602(Ni).

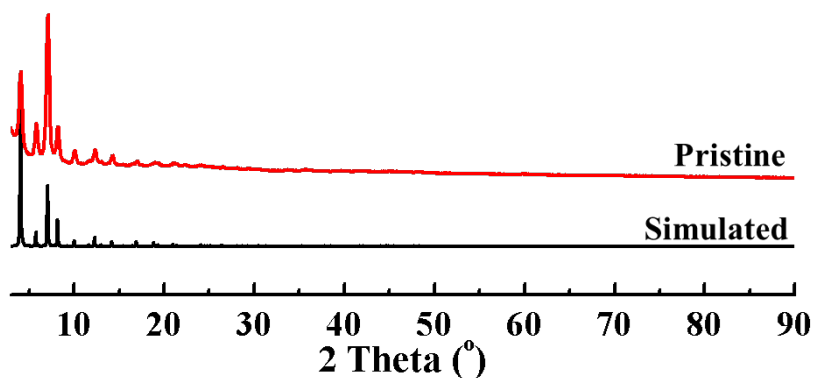


Figure 37. PXRD profiles of simulated and pristine of PCN-602(Mn).

4.2.7 N₂ Adsorption/Desorption Isotherms of PCN-602(M) (M = Ni or Mn)

Sample activation: As-synthesized powders (~100 mg) of PCN-602(M) (M = Ni or Mn) were washed with 100 mL DMF once and 100 mL of deionized water three times to remove excess inorganic salts. Then the samples were further washed with acetone

three times (3×200 mL). Before N_2 sorption experiment, the acetone-washed samples were activated under dynamic vacuum at 100 °C for 12 h (Figure 38-43).

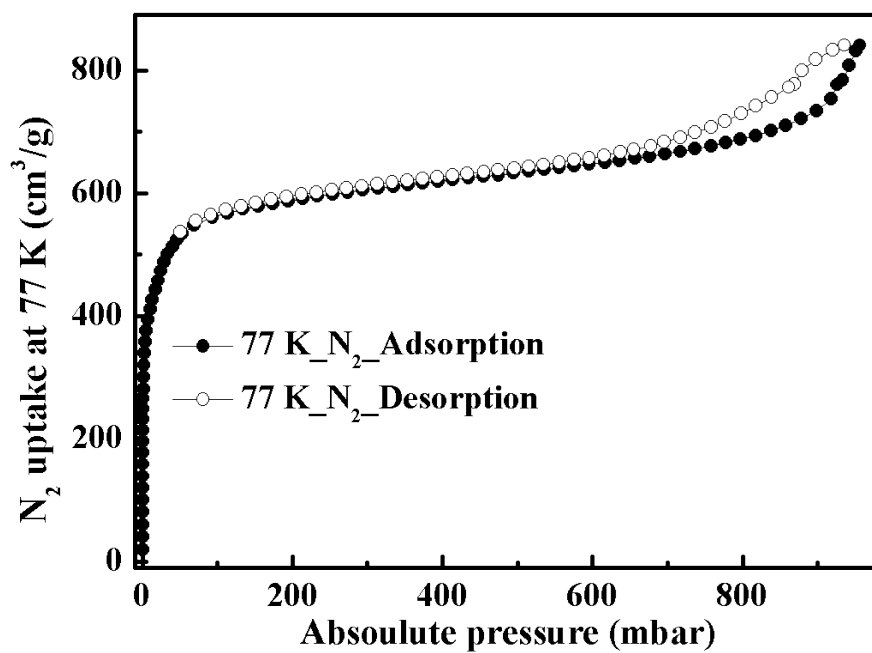


Figure 38. N_2 adsorption/desorption isotherm of PCN-602(Ni) at 77 K.

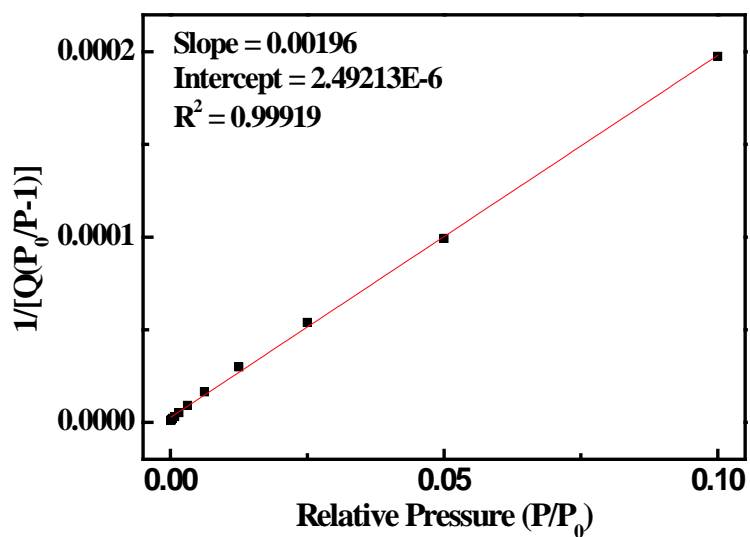


Figure 39. The plot of $P/P_0/(n(1-P/P_0))$ vs. P/P_0 to determine the BET surface area.

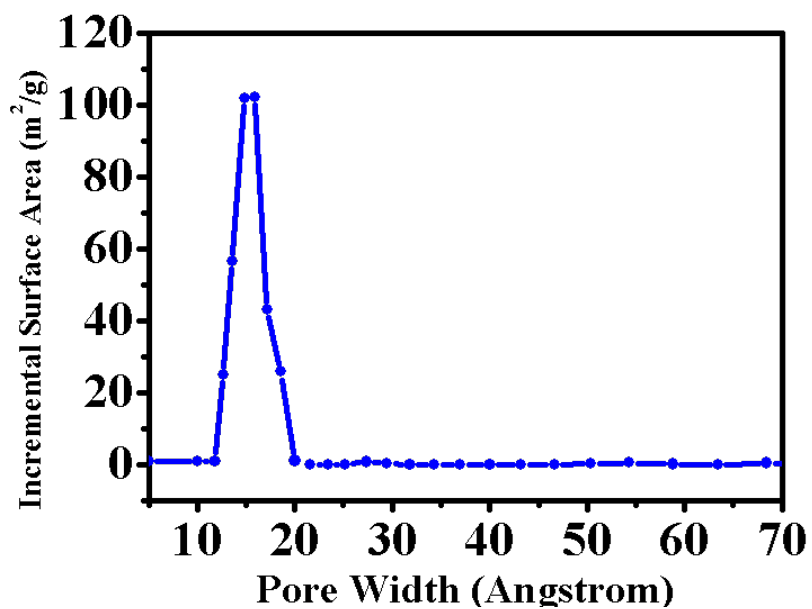


Figure 40. DFT pore size distribution of PCN-602(Ni) evaluated by using N₂ adsorption data measured at 77 K.

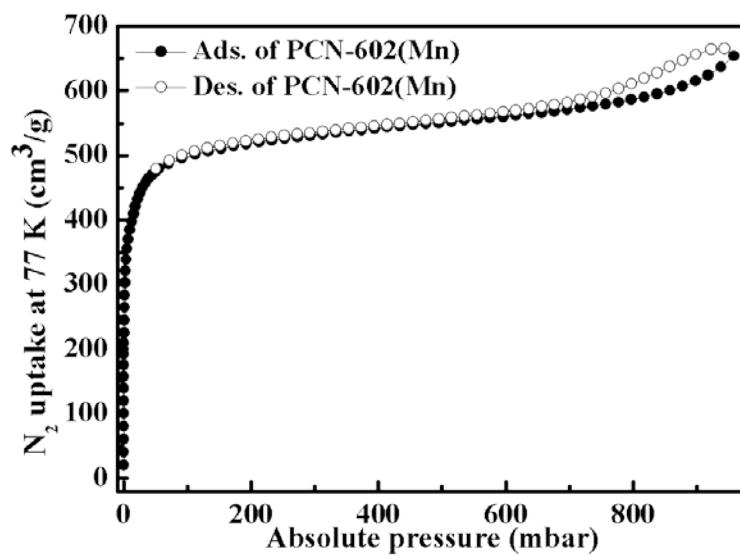


Figure 41. N₂ adsorption/desorption isotherm of PCN-602(Mn) at 77 K.

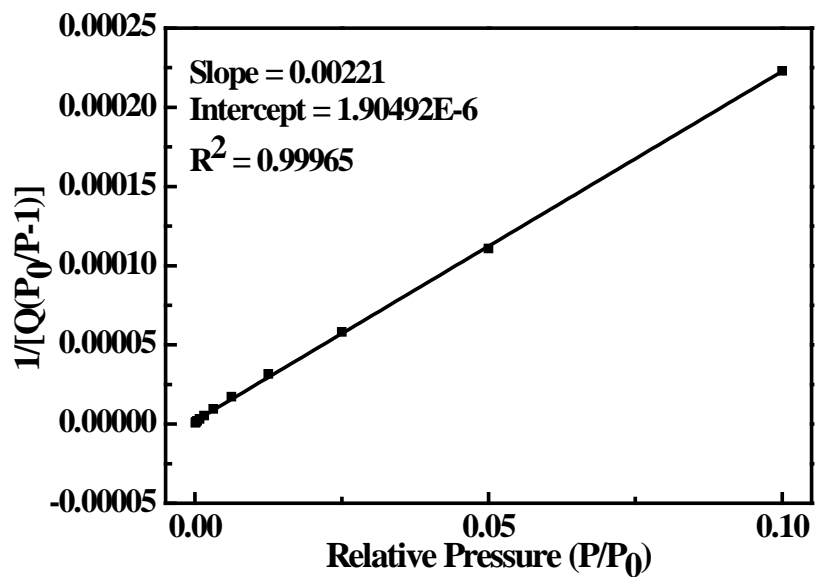


Figure 42. The plot of $P/P_0/(n(1-P/P_0))$ vs. P/P_0 to determine the BET surface area.

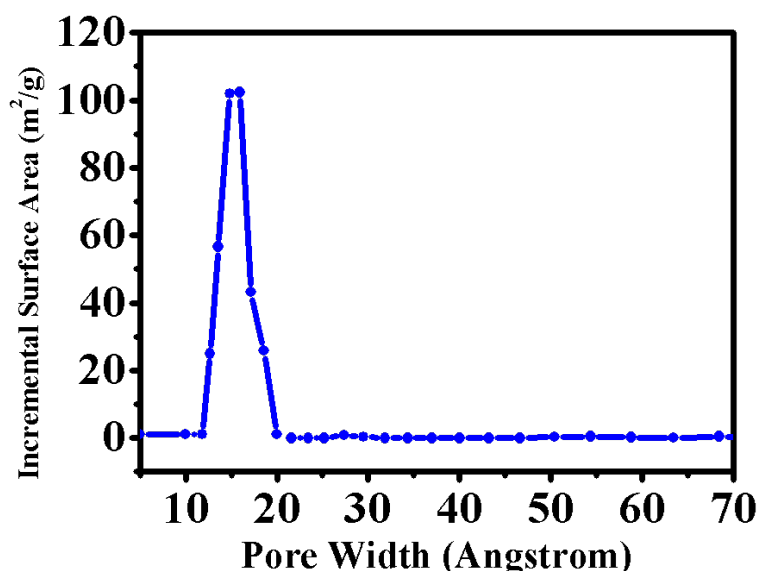


Figure 43. DFT pore size distribution of PCN-602(Mn) evaluated by using N₂ adsorption data measured at 77 K.

4.2.8 Rietveld Refinement and Crystallographic Data of PCN-602(Ni) *

The structure model of PCN-602(Ni) was refined by Rietveld refinement using Topas Academic version 4.1. The background was fitted with a 15th order Chebyshev polynomial. The refinement was conducted using a Pearson VII type peak profile function, followed by refinement of unit cells and zero-shift (Figure 44). Soft distance restraints were placed on the bonds between the nickel and oxygen atoms (2.20 Å), and the nickel and nitrogen atoms (2.10 Å). The rigid bodies were applied on ligands. The ligand was not fully occupied. The occupancy was refined to be 0.76. The additional oxygen atom (O2) with the occupancy of 0.24 was located near nickel atom (Ni1) with the Ni–O bond distance of 2.21 Å. The guest species in the cages of the structure could not be located owing to their partial occupancies and low symmetry. Instead, three

* The structural refinement of PCN-602 was conducted by Dr. Jie Su.

oxygen atoms were added at random positions inside the cages to compensate for the contributions of the guest species and refined subsequently. Crystallographic data and structural refinement are provided in Table 7.

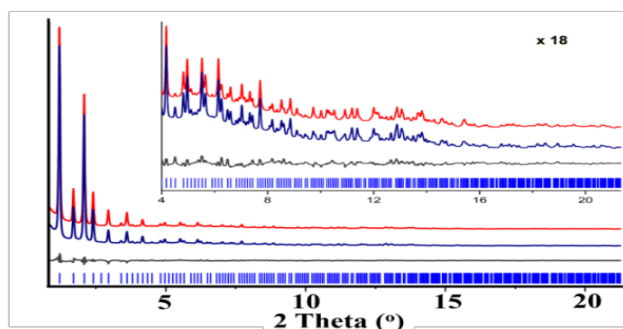


Figure 44. Rietveld refinement of powder X-ray diffraction data for PCN-602(Ni) (the curves from top to bottom are simulated (red), observed (blue), and difference profiles (gray), respectively; the bars below curves indicate peak positions).

Table 7. Crystallographic data and the Rietveld refinement result of PCN-602(Ni).

Chemical formula	$C_{127.92}H_{73.12}N_{27.44}Ni_{10.24}O_{21.98}$
Formula weight	2948.80
Crystal system	cubic
Space group	$Pm\bar{3}m$
$a / \text{\AA}$	21.559(2)
Z	1
Temperature / K	298(2)
Wavelength / \AA	0.45336
2θ range / $^\circ$	0.8~21.39
Number of reflections	686
Number of structural variables	49
R_p	0.03849
R_{wp}	0.04896
R_{exp}	0.00938
GOF	5.219

4.2.9 Chemical Stability Tests of PCN-602

PXRD measurements for stability test of PCN-602: After being washed with DMF and DI water, as-synthesized PCN-602 samples (10 mg for each batch) were immersed in about 3.5 mL aqueous solutions of 0.1 mM HCl (pH = 4), 1 M NaOH (pH = 14), 1 M KF, 1 M Na₂CO₃, and 1 M K₃PO₄ at room temperature for 24 h. The treated samples were collected and washed successively with deionized water (3 times) and acetone (3 times). The obtained powders were dried in an oven at 100 °C before PXRD measurements.

N₂ uptakes for stability test of PCN-602: Five batches of samples (about 100 mg for each) were immersed in 35 mL of 0.1 mM HCl (pH = 4), 1 M NaOH (pH = 14), 1 M KF, 1 M Na₂CO₃, and 1 M K₃PO₄ aqueous solutions at room temperature for 24 h, respectively. After being collected and washed with water (3 times) and acetone (3 times), the samples were activated under vacuum at 100 °C for 10 h on ASAP 2420 system. These activated samples were then measured for N₂ sorption at 77 K.

Electronic absorption Spectra for Stability Test of PCN-602(Mn): Five batches (about 10 mg of each sample) of different samples were immersed in 5 mL of 1 mM HCl (pH = 4), 1 M NaOH (pH = 14), 1 M KF, 1 M Na₂CO₃, and 1 M K₃PO₄ aqueous solutions for 24 h, respectively. After being washed with deionized water (3 times), the samples were soaked in DMF for 24 hours. The clear solutions were taken for electronic absorption spectrum measurements (Figure 49).

4.2.10 Catalytic Activity Tests of PCN-602(Mn)

The C–H bond halogenations reactions were conducted under two conditions. **Condition 1:** catalyst (13 mmol), NaClO (2 mL, 0.33 M in water), tetrabutylammonium chloride (TBACl, 8 mg, as the phase transfer catalyst (PTC)), the substrate (2 mmol), and dichloromethane (2 mL) were mixed and stirred under nitrogen at room temperature for 5 h. **Condition 2:** catalyst (13 mmol), NaClO (2 mL, 0.33 M in water), substrate (2 mmol), and acetone (2 mL) were mixed and stirred under nitrogen at room temperature for 2 h. After the completion of the reaction, the heterogeneous catalyst was collected by filtration. The homogeneous catalyst, inorganic salt and PTC in the filtrate were removed by a short silica gel column eluted by CH₂Cl₂. Then, the identities and the yields of the products were determined by GC-MS.

4.3 Results and Discussion

4.3.1 Chemical Stability of PCN-602

Chemical stability of PCN-602(M) (M = Mn²⁺, Ni²⁺) was firstly tested by treating its samples with the aqueous solutions of HCl and NaOH with pH = 4 and 14 for 24 h at room temperature, respectively. The PXRD patterns of the treated samples remained intact, indicating there was no phase transition or entire framework collapse of PCN-602 after the treatments (Figure 45 and 47). N₂ isotherms at 77 K of these treated samples further confirmed the robustness of PCN-602 in the acid and base solutions (Figure 46 and 48). Moreover, we also explored the stability of PCN-602 in 1 M KF, 1 M Na₂CO₃ and 1 M K₃PO₄ aqueous solutions, respectively. After soaking PCN-602 in these solutions for 24 h at RT, the PXRD patterns and N₂ isotherms of the treated

samples remained unchanged, demonstrating the excellent stability of PCN-602 in these solutions. For comparison, when PCN-224(Co), -222(Fe) and -600(Mn) were treated under the same conditions, the deep color of the solutions and the dissolution of the solid phases clearly indicated the severe decomposition of these MOFs (Figure 46 inset and Table 8). Considering F^- , CO_3^{2-} and PO_4^{3-} are all the conjugate bases of weak acids, the hydrolysis of these anions in aqueous solution will produce hydroxide anions, which are also destructive to the MOFs. To assess the effect of hydroxide anions in the decomposition of PCN-224(Co), -222(Fe) and -600(Mn), the pH values of 1 M KF, 1 M Na_2CO_3 and 1 M K_3PO_4 solutions were measured (Table 8). For instance, the pH value of 1 M KF solution was 7.79, while PCN-224(Co) -222(Fe) and -600(Mn) were claimed to be stable in NaOH aqueous solution with the pH value of 9.^{34, 50, 73} The complete dissolution of these three MOFs in 1 M KF aqueous solution should be attributed to attack of F^- anions. As revealed by the results above, when we evaluate the robustness of porphyrinic MOFs for the real applications, not only their stability in hydroxide solutions but also their resistance towards the attack of other coordinating anions should be carefully considered. However, the later requirement has been neglected for a long time, and can hardly be met by the previously reported porphyrinic MOFs.

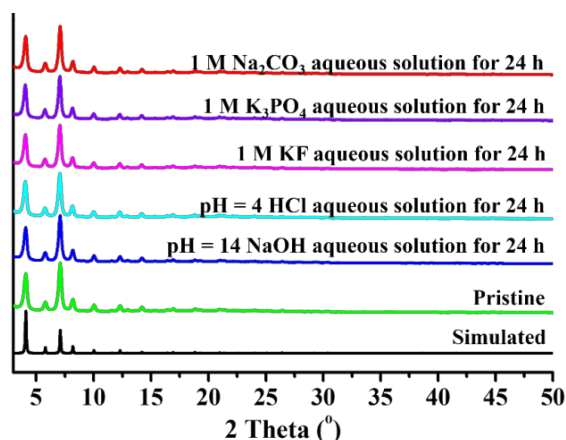


Figure 45. PXRD patterns simulated from the PCN-602 structural model, of pristine PCN-602(Ni) sample, and of those treated in different aqueous solutions.

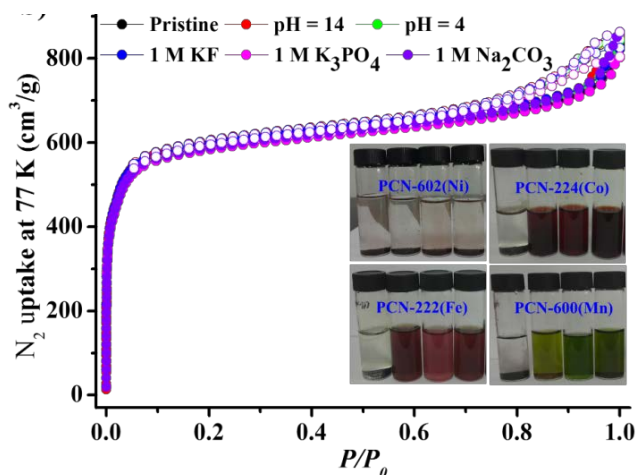


Figure 46. N₂ adsorption/desorption isotherms of pristine PCN-602(Ni) sample and of those treated in different aqueous solutions (inset: photographs of PCN-602(Ni), -224(Co), -222(Fe), and -600(Mn) soaked in different solutions for 24 h: deionized water, 1 M KF, 1 M Na₂CO₃, and 1 M K₃PO₄ aqueous solutions, from left to right).

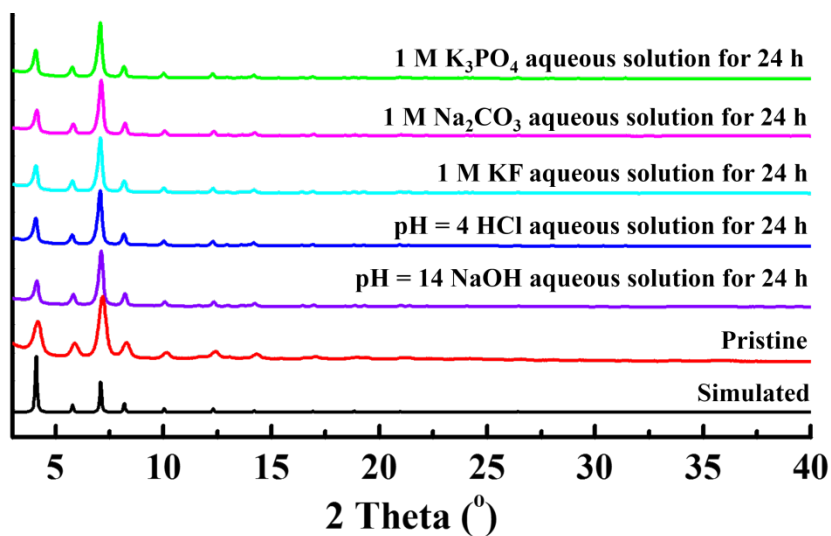


Figure 47. PXRD profiles of simulated, pristine PCN-602(Mn), and PCN-602(Mn) treated under different conditions.

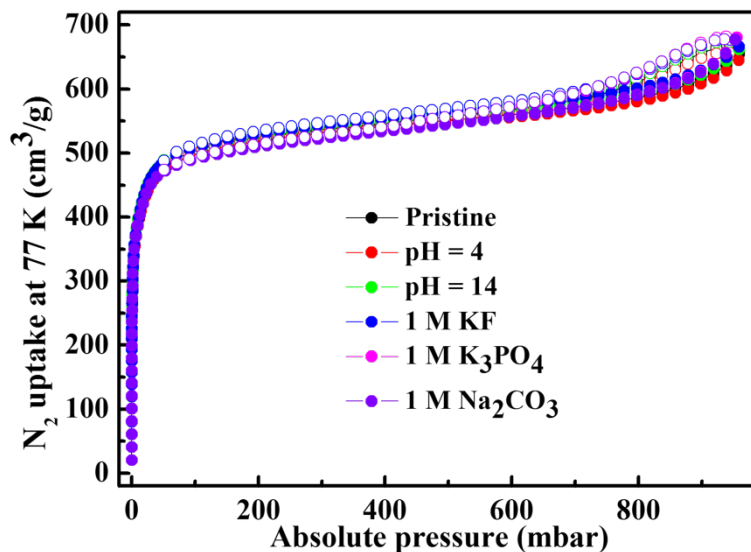


Figure 48. N₂ adsorption/desorption isotherms for simulated, pristine PCN-602(Mn), and PCN-602(Mn) samples treated under different conditions at 77 K.

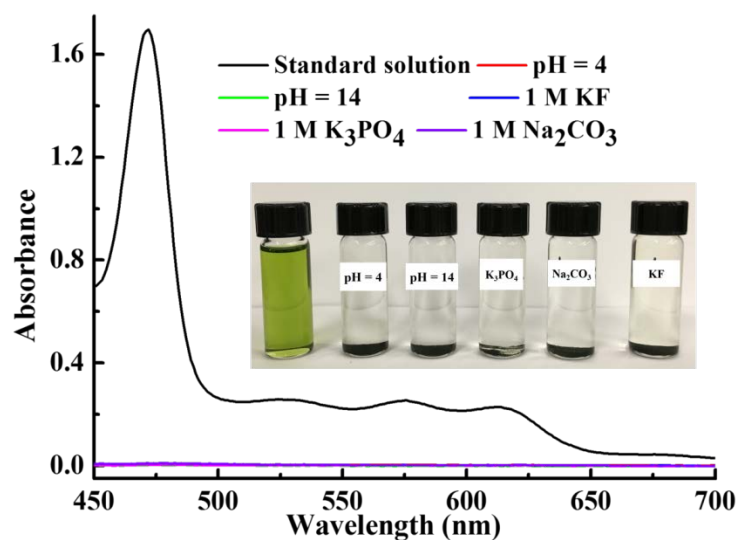


Figure 49. Electronic absorption spectrum of different solutions from the vials in inset (From left to right, Mn(H₄TPPP)Cl in DMF solution (0.1 mg / 4 mL), PCN-602(Mn) treated by pH = 4, pH =14, 1 M K₃PO₄, 1 M Na₂CO₃ and 1 M KF aqueous solution (these samples were washed with deionized water and soaked in DMF)).

Table 8. The state of different MOFs after treated under different conditions.

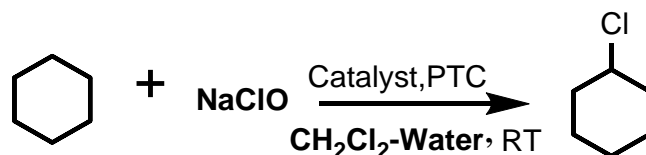
MOFs	Aqueous (pH = 7.0)	1 M KF aqueous solution (pH = 7.79)	1 M Na ₂ CO ₃ aqueous solution (pH =10.21)	1 M K ₃ PO ₄ aqueous solution (pH = 12.55)
PCN-602(Ni)	Powder	Powder	Powder	Powder
PCN-602(Mn)	Powder	Powder	Powder	Powder
PCN-222(Fe)	Powder	Red solution	Red solution	Red solution
PCN-224(Co)	Powder	Red solution	Red solution	Red solution
PCN-600(Mn)	Powder	Dark green solution	Dark green solution	Dark green solution

4.3.2 Catalytic Activity of PCN-602(Mn)

As we known, alkyl halides are widely applied in chemical industry and afford important components of a variety of biologically and pharmacologically active molecules.^{108, 109} Accordingly, the development of new synthesis approaches for alkyl halides is quite interesting but challenging, especially for the direct halogenation of inert C–H bonds. In 2010, Groves and his co-workers reported a method to directly halogenate alkylates with manganese porphyrin as the catalyst and hypohalite as the halogen source.^{107, 110} However, this method still suffered from the moderate yields and the usage of the homogeneous catalyst, which makes the recovery of the catalyst difficult. As we mentioned above, immobilizing porphyrin into MOFs could be an efficient method to improve the activity and recyclability of catalysts. Unfortunately, most of the reported porphyrinic MOFs cannot resist the attack of hydroxide and other coordinating anions in this reaction condition. As expected, the intergeneration of large porosity, the high concentration of catalytically active sites and extreme chemical stability in solutions of hydroxide and other coordinating anions makes PCN-602 a great candidate for the heterogeneous catalyst of this reaction.

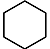
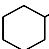
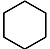
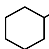
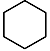
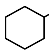
The chemical stabilities of PCN-602(Mn) in acidic, basic and coordinating anion containing aqueous solutions were also tested (Figure 47-49). The results demonstrated its stability is as high as that of PCN-602(Ni). Then, we applied PCN-602(Mn) as the catalyst in the halogenation reaction (Scheme 7). By following the reaction condition described in Groves' paper,¹⁰⁷ PCN-602(Mn) (5 mg), NaClO (2 mL, 0.33 M in water), TBACl (8 mg), cyclohexane (0.22 mL, 2 mmol), and dichloromethane (2 mL) were

mixed and stirred under nitrogen at room temperature for 5 h. The reaction process was monitored by evaluating the consumption of the oxidant (NaClO), through taking out 50 μL reaction solution from reaction system for electronic absorption test. The catalyst was removed by filtration and the filtrate went through a short silica gel column eluted by CH_2Cl_2 . Then, the solution was analyzed by GC-MS. Yields of chlorinated products were calculated based on oxidant added. The assignment of the products was based on the comparison of GC retention times and fragmentation with authentic samples and confirmed by MS (Figure 50-52). Catalytic performance of PCN-602(Mn), Mn(H_4TPPP)Cl, and Mn(TPP)Cl are listed in Table 9. A 92% yield of chlorocyclohexane was achieved. It is much higher than that reported in Groves' paper (57%) when homogeneous catalyst, Mn(TPP)Cl (herein, H_2TPP = *meso*-tetraphenylporphyrin) was applied.¹⁰⁷ The higher catalytic activity of PCN-602(Mn) could be explained by its rigid framework structure. When porphyrin catalysts are dissolved, the formation of catalytically inactive dimers is almost inevitable. As a comparison, the porphyrinic ligands are separated and anchored at the fixed positions in PCN-602(Mn), which makes every porphyrin center highly active.



Scheme 7. Chlorination of cyclohexane under the reported method.

Table 9. Catalytic performance of PCN-602(Mn), Mn(H₄TPPP)Cl, and Mn(TPP)Cl in the C–H bond chlorination under the reported conditions.

Entry	Substrate	Catalyst	Product	Yield (%)
1		PCN-602(Mn)		92
2		Mn(H ₄ TPPP)Cl		54
3		Mn(TPP)Cl		57

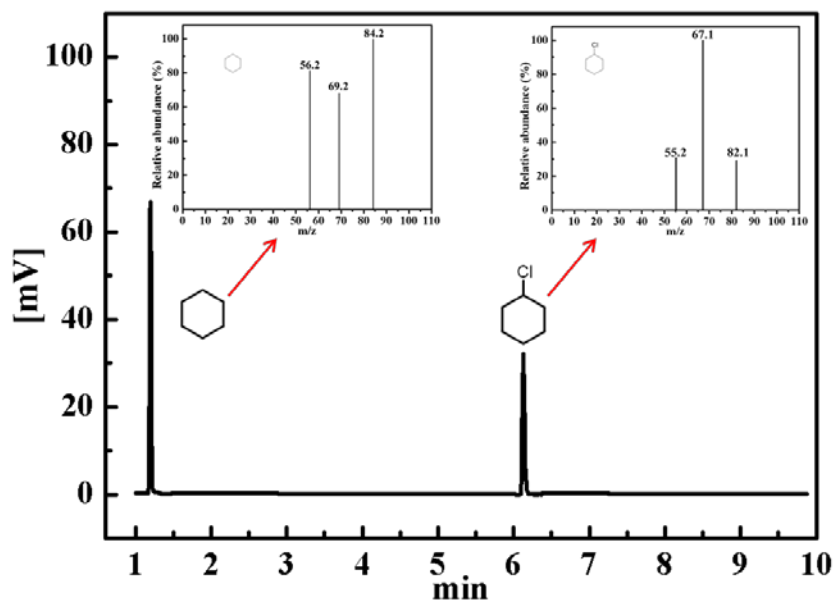


Figure 50. GC of the chlorination of cyclohexane catalyzed by PCN-602(Mn); inset shows the MS of cyclohexane and chlorocyclohexane.

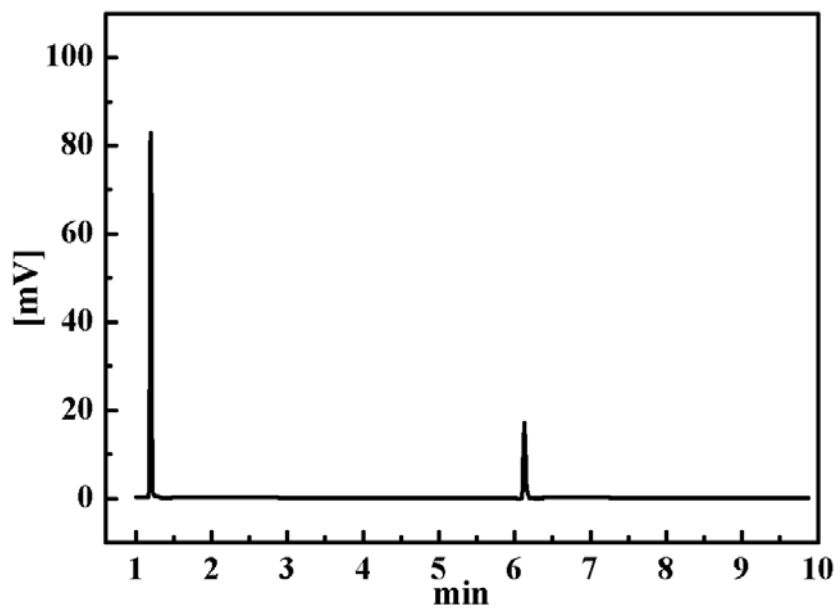


Figure 51. GC of the chlorination of cyclohexane catalyzed by Mn(H₄TPPP)Cl.

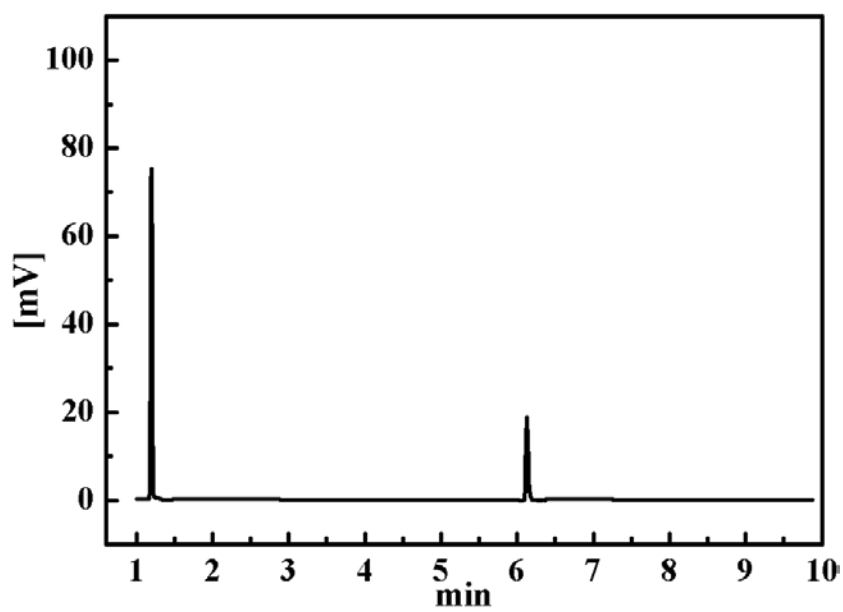
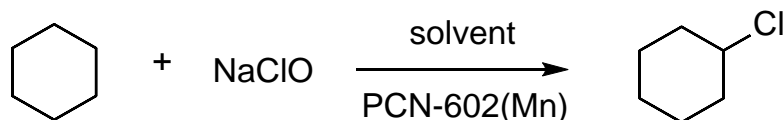


Figure 52. GC of the chlorination of cyclohexane catalyzed by Mn(TPP)Cl.

Moreover, with PCN-602(Mn) as the catalyst, further optimization could be done for this reaction. In the above-mentioned condition, two toxic species, dichloromethane and PTC, are applied to dissolve catalyst better and/or facilitate the migration of ClO^- from the aqueous phase to organic phase to react with the catalyst. However, the rigid structure and high porosity of PCN-602(Mn) can provide a high density of active sites that are approachable to the substrates, which makes the solubility of the catalyst and the phase transfer rate of ClO^- not the limiting factors anymore. This encouraged us to develop a reaction procedure with more environment-friendly solvent and no PTC (Scheme 8).



Scheme 8. Chlorination of cyclohexane in different solvents.

Table 10. Catalytic performance of PCN-602(Mn), $\text{Mn}(\text{H}_4\text{TPPP})\text{Cl}$, and $\text{Mn}(\text{TPP})\text{Cl}$ in different solvents for the C–H bond chlorination of cyclohexane.

Entry	solvent	Catalyst	Temperature ($^{\circ}\text{C}$)	Yield (%)
1	dichloromethane	$\text{Mn}(\text{H}_4\text{TPPP})\text{Cl}$	RT	5
2	dichloromethane	PCN-602(Mn)	RT	23
3	acetone	$\text{Mn}(\text{H}_4\text{TPPP})\text{Cl}$	RT	3
4	acetone	PCN-602(Mn)	RT	93

5	methanol	Mn(H ₄ TPPP)Cl	RT	4
6	methanol	PCN-602(Mn)	RT	80
7	ethanol	Mn(H ₄ TPPP)Cl	RT	5
8	ethanol	PCN-602(Mn)	RT	75
9	acetone	Mn(TPP)Cl	RT	8

In the absence of PTC, more environment-friendly compounds were screened as the organic solvent in this reaction. As described above, 2 mL of NaOCl (0.33 M in water) was added to a solution of porphyrin-based catalyst (5 mg) and cyclohexane (0.22 mL, 2 mmol) in 2 mL of solvent. As shown in Table 10, the catalysis proceeded with unsatisfactory yield (5% and 23%, respectively) when CH₂Cl₂ was used as the solvent. It can be explained by that the reactants were separated into two phases when dichloromethane was the organic solvent without PTC, which hinders the contact between substrate and oxidant. To solve this problem, methanol, ethanol, and acetone were applied as the organic solvents in this system, respectively (Figure 53-60, Table 10).

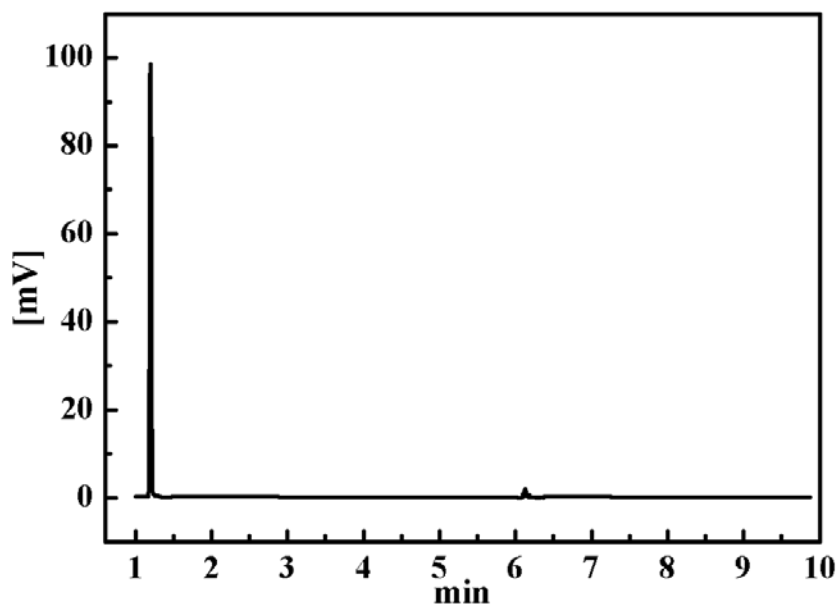


Figure 53. GC of the chlorination of cyclohexane catalyzed by Mn(TPP)Cl using CH_2Cl_2 as the solvent.

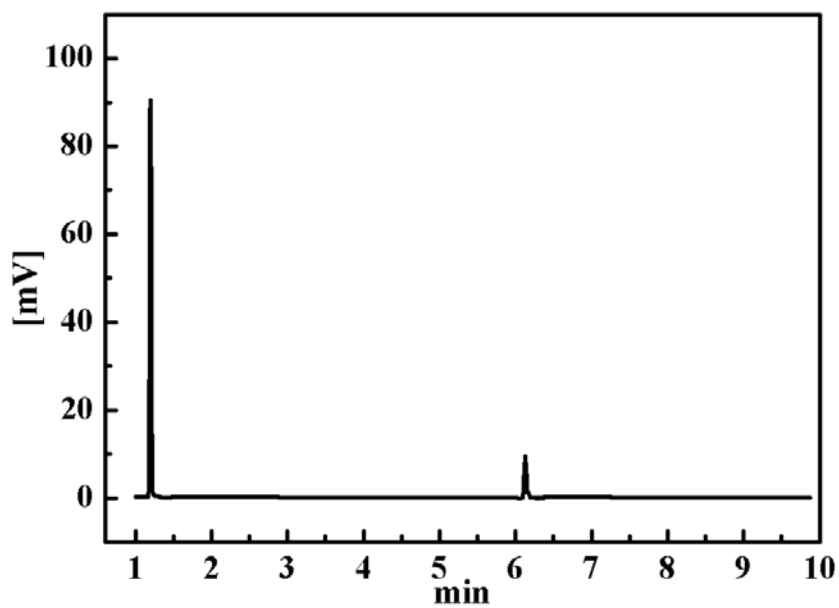


Figure 54. GC of the chlorination of cyclohexane catalyzed by PCN-602(Mn) using CH_2Cl_2 as the solvent.

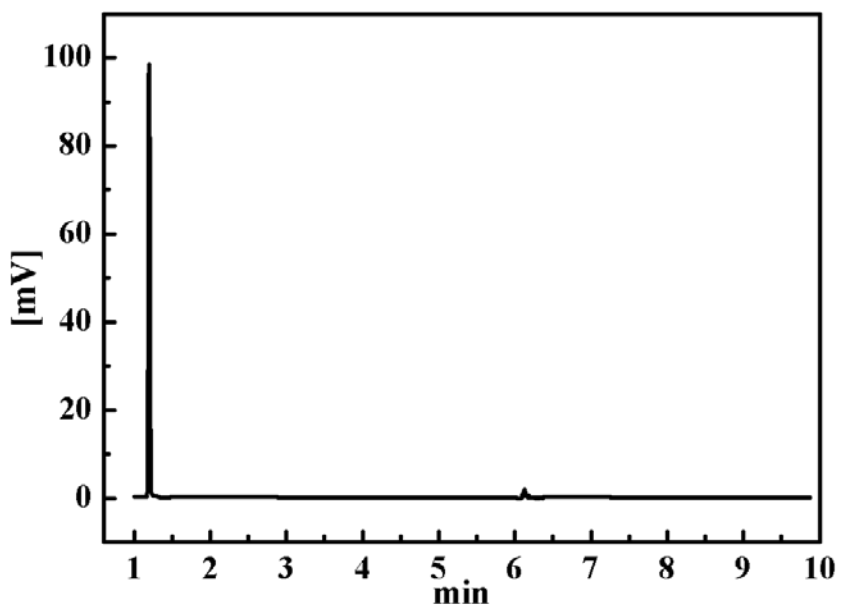


Figure 55. GC of the chlorination of cyclohexane catalyzed by $\text{Mn}(\text{H}_4\text{TPPP})\text{Cl}$ using acetone as the solvent.

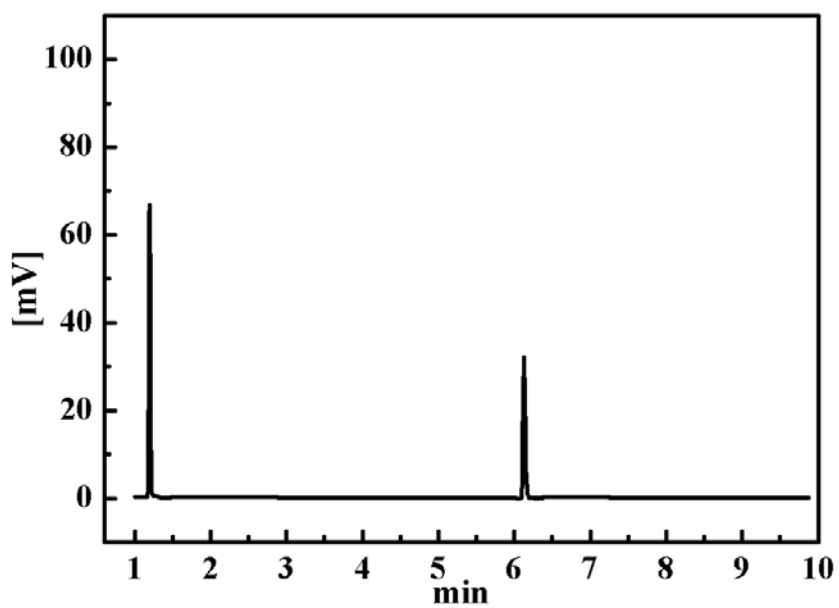


Figure 56. GC of the chlorination of cyclohexane catalyzed by PCN-602(Mn) using acetone as the solvent.

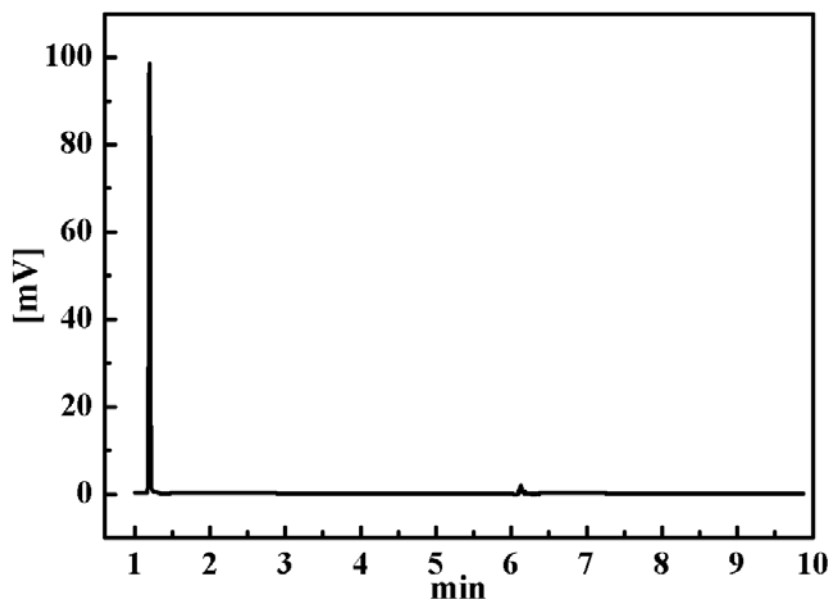


Figure 57. GC of the chlorination of cyclohexane catalyzed by Mn(TPP)Cl using methanol as the solvent.

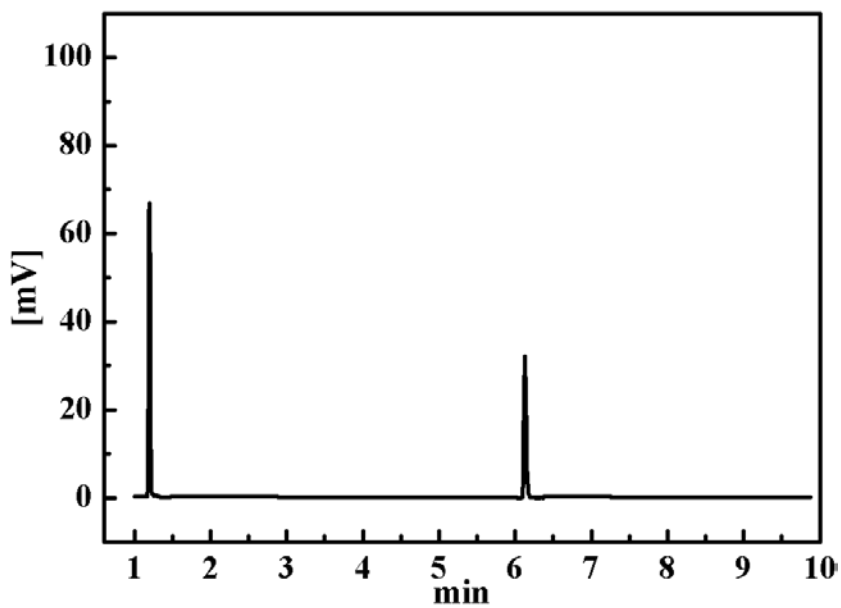


Figure 58. GC of the chlorination of cyclohexane catalyzed by PCN-602(Mn) using methanol as the solvent.

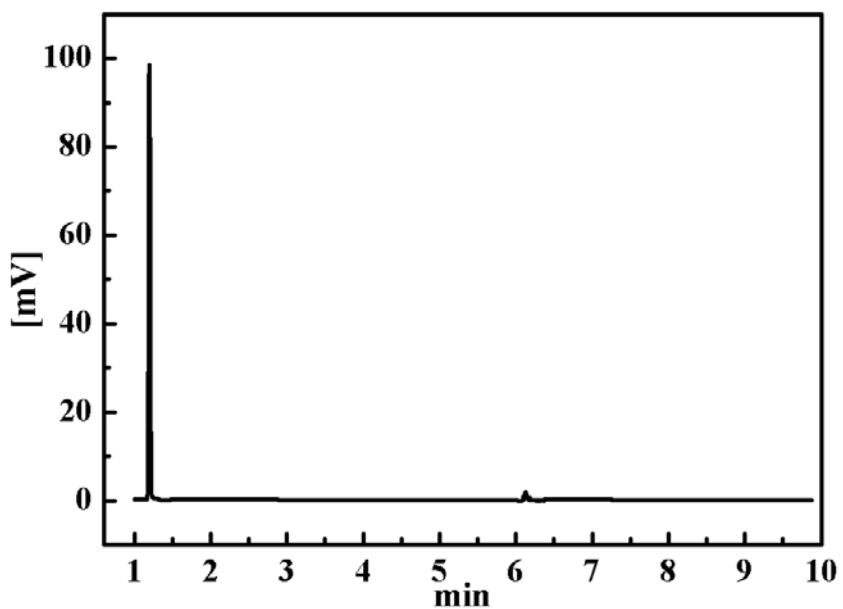


Figure 59. GC of the chlorination of cyclohexane catalyzed by Mn(H₄TPPP)Cl using ethanol as the solvent.

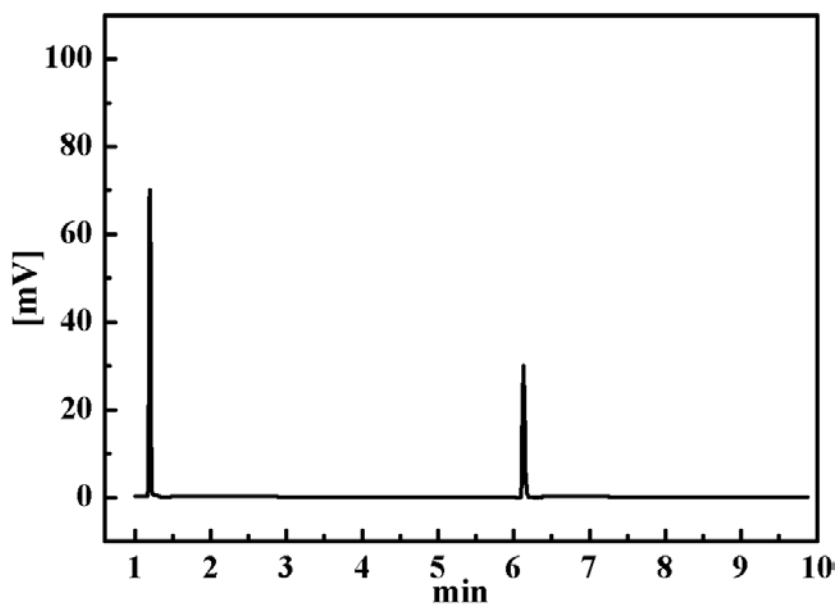
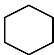
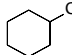
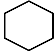
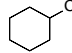
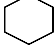
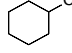


Figure 60. GC of the chlorination of cyclohexane catalyzed by PCN-602(Mn) using ethanol as the solvent.

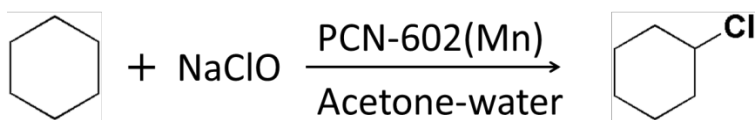
After systematic exploration, acetone was finally chosen as the best organic solvent (Scheme 9). The yield of the chlorocyclohexane reached 93% at room temperature in an even shorter reaction time (2 h) under this condition. As a comparison, when Mn(TPP)Cl was used as the catalyst under this condition, the product yield was only 8% (Figure 61a and Table 11). In addition, to evaluate the effect of the window size of the MOFs on the catalytic performance, PCN-601(Mn) was also prepared and applied as the catalyst in the cyclohexane chlorination under the same optimized condition. After an even longer reaction time of 10 h, the yield was only up to 15%. Clearly, the small window sizes of the cages in PCN-601(Mn) blocks the accesses of substrates to the active sites inside the framework, and thereby reduces its catalytic activity.

Table 11. The catalytic performance of PCN-602(Mn) and other selected catalysts in the C–H bond chlorination/bromination of cyclohexane/cyclopentane.^a

Entry	Substrate	Catalyst	Product	Yield(%)
1		PCN-602(Mn)		93 ^a
2		Mn(TPP)Cl		8 ^a
3		PCN-601(Mn)		15 ^b

^a Standard conditions: substrate/NaClO/catalyst = 2 : 0.66 : 0.013 mmol; in acetone-water (2 : 2 mL); and the suspension was stirred at room temperature for 2 h.

^b The reaction time is extended to 10 h.



Scheme 9. C–H bond halogenation catalyzed by PCN-602(Mn).

It should also be pointed out that the recyclability is another significant advantage of solid heterogeneous catalysts. To assess the performance of PCN-602(Mn) as a re-generable catalyst, the cycling experiment was conducted. After one run of reaction in acetone-water, the catalyst was collected by centrifugation and reused in the next run of reaction under the same condition. It was found that after three consecutive cycles, PCN-602(Mn) was still highly active with the reaction yield maintained up to 92% (Figure 61b). Moreover, the unchanged PXRD pattern and the N₂ sorption isotherm of PCN-602(Mn) in Figure 61c and 64d further confirmed its structural intactness after the cycling experiment.

Overall, the above results demonstrate that high-yield aliphatic halogenations can be achieved with PCN-602(Mn) as a regenerable heterogeneous catalyst under a more environment-friendly condition. This MOF catalyst significantly outperformed their homogeneous counterparts. To the best of our knowledge, this is the first example of the application of porphyrinic MOFs as a highly efficient catalyst in a harsh basic reaction condition.

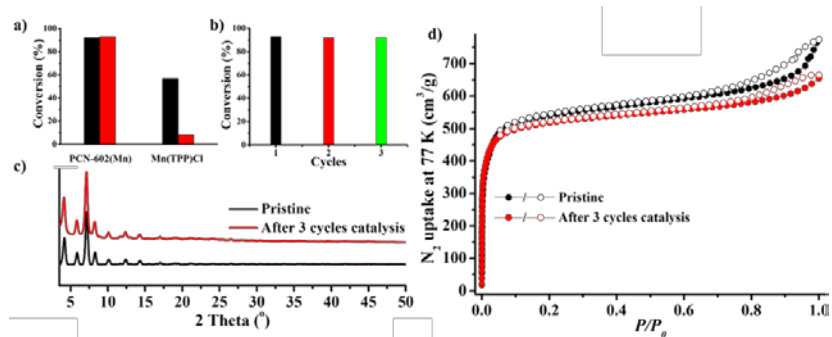


Figure 61. (a) Catalytic efficiencies of PCN-602(Mn) and Mn(TPP)Cl in the cyclohexane chlorination in the presence of PTC and CH₂Cl₂ (black) and under the optimal conditions in this work without PTC (red); (b) catalytic efficiencies of PCN-602(Mn) in three consecutive cyclic runs; and (c) PXRD patterns and (d) N₂ adsorption/desorption isotherms (at 77 K) of pristine PCN-602(Mn) and that after 3 catalytic cycles, respectively.

4.5 Conclusions

In conclusion, guided by the reticular synthesis strategy, a base-resistant pyrazolate-based porphyrinic MOF with high porosity and large window size, namely PCN-602, was constructed. It shows extraordinary robustness in basic solutions of several coordinating anions that are widely used in catalytic reactions. PCN-602(Mn), with Mn^{3+} -porphyrin centers, was confirmed to be a highly effective heterogeneous catalyst for the C–H halogenation of inert hydrocarbons under a basic condition. The base resistance of PCN-602 greatly broadens the application scope of MOFs as catalysts.

CHAPTER V

SUMMARY

Porphyrinic based MOFs, as a new kind of porous materials, have excellent potentials in various applications. However, their weak chemical stability severely hinders the utilization of these materials. In my research, we successfully developed several robust porphyrinic MOFs with excellent chemical stability to survive from different aqueous solutions, which greatly extended the application scope of MOFs.

Through rational topological design and KTDA method, PCN-600(Fe) was successfully synthesized. It showed high chemical stability in acid and base solutions with pH value from 2 to 11. Moreover, PCN-600(Fe) contains large 1D channel with a diameter of 3.1 nm, which can accelerate the diffusion of substrates when it is applied as catalysts. The activity of PCN-600(Fe) was confirmed by its performance as the catalysis of co-oxidation of phenol and 4-aminoantipyrine (4-AAP) by H₂O₂.

Most of the previously reported stable porphyrinic MOFs are constructed by high valent metal ions and carboxylate-based porphyrinic ligands. Though many of them exhibit excellent stability in acidic aqueous solutions, the robustness of these materials in base solutions is relatively much weaker. One method to overcome the vulnerability of MOFs in alkaline environments is to construct MOFs with azolate-based porphyrinic ligands. Guided by a top-down topological analysis, we rationally designed and synthesized PCN-601, which consists of [Ni₈] nodes and H₄TPP ligands. This material shows extraordinary stability in basic solutions. It can even survive in saturated NaOH solution (20 mol/L) at 100 °C, which almost pushes base-resistance of porphyrinic

MOFs to the limit in aqueous media. We also rationalized the thermodynamic and kinetic factors that contribute to the excellent stability of PCN-601.

Though PCN-601 exhibit outstanding chemical stability in alkaline solutions, the window size of the cages in its framework is too small ($\sim 2.1 \times 8.0 \text{ \AA}$). It severely slows down the diffusion of the substrate or even blocks the active centers when PCN-601 is applied as a catalyst. To solve this problem, we rationally elongated the ligand of PCN-601 and successfully obtained the MOFs with isostructural, namely PCN-602, which strikes the balance between porosity and robustness of the material. It not only shows good stability in NaOH solution, but also demonstrates its robustness in the solutions of several coordinating anions, including F^- , CO_3^{2-} , and PO_4^{3-} , which are widely used in many catalytic reactions. The high activity and outstanding recyclability of PCN-602 were confirmed by its excellent performance as a heterogeneous catalyst for the C–H halogenation of inert hydrocarbons under a basic condition, which significantly outperforms its homogeneous counterpart.

REFERENCES

- 1 H. C. Zhou and S. Kitagawa, Metal-organic frameworks (MOFs). *Chem Soc Rev*, 2014, **43**, 5415-5418.
- 2 H.-C. Zhou, J. R. Long and O. M. Yaghi, Introduction to Metal–Organic Frameworks. *Chemical Reviews*, 2012, **112**, 673-674.
- 3 M. Li, D. Li, M. O’Keeffe and O. M. Yaghi, Topological Analysis of Metal–Organic Frameworks with Polytopic Linkers and/or Multiple Building Units and the Minimal Transitivity Principle. *Chemical Reviews*, 2014, **114**, 1343-1370.
- 4 D. Farrusseng, S. Aguado and C. Pinel, Metal–Organic Frameworks: Opportunities for Catalysis. *Angewandte Chemie International Edition*, 2009, **48**, 7502-7513.
- 5 J. Liu, L. Chen, H. Cui, J. Zhang, L. Zhang and C.-Y. Su, Applications of metal-organic frameworks in heterogeneous supramolecular catalysis. *Chem Soc Rev*, 2014, **43**, 6011-6061.
- 6 Y. He, W. Zhou, G. Qian and B. Chen, Methane storage in metal-organic frameworks. *Chem Soc Rev*, 2014, **43**, 5657-5678.
- 7 K. Sumida, D. L. Rogow, J. A. Mason, T. M. McDonald, E. D. Bloch, Z. R. Herm, T.-H. Bae and J. R. Long, Carbon Dioxide Capture in Metal–Organic Frameworks. *Chemical Reviews*, 2012, **112**, 724-781.
- 8 Y. J. Colon and R. Q. Snurr, High-throughput computational screening of metal-organic frameworks. *Chem Soc Rev*, 2014, **43**, 5735-5749.

- 9 M. P. Suh, H. J. Park, T. K. Prasad and D.-W. Lim, Hydrogen Storage in Metal–Organic Frameworks. *Chemical Reviews*, 2012, **112**, 782-835.
- 10 A. Corma, H. García and F. X. Llabrés i Xamena, Engineering Metal Organic Frameworks for Heterogeneous Catalysis. *Chemical Reviews*, 2010, **110**, 4606-4655.
- 11 M. Yoon, R. Srirambalaji and K. Kim, Homochiral Metal–Organic Frameworks for Asymmetric Heterogeneous Catalysis. *Chemical Reviews*, 2012, **112**, 1196-1231.
- 12 H. Wu, Q. Gong, D. H. Olson and J. Li, Commensurate Adsorption of Hydrocarbons and Alcohols in Microporous Metal Organic Frameworks. *Chemical Reviews*, 2012, **112**, 836-868.
- 13 Y. Cui, Y. Yue, G. Qian and B. Chen, Luminescent Functional Metal–Organic Frameworks. *Chemical Reviews*, 2012, **112**, 1126-1162.
- 14 C. Wang, T. Zhang and W. Lin, Rational Synthesis of Noncentrosymmetric Metal–Organic Frameworks for Second-Order Nonlinear Optics. *Chemical Reviews*, 2012, **112**, 1084-1104.
- 15 T. Zhang and W. Lin, Metal-organic frameworks for artificial photosynthesis and photocatalysis. *Chem Soc Rev*, 2014, **43**, 5982-5993.
- 16 S. M. Cohen, Postsynthetic Methods for the Functionalization of Metal–Organic Frameworks. *Chemical Reviews*, 2012, **112**, 970-1000.

- 17 L. E. Kreno, K. Leong, O. K. Farha, M. Allendorf, R. P. Van Duyne and J. T. Hupp, Metal–Organic Framework Materials as Chemical Sensors. *Chemical Reviews*, 2012, **112**, 1105-1125.
- 18 Z.-Y. Gu, C.-X. Yang, N. Chang and X.-P. Yan, Metal–Organic Frameworks for Analytical Chemistry: From Sample Collection to Chromatographic Separation. *Accounts of Chemical Research*, 2012, **45**, 734-745.
- 19 J.-R. Li, J. Sculley and H.-C. Zhou, Metal–Organic Frameworks for Separations. *Chemical Reviews*, 2012, **112**, 869-932.
- 20 J. Canivet, A. Fateeva, Y. Guo, B. Coasne and D. Farrusseng, Water adsorption in MOFs: fundamentals and applications. *Chem Soc Rev*, 2014, **43**, 5594-5617.
- 21 A. J. Howarth, Y. Liu, P. Li, Z. Li, T. C. Wang, J. T. Hupp and O. K. Farha, Chemical, thermal and mechanical stabilities of metal–organic frameworks. *Nature Reviews Materials*, 2016, **1**, 15018.
- 22 G. Mouchaham, L. Cooper, N. Guillou, C. Martineau, E. Elkaïm, S. Bourrelly, P. L. Llewellyn, C. Allain, G. Clavier, C. Serre and T. Devic, A Robust Infinite Zirconium Phenolate Building Unit to Enhance the Chemical Stability of Zr MOFs. *Angewandte Chemie International Edition*, 2015, **54**, 13297-13301.
- 23 J. J. Low, A. I. Benin, P. Jakubczak, J. F. Abrahamian, S. A. Faheem and R. R. Willis, Virtual High Throughput Screening Confirmed Experimentally: Porous Coordination Polymer Hydration. *Journal of the American Chemical Society*, 2009, **131**, 15834-15842.

- 24 P.-C. Lo, X. Leng and D. K. P. Ng, Hetero-arrays of porphyrins and phthalocyanines. *Coordination Chemistry Reviews*, 2007, **251**, 2334-2353.
- 25 J. Park, D. Feng, S. Yuan and H.-C. Zhou, Photochromic Metal–Organic Frameworks: Reversible Control of Singlet Oxygen Generation. *Angewandte Chemie International Edition*, 2015, **54**, 430-435.
- 26 R. W.-Y. Sun, C. K.-L. Li, D.-L. Ma, J. J. Yan, C.-N. Lok, C.-H. Leung, N. Zhu and C.-M. Che, Stable Anticancer Gold(III)–Porphyrin Complexes: Effects of Porphyrin Structure. *Chemistry – A European Journal*, 2010, **16**, 3097-3113.
- 27 H. Eichhorn, Mesomorphic phthalocyanines, tetraazaporphyrins, porphyrins and triphenylenes as charge-transporting materials. *Journal of Porphyrins and Phthalocyanines*, 2000, **4**, 88-102.
- 28 H. Arthanari and P. H. Bolton, Functional and dysfunctional roles of quadruplex DNA in cells. *Chemistry & Biology*, 2001, **8**, 221-230.
- 29 H.-A. Wagenknecht, Helical Arrangement of Porphyrins along DNA: Towards Photoactive DNA-Based Nanoarchitectures. *Angewandte Chemie International Edition*, 2009, **48**, 2838-2841.
- 30 M. Maes, H. Sasabe, N. Kihara, Y. Araki, Y. Furusho, K. Mizuno, T. Takata and O. Ito, Photoinduced electron and energy transfer processes in rotaxanes containing zinc porphyrin as pendant and [60]fullerene and ferrocene as axle ends. *Journal of Porphyrins and Phthalocyanines*, 2005, **09**, 724-734.
- 31 G.-P. Yan, Z. Li, W. Xu, C.-K. Zhou, L. Yang, Q. Zhang, L. Li, F. Liu, L. Han, Y.-X. Ge and J.-F. Guo, Porphyrin-containing polyaspartamide gadolinium

- complexes as potential magnetic resonance imaging contrast agents. *International Journal of Pharmaceutics*, 2011, **407**, 119-125.
- 32 B. S. Lane and K. Burgess, Metal-Catalyzed Epoxidations of Alkenes with Hydrogen Peroxide. *Chemical Reviews*, 2003, **103**, 2457-2474.
- 33 P. Horcajada, R. Gref, T. Baati, P. K. Allan, G. Maurin, P. Couvreur, G. Férey, R. E. Morris and C. Serre, Metal–Organic Frameworks in Biomedicine. *Chemical Reviews*, 2012, **112**, 1232-1268.
- 34 D. Feng, Z.-Y. Gu, J.-R. Li, H.-L. Jiang, Z. Wei and H.-C. Zhou, Zirconium-Metalloporphyrin PCN-222: Mesoporous Metal–Organic Frameworks with Ultrahigh Stability as Biomimetic Catalysts. *Angewandte Chemie International Edition*, 2012, **51**, 10307-10310.
- 35 H.-L. Jiang, D. Feng, K. Wang, Z.-Y. Gu, Z. Wei, Y.-P. Chen and H.-C. Zhou, An Exceptionally Stable, Porphyrinic Zr Metal–Organic Framework Exhibiting pH-Dependent Fluorescence. *Journal of the American Chemical Society*, 2013, **135**, 13934-13938.
- 36 M. Zhao, S. Ou and C.-D. Wu, Porous Metal–Organic Frameworks for Heterogeneous Biomimetic Catalysis. *Accounts of Chemical Research*, 2014, **47**, 1199-1207.
- 37 J. Lee, O. K. Farha, J. Roberts, K. A. Scheidt, S. T. Nguyen and J. T. Hupp, Metal-organic framework materials as catalysts. *Chem Soc Rev*, 2009, **38**, 1450-1459.

- 38 M. H. Alkordi, Y. Liu, R. W. Larsen, J. F. Eubank and M. Eddaoudi, Zeolite-like Metal–Organic Frameworks as Platforms for Applications: On Metalloporphyrin-Based Catalysts. *Journal of the American Chemical Society*, 2008, **130**, 12639-12641.
- 39 P. Deria, D. A. Gómez-Gualdrón, W. Bury, H. T. Schaef, T. C. Wang, P. K. Thallapally, A. A. Sarjeant, R. Q. Snurr, J. T. Hupp and O. K. Farha, Ultraporous, Water Stable, and Breathing Zirconium-Based Metal–Organic Frameworks with ftw Topology. *Journal of the American Chemical Society*, 2015, **137**, 13183-13190.
- 40 W.-Y. Gao, M. Chrzanowski and S. Ma, Metal-metalloporphyrin frameworks: a resurging class of functional materials. *Chem Soc Rev*, 2014, **43**, 5841-5866.
- 41 S. Huh, S.-J. Kim and Y. Kim, Porphyrinic metal-organic frameworks from custom-designed porphyrins. *CrystEngComm*, 2016, **18**, 345-368.
- 42 J. A. Johnson, X. Zhang, T. C. Reeson, Y.-S. Chen and J. Zhang, Facile Control of the Charge Density and Photocatalytic Activity of an Anionic Indium Porphyrin Framework via in Situ Metalation. *Journal of the American Chemical Society*, 2014, **136**, 15881-15884.
- 43 L. Meng, Q. Cheng, C. Kim, W.-Y. Gao, L. Wojtas, Y.-S. Chen, M. J. Zaworotko, X. P. Zhang and S. Ma, Crystal Engineering of a Microporous, Catalytically Active fcu Topology MOF Using a Custom-Designed Metalloporphyrin Linker. *Angewandte Chemie International Edition*, 2012, **51**, 10082-10085.

- 44 W. Morris, B. Voloskiy, S. Demir, F. Gándara, P. L. McGrier, H. Furukawa, D. Cascio, J. F. Stoddart and O. M. Yaghi, Synthesis, Structure, and Metalation of Two New Highly Porous Zirconium Metal–Organic Frameworks. *Inorganic Chemistry*, 2012, **51**, 6443-6445.
- 45 H.-J. Son, S. Jin, S. Patwardhan, S. J. Wezenberg, N. C. Jeong, M. So, C. E. Wilmer, A. A. Sarjeant, G. C. Schatz, R. Q. Snurr, O. K. Farha, G. P. Wiederrecht and J. T. Hupp, Light-Harvesting and Ultrafast Energy Migration in Porphyrin-Based Metal–Organic Frameworks. *Journal of the American Chemical Society*, 2013, **135**, 862-869.
- 46 K. S. Suslick, P. Bhyrappa, J. H. Chou, M. E. Kosal, S. Nakagaki, D. W. Smithenry and S. R. Wilson, Microporous Porphyrin Solids. *Accounts of Chemical Research*, 2005, **38**, 283-291.
- 47 X.-S. Wang, M. Chrzanowski, L. Wojtas, Y.-S. Chen and S. Ma, Formation of a Metalloporphyrin-Based Nanoreactor by Postsynthetic Metal–Ion Exchange of a Polyhedral-Cage Containing a Metal–Metalloporphyrin Framework. *Chemistry – A European Journal*, 2013, **19**, 3297-3301.
- 48 X.-L. Yang, M.-H. Xie, C. Zou, Y. He, B. Chen, M. O’Keeffe and C.-D. Wu, Porous Metalloporphyrinic Frameworks Constructed from Metal 5,10,15,20-Tetrakis(3,5-biscarboxylphenyl)porphyrin for Highly Efficient and Selective Catalytic Oxidation of Alkylbenzenes. *Journal of the American Chemical Society*, 2012, **134**, 10638-10645.

- 49 Z. Zhang, L. Zhang, L. Wojtas, M. Eddaoudi and M. J. Zaworotko, Template-Directed Synthesis of Nets Based upon Octahemioctahedral Cages That Encapsulate Catalytically Active Metalloporphyrins. *Journal of the American Chemical Society*, 2012, **134**, 928-933.
- 50 D. Feng, W.-C. Chung, Z. Wei, Z.-Y. Gu, H.-L. Jiang, Y.-P. Chen, D. J. Darensbourg and H.-C. Zhou, Construction of Ultrastable Porphyrin Zr Metal–Organic Frameworks through Linker Elimination. *Journal of the American Chemical Society*, 2013, **135**, 17105-17110.
- 51 T.-F. Liu, D. Feng, Y.-P. Chen, L. Zou, M. Bosch, S. Yuan, Z. Wei, S. Fordham, K. Wang and H.-C. Zhou, Topology-Guided Design and Syntheses of Highly Stable Mesoporous Porphyrinic Zirconium Metal–Organic Frameworks with High Surface Area. *Journal of the American Chemical Society*, 2015, **137**, 413-419.
- 52 Q. Lin, X. Bu, A. Kong, C. Mao, X. Zhao, F. Bu and P. Feng, New Heterometallic Zirconium Metalloporphyrin Frameworks and Their Heteroatom-Activated High-Surface-Area Carbon Derivatives. *Journal of the American Chemical Society*, 2015, **137**, 2235-2238.
- 53 J. S. Anderson, A. T. Gallagher, J. A. Mason and T. D. Harris, A Five-Coordinate Heme Dioxygen Adduct Isolated within a Metal–Organic Framework. *Journal of the American Chemical Society*, 2014, **136**, 16489-16492.
- 54 C. Y. Lee, O. K. Farha, B. J. Hong, A. A. Sarjeant, S. T. Nguyen and J. T. Hupp, Light-Harvesting Metal–Organic Frameworks (MOFs): Efficient Strut-to-Strut

- Energy Transfer in Bodipy and Porphyrin-Based MOFs. *Journal of the American Chemical Society*, 2011, **133**, 15858-15861.
- 55 Y. Liu, A. J. Howarth, J. T. Hupp and O. K. Farha, Selective Photooxidation of a Mustard-Gas Simulant Catalyzed by a Porphyrinic Metal–Organic Framework. *Angewandte Chemie International Edition*, 2015, **54**, 9001-9005.
- 56 K. Lu, C. He and W. Lin, Nanoscale Metal–Organic Framework for Highly Effective Photodynamic Therapy of Resistant Head and Neck Cancer. *Journal of the American Chemical Society*, 2014, **136**, 16712-16715.
- 57 A. Fateeva, P. A. Chater, C. P. Ireland, A. A. Tahir, Y. Z. Khimyak, P. V. Wiper, J. R. Darwent and M. J. Rosseinsky, A Water-Stable Porphyrin-Based Metal–Organic Framework Active for Visible-Light Photocatalysis. *Angewandte Chemie International Edition*, 2012, **51**, 7440-7444.
- 58 J. Zheng, M. Wu, F. Jiang, W. Su and M. Hong, Stable porphyrin Zr and Hf metal-organic frameworks featuring 2.5 nm cages: high surface areas, SCSC transformations and catalyses. *Chemical Science*, 2015, **6**, 3466-3470.
- 59 A. Umemura, S. Diring, S. Furukawa, H. Uehara, T. Tsuruoka and S. Kitagawa, Morphology Design of Porous Coordination Polymer Crystals by Coordination Modulation. *Journal of the American Chemical Society*, 2011, **133**, 15506-15513.
- 60 J.-H. Wang, Y. Zhang, M. Li, S. Yan, D. Li and X.-M. Zhang, Solvent-Assisted Metal Metathesis: A Highly Efficient and Versatile Route towards Synthetically

- Demanding Chromium Metal–Organic Frameworks. *Angewandte Chemie*, 2017, n/a-n/a.
- 61 D. Feng, K. Wang, Z. Wei, Y.-P. Chen, C. M. Simon, R. K. Arvapally, R. L. Martin, M. Bosch, T.-F. Liu, S. Fordham, D. Yuan, M. A. Omary, M. Haranczyk, B. Smit and H.-C. Zhou, Kinetically tuned dimensional augmentation as a versatile synthetic route towards robust metal–organic frameworks. *Nature Communications*, 2014, **5**, 5723.
- 62 R. W. Noble and Q. H. Gibson, The reaction of ferrous horseradish peroxidase with hydrogen peroxide. *J Biol Chem*, 1970, **245**, 2409-2413.
- 63 I. Accelrys Software, *Journal*, 2010.
- 64 L. Ma, C. Abney and W. Lin, Enantioselective catalysis with homochiral metal-organic frameworks. *Chem Soc Rev*, 2009, **38**, 1248-1256.
- 65 D. Fiedler, D. H. Leung, R. G. Bergman and K. N. Raymond, Selective Molecular Recognition, C–H Bond Activation, and Catalysis in Nanoscale Reaction Vessels. *Accounts of Chemical Research*, 2005, **38**, 349-358.
- 66 M. E. Padilla-Tosta, O. D. Fox, M. G. B. Drew and P. D. Beer, Self-Assembly of a Mixed-Valence Copper(II)/Copper(III) Dithiocarbamate Catenane. *Angewandte Chemie International Edition*, 2001, **40**, 4235-4239.
- 67 M. Karlsson, M. Davidson, R. Karlsson, A. Karlsson, J. Bergenholtz, Z. Konkoli, A. Jesorka, T. Lobovkina, J. Hurtig, M. Voinova and O. Orwar, Biomimetic nanoscale reactors and networks. *Annu Rev Phys Chem*, 2004, **55**, 613-649.

- 68 S. Biswas, T. Ahnfeldt and N. Stock, New Functionalized Flexible Al-MIL-53-X (X = -Cl, -Br, -CH₃, -NO₂, -(OH)₂) Solids: Syntheses, Characterization, Sorption, and Breathing Behavior. *Inorganic Chemistry*, 2011, **50**, 9518-9526.
- 69 P. L. Llewellyn, S. Bourrelly, C. Serre, A. Vimont, M. Daturi, L. Hamon, G. De Weireld, J.-S. Chang, D.-Y. Hong, Y. Kyu Hwang, S. Hwa Jung and G. Férey, High Uptakes of CO₂ and CH₄ in Mesoporous Metal—Organic Frameworks MIL-100 and MIL-101. *Langmuir*, 2008, **24**, 7245-7250.
- 70 G. Férey, C. Mellot-Draznieks, C. Serre, F. Millange, J. Dutour, S. Surblé and I. Margiolaki, A Chromium Terephthalate-Based Solid with Unusually Large Pore Volumes and Surface Area. *Science*, 2005, **309**, 2040-2042.
- 71 X. Zhu, J. Gu, Y. Wang, B. Li, Y. Li, W. Zhao and J. Shi, Inherent anchorages in UiO-66 nanoparticles for efficient capture of alendronate and its mediated release. *Chemical Communications*, 2014, **50**, 8779-8782.
- 72 N. L. Torad, M. Hu, Y. Kamachi, K. Takai, M. Imura, M. Naito and Y. Yamauchi, Facile synthesis of nanoporous carbons with controlled particle sizes by direct carbonization of monodispersed ZIF-8 crystals. *Chemical Communications*, 2013, **49**, 2521-2523.
- 73 K. Wang, D. Feng, T.-F. Liu, J. Su, S. Yuan, Y.-P. Chen, M. Bosch, X. Zou and H.-C. Zhou, A Series of Highly Stable Mesoporous Metalloporphyrin Fe-MOFs. *Journal of the American Chemical Society*, 2014, **136**, 13983-13986.
- 74 J. H. Cavka, S. Jakobsen, U. Olsbye, N. Guillou, C. Lamberti, S. Bordiga and K. P. Lillerud, A New Zirconium Inorganic Building Brick Forming Metal Organic

- Frameworks with Exceptional Stability. *Journal of the American Chemical Society*, 2008, **130**, 13850-13851.
- 75 M. Carboni, C. W. Abney, S. Liu and W. Lin, Highly porous and stable metal-organic frameworks for uranium extraction. *Chemical Science*, 2013, **4**, 2396-2402.
- 76 H. Fei and S. M. Cohen, A robust, catalytic metal-organic framework with open 2,2[prime or minute]-bipyridine sites. *Chemical Communications*, 2014, **50**, 4810-4812.
- 77 O. V. Gutov, W. Bury, D. A. Gomez-Gualdron, V. Krungleviciute, D. Fairen-Jimenez, J. E. Mondloch, A. A. Sarjeant, S. S. Al-Juaid, R. Q. Snurr, J. T. Hupp, T. Yildirim and O. K. Farha, Water-Stable Zirconium-Based Metal–Organic Framework Material with High-Surface Area and Gas-Storage Capacities. *Chemistry – A European Journal*, 2014, **20**, 12389-12393.
- 78 M. Kim and S. M. Cohen, Discovery, development, and functionalization of Zr(IV)-based metal-organic frameworks. *CrystEngComm*, 2012, **14**, 4096-4104.
- 79 S. Biswas, M. Grzywa, H. P. Nayek, S. Dehnen, I. Senkowska, S. Kaskel and D. Volkmer, A cubic coordination framework constructed from benzobistriazolate ligands and zinc ions having selective gas sorption properties. *Dalton Transactions*, 2009, 6487-6495.
- 80 W.-Y. Gao, R. Cai, L. Meng, L. Wojtas, W. Zhou, T. Yildirim, X. Shi and S. Ma, Quest for a highly connected robust porous metal-organic framework on the basis

- of a bifunctional linear linker and a rare heptanuclear zinc cluster. *Chemical Communications*, 2013, **49**, 10516-10518.
- 81 Z. R. Herm, B. M. Wiers, J. A. Mason, J. M. van Baten, M. R. Hudson, P. Zajdel, C. M. Brown, N. Masciocchi, R. Krishna and J. R. Long, Separation of Hexane Isomers in a Metal-Organic Framework with Triangular Channels. *Science*, 2013, **340**, 960-964.
- 82 D.-X. Xue, A. J. Cairns, Y. Belmabkhout, L. Wojtas, Y. Liu, M. H. Alkordi and M. Eddaoudi, Tunable Rare-Earth fcu-MOFs: A Platform for Systematic Enhancement of CO₂ Adsorption Energetics and Uptake. *Journal of the American Chemical Society*, 2013, **135**, 7660-7667.
- 83 J.-P. Zhang, Y.-B. Zhang, J.-B. Lin and X.-M. Chen, Metal Azolate Frameworks: From Crystal Engineering to Functional Materials. *Chemical Reviews*, 2012, **112**, 1001-1033.
- 84 T. M. McDonald, D. M. D'Alessandro, R. Krishna and J. R. Long, Enhanced carbon dioxide capture upon incorporation of N,N[prime or minute]-dimethylethylenediamine in the metal-organic framework CuBTri. *Chemical Science*, 2011, **2**, 2022-2028.
- 85 V. Colombo, S. Galli, H. J. Choi, G. D. Han, A. Maspero, G. Palmisano, N. Masciocchi and J. R. Long, High thermal and chemical stability in pyrazolate-bridged metal-organic frameworks with exposed metal sites. *Chemical Science*, 2011, **2**, 1311-1319.

- 86 K. S. Park, Z. Ni, A. P. Côté, J. Y. Choi, R. Huang, F. J. Uribe-Romo, H. K. Chae, M. O’Keeffe and O. M. Yaghi, Exceptional chemical and thermal stability of zeolitic imidazolate frameworks. *Proceedings of the National Academy of Sciences*, 2006, **103**, 10186-10191.
- 87 G. Zoppellaro, V. Enkelmann, A. Geies and M. Baumgarten, A Multifunctional High-Spin Biradical Pyrazolylbipyridine-bisnitronylnitroxide. *Organic Letters*, 2004, **6**, 4929-4932.
- 88 N. M. Padial, E. Quartapelle Procopio, C. Montoro, E. López, J. E. Oltra, V. Colombo, A. Maspero, N. Masciocchi, S. Galli, I. Senkovska, S. Kaskel, E. Barea and J. A. R. Navarro, Highly Hydrophobic Isoreticular Porous Metal–Organic Frameworks for the Capture of Harmful Volatile Organic Compounds. *Angewandte Chemie International Edition*, 2013, **52**, 8290-8294.
- 89 P.-E. Werner, L. Eriksson and M. Westdahl, TREOR, a semi-exhaustive trial-and-error powder indexing program for all symmetries. *Journal of Applied Crystallography*, 1985, **18**, 367-370.
- 90 V. Petříček, M. Dušek and L. Palatinus, Crystallographic Computing System JANA2006: General features. *Zeitschrift für Kristallographie - Crystalline Materials*, 2014, **229**.
- 91 L. Palatinus and G. Chapuis, SUPERFLIP - a computer program for the solution of crystal structures by charge flipping in arbitrary dimensions. *Journal of Applied Crystallography*, 2007, **40**, 786-790.

- 92 K. I. Pandya, In Situ X-Ray Absorption Spectroscopic Studies of Nickel Oxide Electrodes. *Journal of The Electrochemical Society*, 1990, **137**, 383.
- 93 N. Masciocchi, S. Galli, V. Colombo, A. Maspero, G. Palmisano, B. Seyyedi, C. Lamberti and S. Bordiga, Cubic Octanuclear Ni(II) Clusters in Highly Porous Polypyrazolyl-Based Materials. *Journal of the American Chemical Society*, 2010, **132**, 7902-7904.
- 94 O. Delgado-Friedrichs, M. O'Keeffe and O. M. Yaghi, Three-periodic nets and tilings: edge-transitive binodal structures. *Acta Crystallographica Section A*, 2006, **62**, 350-355.
- 95 J.-Y. Xu, X. Qiao, H.-B. Song, S.-P. Yan, D.-Z. Liao, S. Gao, Y. Journaux and J. Cano, The self-assembly and magnetic properties of a Ni(ii)₈([small micro]4-hydroxo)₆ cube with [small micro]2-pyrazolate as an exogeneous ancillary ligand. *Chemical Communications*, 2008, 6414-6416.
- 96 M. Tonigold, Y. Lu, A. Mavrandonakis, A. Puls, R. Staudt, J. Möllmer, J. Sauer and D. Volkmer, Pyrazolate-Based Cobalt(II)-Containing Metal–Organic Frameworks in Heterogeneous Catalytic Oxidation Reactions: Elucidating the Role of Entatic States for Biomimetic Oxidation Processes. *Chemistry – A European Journal*, 2011, **17**, 8671-8695.
- 97 O. Delgado-Friedrichs and M. O'Keeffe, Three-periodic tilings and nets: face-transitive tilings and edge-transitive nets revisited. *Acta Crystallographica Section A*, 2007, **63**, 344-347.

- 98 D. Feng, H.-L. Jiang, Y.-P. Chen, Z.-Y. Gu, Z. Wei and H.-C. Zhou, Metal–Organic Frameworks Based on Previously Unknown Zr₈/Hf₈ Cubic Clusters. *Inorganic Chemistry*, 2013, **52**, 12661-12667.
- 99 J. Reedijk, Complexes with ligands containing nitrile groups. Part IX . Magnetic measurements on solid methyl-cyanide solvates. *Recueil des Travaux Chimiques des Pays-Bas*, 1969, **88**, 86-96.
- 100 S. Soyama, M. Ishii, S. Funahashi and M. Tanaka, Variable-temperature and -pressure multinuclear magnetic resonance study of solvent exchange at the tris(ethylenediamine)nickel(II) ion in ethylenediamine. *Inorganic Chemistry*, 1992, **31**, 536-538.
- 101 J. B. DeCoste, G. W. Peterson, H. Jasuja, T. G. Glover, Y.-g. Huang and K. S. Walton, Stability and degradation mechanisms of metal-organic frameworks containing the Zr₆O₄(OH)₄ secondary building unit. *Journal of Materials Chemistry A*, 2013, **1**, 5642-5650.
- 102 K. Wang, X.-L. Lv, D. Feng, J. Li, S. Chen, J. Sun, L. Song, Y. Xie, J.-R. Li and H.-C. Zhou, Pyrazolate-Based Porphyrinic Metal–Organic Framework with Extraordinary Base-Resistance. *Journal of the American Chemical Society*, 2016, **138**, 914-919.
- 103 S. E. Denmark and G. L. Beutner, Lewis Base Catalysis in Organic Synthesis. *Angewandte Chemie International Edition*, 2008, **47**, 1560-1638.
- 104 D. R. Lide, *CRC Handbook of Chemistry and Physics*, CRC Press 82nd edn., 2001.

- 105 J. Speight, *Lang's Handbook of Chemistry*, 16th edn., 2005.
- 106 O. M. Yaghi, M. O'Keeffe, N. W. Ockwig, H. K. Chae, M. Eddaoudi and J. Kim, Reticular synthesis and the design of new materials. *Nature*, 2003, **423**, 705-714.
- 107 W. Liu and J. T. Groves, Manganese Porphyrins Catalyze Selective C–H Bond Halogenations. *Journal of the American Chemical Society*, 2010, **132**, 12847-12849.
- 108 J. Fauvarque, The Chlorine Industry. *Pure and Applied Chemistry*, 1996, **68**.
- 109 I. Saikia, A. J. Borah and P. Phukan, Use of Bromine and Bromo-Organic Compounds in Organic Synthesis. *Chemical Reviews*, 2016, **116**, 6837-7042.
- 110 D. Lahaye and J. T. Groves, Modeling the haloperoxidases: Reversible oxygen atom transfer between bromide ion and an oxo-Mn(V) porphyrin. *Journal of Inorganic Biochemistry*, 2007, **101**, 1786-1797.